

**Multifocal Multiphoton Microscopy:
New Detection Methods
and
Biological Applications**

Dissertation

Jörg Martini
Faculty of Physics
Bielefeld University

Bielefeld, November 2006

ERKLÄRUNG

Hiermit erkläre ich, dass ich die vorliegende Arbeit selbstständig verfasst und dabei keine weiteren als die angegebenen Hilfsmittel verwendet habe.

Bielefeld, den 16. November 2006

Jörg Martini

Gutachter:

Prof. Dr. Dario Anselmetti

Prof. Dr. Markus Sauer

Abgabedatum der Arbeit: 17. November 2006

Contents

1	Introduction	1
2	Background	4
2.1	Fluorescence	4
2.2	Absorption of photons	5
2.3	Second harmonic generation	9
2.4	Light intensity distribution near the focus of an objective lens	13
2.4.1	Resolution	16
2.5	Laser scanning microscopy	17
2.5.1	Confocal laser scanning microscopy	17
2.5.2	Multiphoton laser scanning microscopy	19
2.6	Cartilage and cartilage repair	24
2.6.1	Cartilage	24
2.6.2	Cartilage repair	26
2.7	Intracellular protein dynamics using Pa-GFP	27
3	Experimental methods	29
3.1	Samples	29
3.1.1	Pollen	29
3.1.2	Ficus Benjamini	29
3.1.3	Fluorescent beads	29
3.1.4	I/III collagen membranes	30
3.1.5	Cartilage	31
3.1.6	Pa-GFP transfected tobacco BY-2 protoplasts	31
3.2	Fluorescence labeling	32
3.3	The multifocal multiphoton microscope	33
3.3.1	Excitation	33

3.3.2	Parallel non-descanned camera detection	34
3.3.3	Single beam non-descanned PMT detection	35
3.3.4	Parallel descanned detection	36
3.3.5	General considerations regarding spectral detection	38
3.3.6	Non-descanned parallel spectral detection	38
3.3.7	Descanned single beam spectral detection	41
3.3.8	Multifocal multispectral descanned detection	41
3.4	Pa-GFP measurements	43
3.5	The versatile experimental setup	45
3.6	Multi anode PMT electronics	47
3.7	Software	49
3.8	Spectral unmixing	50
4	Results	52
4.1	Cartilage	52
4.1.1	Bovine cartilage	52
4.1.2	Human cartilage	53
4.2	Chondrocytes on I/III-collagen membranes	56
4.2.1	Emission spectra	56
4.2.2	Cell culture conditions without Phenol Red	57
4.2.3	Cell culture conditions with Phenol Red	63
4.3	Parallel descanned detection	71
4.3.1	Scattering suppression	71
4.3.2	Confocal detection	73
4.3.3	Detection efficiency	76
4.3.4	Multifocal multispectral descanned detection	78
4.4	Intracellular protein dynamics using Pa-GFP	80
4.4.1	Pa-GFP diffusion from the nucleus into the cytoplasm	81
4.4.2	Active translocation of the MYB transcription factor LCL1 fused to Pa-GFP	84
4.4.3	Protein dynamics of the export-negative mutant Pa-GFP-LCL(NESm)	86
5	Conclusion and Outlook	88
	Bibliography	94
	List of Publications	106

1 Introduction

Although a microscope opens up a whole new world - directly in front of the user and yet hidden - the simple concept of magnification is extremely convincing: Seeing (through a microscope) is believing. This aspect of human perception, however, better explains why microscopy became a merriment for the upper class in the 17th and 18th century, than why it has become one of the most powerful, versatile and widely used tools in all areas of natural science today. To explain why microscopes are so prevalent in science, or in other words, why a microscopic image constitutes a scientific result, it is necessary to point out that it is the interpretation of a microscopic image that makes it scientific. The recognition of structures and patterns in the samples and hypothesis building, e.g. concluding from the discovery of a cell nucleus that all cells of this type have nuclei, have made microscopy scientific.

The fundamental concept of a microscope¹ is the detection of photons correlated with their spatial and temporal origin. This of course is also the concept of "seeing" in general, but as the human eye has natural limitations regarding sensitivity (photon density), specificity (wavelength, phase, polarization, etc.) and resolution (spatial and temporal), tools (glasses, microscopes, telescopes) are required to overcome these. Early microscopes only extended the spatial resolution of the human eye by magnifying the object under investigation, thereby extending science, from today's perspective, especially biology, into the microcosmos. Magnification is however not the only important property of a microscope, as contrast in the sample, especially in thick (tissue) samples, is extremely important for the identification of its structures.

The need for contrast did not only induce the science of staining² samples, which still is

¹The terms "microscope" and "microscopy", as used in this text, only refer to far field light microscopy techniques, as opposed to near field techniques such as "atomic force microscopy" or "scanning near-field optical microscopy" and microscopy techniques that are based on completely different wavelength regimes such as "scanning electron microscopy". The common basis of all of these highly varied microscopy techniques is the fact that they are all different kinds of magnifying devices. Hence, their names are all based on the Greek words "micro" = "small" and "scope" = "seeing".

²The diversity and specificity of dyes can be considered one of the foundations of scientific microscopical imaging, as it provides the tool for selecting the components of interest in the sample.

one of the most important steps in microscopy, it also triggered the development of new microscopy techniques. This progress has not been limited to the generation of contrast alone, but it has been extended to all features, i. e. sensitivity, specificity and resolution, of microscopes. Although these technical improvements began hundreds of years ago, advances in microscopy do not seem to be slowing down.

These considerations represent the general setting of this work. In this work multifocal multiphoton microscopy (MMM) has, on the one hand, been applied as a technique for the investigation of certain biological samples. On the other hand, new detection techniques have been developed and tested in order to advance the capabilities in MMM. This progress in technical possibilities has been driven by the particular difficulties in imaging the samples of interest, i.e. cartilage, tissue engineering products for cartilage implants and tobacco protoplasts transfected with a *Arabidopsis thaliana* transcription factor. Some of these techniques became a standard measurement protocol for successful imaging of the particular sample of interest, while others were found to be better suited for types of samples that they were not intended for. As this work documents a contribution to the collaboration between partners both in the field of biology, who are interested gaining knowledge on their samples, as well as in the field of microscopy, who are interested in advancing the general techniques, the results serve both groups.

This work has been prepared within the framework of the biophotonics research initiative "Metabolismus und Morphologie von Zellverbänden (MeMo)", the aim of which was advancements in collagen scaffolded growth and stimulation of chondrocytic cells. The optimization of growth conditions was performed by the project partner "Institut für Bioprozess- und Analysenmesstechnik e.V. (IBA)". In order to provide a quality control mechanism for the in vitro cell culture, a 2-photon laser scanning microscope (2PLSM) was coupled to their standard bioreactor based cell culture technique. MMM was chosen as the feedback mechanism for alterations in the cell culture conditions, because it provides the advantages of label-free, contact-free and inherently 3-dimensional resolved imaging with high spatial and temporal resolution. Although these fundamental capabilities of MMM had been expected to sufficiently provide a feedback mechanism for the cell culture conditions, it had not been tested before the project started. The objective of imaging chondrocyte populated I/III-collagen membranes could be loosely summarized as answering the question: What can we see and how do we do that?

The interest in a tissue engineering product used in cartilage repair by transplantation naturally expanded from this product to its origin: the cartilage. With the MMM technique at hand, the following question arose: Which quality characteristics can be inferred from the source of the chondrocytes before the actual tissue engineering process

starts? Thanks to the cooperation with a local orthopedic surgeon, Dr. Michael Dickob, successful examinations of human cartilage were possible.

Another aim of the MeMo project has been the advancement of MMM in general by implementing new and advanced detection techniques. This has been achieved in close cooperation with the project partner and manufacturer of the 2PLSM: "LaVision BioTec". Originally, the collagen membrane samples were not expected to be sufficiently imageable by the 2PLSM's standard imaging mode. Luckily, this assumption did not prove true, but nevertheless an intended solution for the suppression of scattered fluorescence photons has been implemented in a new type of detector. Thereby a new detection mode with improved resolution has been introduced in MMM. Furthermore, various spectral detection modes have been developed and their usefulness, especially for imaging the chondrocyte populated I/III-collagen membranes, could be proven. Most of the techniques have been developed in close cooperation with LaVision BioTec and hopefully some of the new detection modes or ideas for improvements will serve the company as new products.

Finally, the availability of the fast, high resolution MMM-technique in combination with scientific curiosity opened a completely different field of research: intracellular protein dynamics in plant cells. These measurements are the result of an interdisciplinary in-house research cooperation with the "Institute for Genome Research" at Bielefeld University. Their findings, a tessera in systems biology, have encouraged the interest in further dynamical measurements by means of fluorescent label highlighting.

This short overview of the research subjects of this work should make it evident that much of the research was intended to, and in fact did, rely on the expertise and preparation of the biologists and physicians that provided the samples of interest. Furthermore, alterations of the commercial 2PLSM-software were necessary for the implementation of new measurement modes, which had to be performed by the project partner LaVision BioTec. In that sense, this work represents one contribution to a large research network.

2 Background

2.1 Fluorescence

Because the mechanism of fluorescence [1] is central to 2PLSM, this section will provide a brief overview of this fundamental concept¹. The emission of photons by fluorophores (molecules or atoms) due to a relaxing into a lower energy state is called fluorescence. The mechanism of fluorescence is often illustrated by a Jablonski diagram (s. Fig. 2.1). Usually a fluorophore is "lifted" into an excited state when a photon is absorbed which has more energy than the one emitted. The energy difference between the absorbed and emitted photon is called Stokes shift. This energy difference remains as vibrational (and rotational) energy, i.e. thermal energy, in the molecule. Fluorophores do not absorb and emit photons arbitrarily. In order for a fluorophore's electrons to be lifted into unoccupied excited states, the photons must hold specific energy proportions $E = h \cdot \nu = c/\lambda$ (s. Fig. 2.1, a, d). From this state, the fluorophore thermally relaxes into the lowest excited vibrational state (s. Fig. 2.1, b). After remaining in this state for the fluorescence lifetime, usually in the range of $10^{-10} \dots 10^{-8} s$, the fluorophore relaxes into its ground state under emission of a fluorescence photon (s. Fig. 2.1, c). Alternatively, the fluorophore can relax into the ground state without emission of fluorescence light, transfer into a triplet state or transfer energy to neighboring molecules (inter system crossing). Instead of absorbing one exciting photon, it is also possible for two photons of half of the required energy to be absorbed simultaneously via a virtual excitation state (s. Fig. 2.1, d). In this case "simultaneously" means that the absorption of the two photons has to happen within $4 \cdot 10^{-16} s$, the uncertainty time for typical energy differences of $\Delta E = h\nu = \lambda/c = 800[nm]/(3 \cdot 10^8[ms^{-1}]) = 2.67 \cdot 10^{-15}[J]$ according to the energy-time uncertainty principle. Due to the requirement of simultaneous absorption, two photon excitation is a very unlikely process. For the sake of comparison [2], in bright sunlight the photon absorption rate of a Rhodamin 6G molecule (an excellent one- and two-photon absorber) is calculated to be approximately once per second for one-photon absorption

¹"Never underestimate the joy people derive from hearing something they already know." - Enrico Fermi, 1901-1954

and once in 10 million years for two-photon absorption.

Another mechanism of wavelength conversion between incident and emitted light is the process of second harmonic generation (SHG). This process does not require free energy Eigen-states of the fluorophore, it is a scattering (s. section 2.3) and not an absorption/emission process. It is, however, also instructive to illustrate the basic principals of the SHG with the help of a Jablonski diagram (s. Fig 2.1, C) because it represents the energetic relationships well.

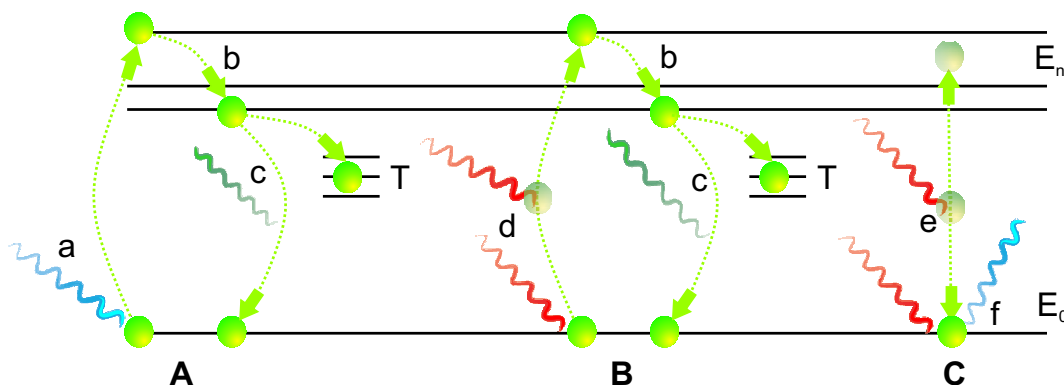


Figure 2.1: Jablonski-like diagram: A) One photon absorption including electron transition (a) of the molecule’s ground state E_0 to an excited state E_n , thermal relaxation (b), transition from the lowest excited singlet either to the ground state under emission of fluorescence light (c) or intersystem crossing, triplet (T); B) Two-photon absorption via a virtual energy state (d) and subsequent relaxation (b), transition to ground state (c) or intersystem crossing, triplet (T); C) Second harmonic generation by energy transfer of two photons (e) with identical wavelengths into one photon (f) with half of the incident wavelengths (s. chapter 2.3)

2.2 Absorption of photons

Time dependent perturbation theory² [4, 5, 6, 7] is helpful for understanding the mechanism of photon absorption by a molecule (atom). The electron’s wave function Ψ obeys the time dependent Schrödinger equation,

$$i\hbar\dot{\Psi} = (H_0 + H_p(t))\Psi \quad (2.1)$$

whereas H_0 and $H_p(t)$ denote the undisturbed Hamiltonian and the time dependent perturbation one respectively and i and \hbar denote the imaginary unit and the Planck

²An alternative calculation by photon density is presented in [3]

constant. For an undisturbed time independent Hamilton function

$$H_0\varphi_n = E_n\varphi_n \quad (2.2)$$

the set of wave functions φ_n and their corresponding (energy) Eigen-values E_n solve Eq. 2.2. Furthermore, the complete set of φ_n may be chosen to be orthonormal:

$$\int \varphi_m^* \varphi_n dV = \delta_{nm} \quad (2.3)$$

To solve the time dependent Schrödinger equation the following approach is commonly used:

$$\Phi_n = \varphi_n \exp(-iE_n t/\hbar) \quad (2.4)$$

Therefore wave functions solving Eq. 2.1 may be written as a linear combination of these time dependent functions, where the $a_n(t)$ represent the time dependent influence of the perturbation on the solution of the wave function:

$$\Psi = \sum_n a_n(t) \Phi_n = \sum_n a_n(t) \varphi_n \exp(-iE_n t/\hbar) \quad (2.5)$$

Substituting Eq. 2.1 with Eq. 2.5 one derives:

$$\sum_n a_n(t) \exp(-iE_n t/\hbar) (H_0 + H_p(t)) \varphi_n = \sum_n \exp(-iE_n t/\hbar) \varphi_n (E_n a_n(t) + i\hbar \dot{a}_n(t)) \quad (2.6)$$

Linearity of the Hamilton operators and Eq. 2.2 simplifies Eq. 2.6 to:

$$\sum_n a_n(t) \exp(-iE_n t/\hbar) H_p(t) \varphi_n = \sum_n i\hbar \exp(-iE_n t/\hbar) \dot{a}_n(t) \varphi_n \quad (2.7)$$

Multiplying from the left with φ_m^* and integrating over space (Eq. 2.3) Eq. 2.7 becomes:

$$\sum_n a_n(t) \exp(-iE_n t/\hbar) \int \varphi_m^* H_p(t) \varphi_n dV = i\hbar \exp(-iE_m t/\hbar) \dot{a}_m(t) \quad (2.8)$$

With the notations

$$\int \varphi_m^* H_p(t) \varphi_n dV = \langle \varphi_m | H_p(t) | \varphi_n \rangle \quad (2.9)$$

and

$$\omega_{mn} = (1/\hbar)(E_m - E_n) \quad (2.10)$$

Eq. 2.8 may be written as:

$$i\hbar \dot{a}_m(t) = \sum_n a_n(t) \exp(i\omega_{mn}t) \langle \varphi_m | H_p(t) | \varphi_n \rangle \quad (2.11)$$

The parameter $a_n(t)$ may be written as a power series in μ , which may be interpreted as the "strength" of the perturbation and therefore ranges between 0 and 1, where $\mu = 1$ describes the physical situation of an existing perturbation, relevant in this case:

$$a_n(t) = a_n^{(0)}(t) + \mu a_n^{(1)} + \mu^2 a_n^{(2)} + \dots = \sum_{k=0}^l \mu^k a_n^{(k)} \quad (2.12)$$

The index k in Eq. 2.12 denotes the order of the perturbation, whereas l is the upper limit for the order of perturbation that has to be taken into account. In principle it has to be assumed that $l \rightarrow \infty$, but in fact many physical problems can be solved using small l . This is due to the fact that the perturbations are commonly assumed to be small, especially if they are of higher order. Therefore, it is possible to evaluate the perturbation terms of Eq. 2.12 iteratively by successively adding higher orders of perturbation. At $t = 0$ the 0th order of Eq. 2.12 describes an Eigen-state φ_{n_0} of Eq. 2.2. Therefore:

$$a_n(t = 0) = a_n^{(0)}(t = 0) = \delta_{nn_0} \quad (2.13)$$

Which implies:

$$\dot{a}_n(t = 0) = \dot{a}_n^{(0)}(t = 0) = 0 \quad (2.14)$$

and

$$a_n^{(1)}(t = 0) = 0 \quad (2.15)$$

As the perturbation is assumed to be small, its first order may be calculated by substituting $a_n^{(0)}(t)$ for $a_n^{(1)}(t)$ on the right side of Eq. 2.11:

$$\dot{a}_m^{(1)}(t) = (-i/\hbar) \exp(i\omega_{mn}t) \langle \varphi_m | H_p(t) | \varphi_n \rangle \delta_{nn_0} = (-i/\hbar) \exp(i\omega_{mn_0}t) \langle \varphi_m | H_p(t) | \varphi_{n_0} \rangle \quad (2.16)$$

For higher orders of perturbation, the following recursion can be derived by the successive "improving" of Eq. 2.11, starting with the result of Eq. 2.16:

$$\dot{a}_m^{(l+1)}(t) = (-i/\hbar) \sum_n \exp(i\omega_{mn}t) \langle \varphi_m | H_p(t) | \varphi_n \rangle a_n^l(t) \quad (2.17)$$

Integration of Eq. 2.17 with respect to the integration limit 2.15 results in:

$$a_m^{(l+1)}(t) = (-i/\hbar) \sum_n \int_0^t a_n^l(t') \exp(i\omega_{mn}t') \langle \varphi_m | H_p(t') | \varphi_n \rangle dt' \quad (2.18)$$

By integrating Eq. 2.16, the first order perturbation, one easily derives:

$$|a_m^{(1)}(t)|^2 = \left| (-i/\hbar) \int_0^t \exp(i\omega_{mn}t') \langle \varphi_m | H_p(t') | \varphi_n \rangle dt' \right|^2 \quad (2.19)$$

With a perturbation operator $H_p(t)$ that describes the interaction between the electric dipole momentum \vec{p} of a fluorophore and the electric field of an incident laser beam, Eq. 2.19 describes the transition probability between the fluorophore's ground state into an excited state, i.e. one-photon absorption of the fluorophore. Assuming that the incident electric field $\vec{E}(t)$ is constant over the expansion of the fluorophore, such a perturbation operator is represented by:

$$H_p(t) = \vec{p} \cdot \vec{E}(t) = -e\vec{r} \cdot E_0\vec{E} \cos(\nu t) \quad (2.20)$$

Here $\nu = c/\lambda$ denotes the frequency of the laser light, while λ is the laser's wavelength and c the speed of light. Furthermore \vec{r} and \vec{E} are normalized base vectors in the direction of the dipole momentum and the electric field respectively. By substituting Eq. 2.19 into Eq. 2.20 and dividing both sides by time, one derives the one-photon absorption probability per time:

$$(1/t) \cdot |a_m^{(1)}(t)|^2 = (1/t\hbar^2) \cdot (-eE_0)^2 \cdot \left| \int_0^t \exp(i\omega_{mn}t') \cos(\nu t') \langle \varphi_m | \vec{r} \cdot \vec{E} | \varphi_n \rangle dt' \right|^2 \quad (2.21)$$

From Eq. 2.21 it becomes evident that the one-photon absorption probability is proportional to the square of the electric field vector or proportional to the intensity $I = c\epsilon_0 E^2$ of the incident laser light.

Now to derive the probability of a two-photon absorption process, we suppose that the fluorophore possesses an intermediate (s. Fig. 2.1) virtual state $k \neq n, m$ with corresponding non-vanishing transition probabilities $\langle \varphi_k | H_p(t) | \varphi_n \rangle \neq 0$ and $\langle \varphi_m | H_p(t) | \varphi_k \rangle \neq 0$. For the first order ($l = 0$) of perturbation, i.e. the transition into the virtual state k , Eq. 2.18 results in:

$$a_k^{(1)}(t) = (-i/\hbar) \cdot (-eE_0) \int_0^t \exp(i\omega_{kn}t'') \cos(\nu t'') \langle \varphi_k | \vec{r}_n \cdot \vec{E} | \varphi_n \rangle dt'' \quad (2.22)$$

Using $l = 1$ in Eq. 2.18 with the result $a_k^{(1)}(t)$ from 2.22 the fluorophore's transition from the initial state n via a virtual one k into the final state m is described by:

$$a_m^{(2)}(t) = (-i/\hbar)^2 \cdot (-eE_0)^2 \sum_k \int_0^t \exp(i\omega_{mk}t') \cos(\nu t') \langle \varphi_m | \vec{r}_k \cdot \vec{E} | \varphi_k \rangle dt' \cdot \int_0^t \exp(i\omega_{kn}t'') \cos(\nu t'') \langle \varphi_k | \vec{r}_n \cdot \vec{E} | \varphi_n \rangle dt'' \quad (2.23)$$

In Eq. 2.23 it is assumed that the electric field, i.e. the laser light, has the same wavelength for both transitions. This is not necessarily always the case³ in two photon

³In principle the two electric field vectors \vec{E} can differ, for example when performing Doppler-free atomic/molecular spectroscopy.

absorption experiments, but in 2PLSM only one laser source is used and wavelength broadening, due to the use of pulsed lasers, is negligible. Furthermore, it should be mentioned that 2-photon excitation does not obey the same selection rules as one-photon absorption. Whereas the selection rule for the angular momentum l in a dipole transition in the one-photon case is given by $\Delta l = \pm 1$, it is $\Delta l = 0, \pm 2$ for the 2-photon case⁴. Although the possibility for 2-photon absorption was predicted in 1931 by Maria Göppert-Mayer in her doctoral thesis, it took until 1961, one year after the invention of the laser, for Kaiser and Garrett to experimentally prove 2-photon absorption [8].

The central result from Eq. 2.23 is that the transition probability $\left| a_m^{(2)}(t) \right|^2$ between two fluorophore's states, due to 2-photon absorption, is proportional to the square of the incident laser intensity.

The excitation rate $P(t)$ for a fluorophore due to 2-photon absorption is given by:

$$P(t) = I^2 \sigma_{2P} \quad (2.24)$$

Here the (laser) intensity I is measured in units of $\left[\frac{\text{photons}}{m^2 s} \right]$, while the 2-photon absorption cross section⁵ σ_{2P} is given in $[m^4 s]$. For 2PLSM a practical formula for the time-average 2-photon fluorescence intensity per molecule I_f is derived in [3, chap. 3]:

$$I_f = \sigma_2 \frac{P_{av}^2}{\tau_P f_P} \left[\pi \frac{NA^2}{hc\lambda} \right]^2 \quad (2.25)$$

(P_{av} : average laser power, τ_P : laser pulse duration, f_P : laser repetition frequency, NA: numerical aperture of the objective lens, c : speed of light, λ : laser wavelength)

Equation 2.25 contains the relevant measurands for 2-photon induced fluorescence in a 2PLSM, because there pulsed laser beams are commonly focused (s. section 2.5.2), in order to achieve sufficient fluorescence yield.

2.3 Second harmonic generation

The second harmonic generation (SHG) effect describes the upconversion of an incident electromagnetic wave, with a frequency ν , into one with a frequency of 2ν . This conversion is due to the second order susceptibility of the material the wave is propagating

⁴This is an interesting aspect of atomic/molecular spectroscopy, because different transitions between energy Eigen-states can be measured by 2-photon than by one-photon spectroscopy.

⁵A common unit in literature is *Göppert-Mayer* (GM), whereas $1 \text{ GM} = 10^{-58} m^4 s$. Due to practical reasons, in many cases the *action* cross section, which is the product of the 2-photon absorption cross section and the fluorescence quantum yield, is listed in literature. The action cross section σ_2 is usually also given in units of GM.

in. SHG may only occur in noncentrosymmetric media because the second order of the susceptibility does not vanish in these. Following the argumentation in [7], the Maxwell equations in media are:

$$\vec{\nabla} \cdot \vec{B} = 0 \quad (2.26)$$

$$\vec{\nabla} \cdot \vec{D} = \rho \quad (2.27)$$

$$\vec{\nabla} \times \vec{E} = -\frac{\partial \vec{B}}{\partial t} \quad (2.28)$$

$$\vec{\nabla} \times \vec{H} = \frac{\partial \vec{D}}{\partial t} + \vec{J} \quad (2.29)$$

(\vec{B} : magnetic induction, \vec{H} : magnetic field, \vec{D} : electric displacement, \vec{E} electric field; ρ charge density; \vec{J} current density)

They simplify under the assumption of charge free ($\rho = 0$), nonmagnetic ($\vec{B} = \mu_0 \vec{H}$) and current free insulating ($\vec{J} = 0$) media to:

$$\vec{\nabla} \cdot \vec{B} = 0 \quad (2.30)$$

$$\vec{\nabla} \cdot \vec{D} = 0 \quad (2.31)$$

$$\vec{\nabla} \times \vec{E} = -\mu_0 \frac{\partial \vec{H}}{\partial t} \quad (2.32)$$

$$\vec{\nabla} \times \vec{H} = \frac{\partial \vec{D}}{\partial t} \quad (2.33)$$

This set of equations differs from Maxwell equations in vacuum only with respect to \vec{D} which contains the influence of the polarization \vec{P} of matter so that \vec{D} may be written as:

$$\vec{D} = \varepsilon_0 \vec{E} + \vec{P} \quad (2.34)$$

By applying the $\vec{\nabla} \times$ operation on Eq. 2.32, changing the order of the operations $\frac{\partial}{\partial t}$ and $\vec{\nabla} \times$ on the right side of Eq. 2.32, it is possible to substitute Eq. 2.33 into the right side of Eq. 2.32, thereby:

$$\vec{\nabla} \times \vec{\nabla} \times \vec{E} = -\mu_0 \frac{\partial^2 \vec{D}}{\partial t^2} \quad (2.35)$$

Furthermore, the identity

$$\vec{\nabla} \times \vec{\nabla} \times \vec{E} = \vec{\nabla}(\vec{\nabla} \cdot \vec{E}) - \vec{\nabla}^2 \vec{E} \quad (2.36)$$

in combination with $\vec{\nabla} \cdot \vec{E} = 0$ has to be noted. After substituting Eq. 2.34 into Eq. 2.35, sorting Eq. 2.35, and using Eq. 2.36, one derives:

$$\vec{\nabla}^2 \vec{E} - \mu_0 \varepsilon_0 \frac{\partial^2 \vec{E}}{\partial t^2} = \mu_0 \frac{\partial^2 \vec{P}}{\partial t^2} \quad (2.37)$$

The polarization \vec{P} of matter may be written as a power series in \vec{E} :

$$\vec{P} = \varepsilon_0(\chi^{(1)} \vec{E}^1 + \chi^{(2)} \vec{E}^2 + \dots) \quad (2.38)$$

Here $\chi^{(n)}$ denotes the n-th order susceptibility of the material. It has to be pointed out that $\chi^{(n)}$ is a $(n + 1)$ th rank tensor, as it contains the orientation of the polarization. Furthermore, only in the case of strong electric fields, i.e. intense laser beams, and in noncentrosymmetric media, does the second order of the susceptibility $\chi^{(2)}$ not vanish.

Substituting Eq. 2.38 into Eq. 2.37 and subtracting the first order of Eq. 2.38 yields:

$$\vec{\nabla}^2 \vec{E} - \mu_0 \varepsilon_0 (1 + \chi^{(1)}) \frac{\partial^2 \vec{E}}{\partial t^2} = \mu_0 \varepsilon_0 \chi^{(2)} \frac{\partial^2 \vec{E}^2}{\partial t^2} + \mu_0 \varepsilon_0 \chi^{(3)} \frac{\partial^2 \vec{E}^3}{\partial t^2} + \dots \quad (2.39)$$

Eq. 2.39 now represents a *driven*⁶ wave function. The right hand side of Eq. 2.39 explains the generation of harmonics of incident $\vec{E}(t)$ -fields.

As an example, SHG can now readily be derived: Given an incident laser beam (in \vec{k} -direction) with an electric field $\vec{E}(\vec{r}, t) = E \cdot \exp(i(\vec{r}\vec{k} - \omega t))$, only first and second order susceptibilities, the relationships for the vacuum speed of light $c = 1/\sqrt{\mu_0 \varepsilon_0}$ and the refractive index of the material $n = \sqrt{1 + \chi^{(1)}}$, Eq. 2.39 becomes:

$$\vec{\nabla}^2 \vec{E}(\vec{r}, t) - \frac{n^2}{c^2} \frac{\partial^2 \vec{E}(\vec{r}, t)}{\partial t^2} = \frac{\chi^{(2)} E^2 \exp(i2\vec{r}\vec{k})}{c^2} \frac{\partial^2 \exp(-i2\omega t)}{\partial t^2} \quad (2.40)$$

On the right hand side of Eq. 2.40 the term $\exp(-i2\omega t)$ expresses the generation of the second harmonic of the incident frequency ω . In summary, it is due to the anharmonic potential of the material which generates harmonics of the incident laser frequency.

In this section, the general procedure of explaining SHG has only been introduced. There are many more interesting aspects to SHG that are too lengthy to include them in this work. Some of these aspects shall, however, be mentioned now with reference to some respective literature.

⁶That is a wave function driven by the influence of the higher orders of the polarization.

- The deduction of SHG in this text did not account for dispersion or damping [7, chap. 3] in the media.
- In highly efficient SHG generating media, such as Lithium Triborate crystals, used for wavelength conversion in lasers, incident laser power depletion, due to SHG, has to be accounted for [9, chap. 2].
- SHG is a special case of sum frequency generation. Therefore, it is important to consider the directions of the incident waves that are being added up. So called "phase matching" is important for efficient SHG. This aspect is particularly important in focused laser beams (e.g. 2PLSM), not only due to cone-like beam paths, but also due to the Gouy phase anomaly [10, 11], [12, chap. 8], [13, chap. 7] in the focal region.
- The intensity of SHG is not only dependent on the phase matching and polarization orientation of the medium, it is also linearly dependent on the square of the incident laser⁷ intensity [16, 17], [13, chap. 7]. Therefore, optical sectioning capacity of 2PLSM also applies to SHG microscopy⁸ [18].
- As SHG stems from laser induced dipoles in the material, the radiation characteristics of these dipoles is anisotropic [19, 10], [13, chap. 7], [7, chap. 2]. 2-photon induced fluorescence has the same character, but in most cases the dipole orientation of fluorophores is isotropic. Therefore, 2-photon induced fluorescence has an isotropic character. This is different for SHG-active materials. They have crystal (or micro crystalline) structures and therefore orientated (and fixed) susceptibilities with corresponding emission characteristics. Therefore, SHG is anisotropic. In 2PLSM for example there is usually an intensity difference in forwards and backwards⁹ scattered SHG signal intensities [10, 20]. This difference can be used to analyze different orientations of samples (e.g. collagen). Furthermore, polarization of the incident laser and corresponding SHG intensities [21, 10] (with respect to their direction and polarization) provide information on the material's susceptibility orientation.

⁷SHG first was experimentally proven in 1969 [14] in quartz crystals, shortly after the invention of lasers. Surprisingly only 2 years later, experiments on rabbit corneas exhibited SHG on biological materials [15].

⁸Hence the term "multiphoton microscopy" (MPM) is often used when referring to non-linear laser scanning microscopes

⁹See section 2.5.2 for epi- and trans-detection in 2PLSM.

- For materials with aligned dipoles, the SHG intensity depends linearly on the square of the dipole concentration¹⁰. This is due to a cooperative increase in SHG scattering susceptibilities [19, 11].
- Because SHG is a scattering process, its lifetime does not exceed approximately 10^{-16} s (s. calculation in section 2.1). Furthermore, SHG *exactly* results in a frequency doubling. This means that no energy is deposited in the material and therefore no phototoxicity or bleaching effects occur in the (biological) material [22] due to SHG.

2.4 Light intensity distribution near the focus of an objective lens

To understand the intrinsic 3-dimensional sectioning capability of a 2PLSM and a SHG microscopy, it is necessary to know the light intensity distribution of a focused laser beam (in z-direction). This intensity distribution, in combination with two-photon absorption probabilities, namely $|a_m^{(2)}(t)|^2 \sim I^2$ (s. section 2.2), explains why 2PLSM optically slices fluorescent specimens. In [12, chap. 8] the scalar (paraxial) approximation for the light intensity near the focus derives for low aperture ($NA < 0.7$ [23, chap. 9]) lenses:

$$I(u, v) = (2/u)^2 I_0 [U_1^2(u, v) + U_2^2(u, v)] \quad (2.41)$$

Whereas I_0 is the intensity in the geometrical focal center and u and v denote the generalized dimensionless spatial positions relative to it:

$$u = \frac{2\pi}{\lambda} \sin^2(\alpha_{max}) z \quad (2.42)$$

$$v = \frac{2\pi}{\lambda} \sin(\alpha_{max}) r = \frac{2\pi}{\lambda} \sin(\alpha_{max}) \sqrt{x^2 + y^2} \quad (2.43)$$

$$NA = \eta \sin(\alpha_{max}) \quad (2.44)$$

With: x, y : lateral distance to geometrical focus; z : axial distance to geometrical focus; λ : wavelength; NA : numerical aperture; η : refractive index

The so called Lommel functions U_n are defined by:

$$U_n(u, v) = \sum_{s=0}^{\infty} (-1)^s \left(\frac{u}{v}\right)^{n+2s} J_{n+2s}(v) \quad (2.45)$$

¹⁰Unlike 2-photon induced fluorescence, which only depends linearly on the fluorophore concentration.

Using the first kind, n-th order Bessel functions $J_n(v)$. Two interesting cases of Eq. 2.41 for $u = 0$ (lateral intensity distribution in focal plane) and $v = 0$ (axial intensity distribution through the focus) are described by:

$$I(0, v) = \left[\frac{2J_1(v)}{v} \right]^2 I_0 \quad (2.46)$$

$$I(u, 0) = \left[\frac{\sin(u/4)}{u/4} \right]^2 I_0 \quad (2.47)$$

A more complex treatment of intensity distribution near the focus suitable for high aperture lenses was derived by Richards and Wolf [24]. As this treatment is a vectorial one, it also accounts for polarization and is the basis for a detailed description [25, 26], [3, chap. 6] of the imaging properties of confocal and 2-photon microscopes. A slight variation in the definition of the generalized coordinate u results in the following intensity distributions for high aperture lenses, as they are presented in [27], [23, chap. 9]:

$$u = \frac{8\pi}{\lambda} \sin^2(\alpha_{max}/2)z \quad (2.48)$$

$$h(u, v) = \exp \left[\frac{-iu}{4 \sin^2(\alpha_{max}/2)} \right] \cdot \int_0^{\alpha_{max}} \sqrt{\cos \Theta} J_0 \left(\frac{v \sin \Theta}{\sin \alpha_{max}} \right) \exp \left(\frac{iu \sin^2(\Theta/2)}{2 \sin^2(\alpha_{max}/2)} \right) \sin \Theta d\Theta \quad (2.49)$$

$$I(u, v) = |h(u, v)|^2 = h(u, v) \cdot h^*(u, v) \quad (2.50)$$

Eq. 2.50 is called the intensity point spread function (IPSF) or short point spread function (PSF) of the (objective) lens. As previously mentioned, 1-photon absorption depends linearly on the incident laser intensity while 2-photon absorption depends linearly on the *square* of the intensity. Therefore the absorption probability for unsaturated fluorescence excitation [28] is $\propto I(u, v)$ and $\propto I(u, v)^2$ for 1-photon and for 2-photons, respectively. For the detection of fluorescence photons on the other hand, Eq. 2.50 describes the "acceptance" distribution for the objective lens. This implies that the detection of fluorescence generated in a 2PLSM or a confocal laser scanning microscope is not only dependent on the excitation PSF, but also on the detection PSF. For a point like detector¹¹ the complete imaging PSF can be derived [23, 32, 33] by $I_{imaging}(u, v) \propto I_{excitation}(u, v) \cdot I_{detection}(u, v)$, where $I_{excitation}(u, v)$ and $I_{detection}(u, v)$ are calculated with the corresponding excitation and emission wavelengths in Eq. 2.49

¹¹A point like detector is usually experimentally realized by a confocal pinhole (s. section 2.5.1). The influence of finite size detectors is described in [29, 30, 31].

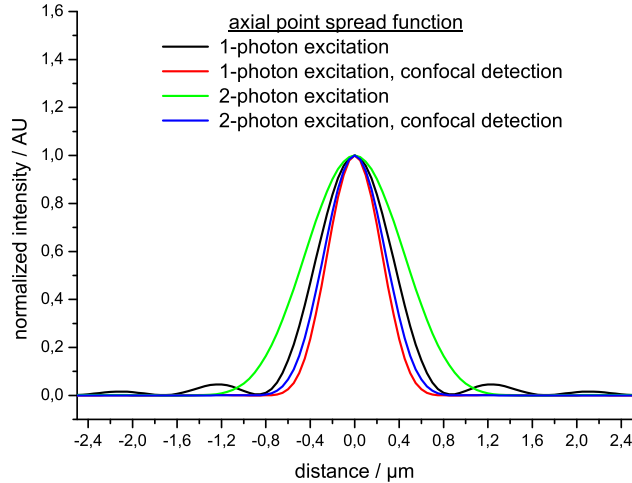


Figure 2.2: Comparison of axial ($v = 0$) PSFs, calculated from Eq. 2.50 for imaging eGFP: 1-photon excitation at 488 nm, 2-photon excitation at 900 nm, eGFP emission maximum at 508 nm, $NA = 1.2$, $\eta = 1.33$, point like detector for confocal detection

and Eq. 2.50. Figure 2.2 shows axial ($v = 0$) and lateral 2.3 ($u = 0$) PSF for several excitation/detection cases. From these figures it can be inferred that 2-photon excitation provides an intrinsic sectioning capacity, as absorption, and thereby excitation of fluorescence, is limited to the small focal volume ($< 1fl$). 1-photon excitation, as the only mechanism of sectioning, on the other hand does not provide intrinsic z-resolution, as there are considerable intensity side lobes (s. Fig. 2.2) along the z-axis. In a point-by-point x-y-scanning scheme, the detector effectively integrates intensity along the z-axis, over the side lobes and considerable contributions of the fluorescence intensity in off-focus regions, and therefore the detected fluorescence signal does not exclusively originate from the focal plane.

Although pixelation and the signal-to-noise ratio of the fluorescence image require a more detailed treatment of PSFs [34] good estimations for the FWHM of the PSF, are provided for non-confocal 2-photon microscopes by the following formulas [28]:

$$FWHM_{lateral} = \frac{0.377\lambda}{NA} \quad \text{for } NA < 0.7 \quad (2.51)$$

$$FWHM_{lateral} = \frac{0.383\lambda}{NA^{0.91}} \quad \text{for } NA > 0.7 \quad (2.52)$$

$$FWHM_{axial} = \frac{0.626\lambda}{\eta - \sqrt{\eta^2 - NA^2}} \quad (2.53)$$

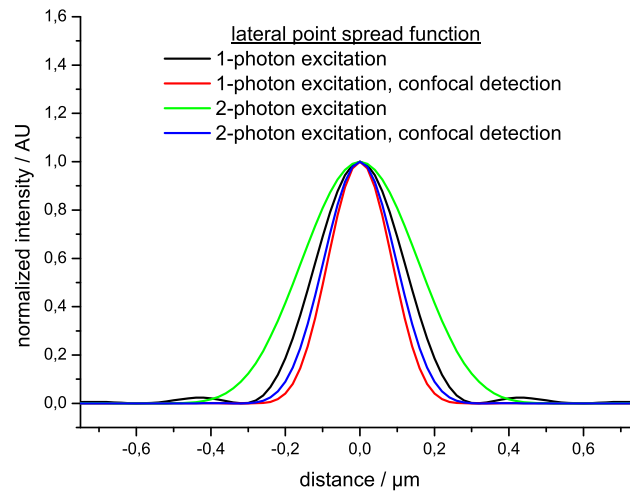


Figure 2.3: Comparison of lateral ($u = 0$) PSFs, calculated from Eq. 2.50 for imaging eGFP: 1-photon excitation at 488 nm, 2-photon excitation at 900 nm, eGFP emission maximum at 508 nm, $NA = 1.2$, $\eta = 1.33$, point like detector for confocal detection

These equations were derived by a Gauß approximation [28] of Eq. 2.50, which is also appropriate when fitting measured PSFs in 2PLSM or CLSM.

2.4.1 Resolution

A common definition for spatial resolution is the distance between two point like, equally bright objects that creates a 26.4% contrast between the middle of their superimposed PSF and their maxima [35]. This particular value of contrast is called Rayleigh criterion and stems from the superposition of two 1-photon PSF where the lateral first PSF minimum (s. Fig 2.3) is positioned at the central maximum of the second PSF. Another common definition is the Sparrow criterion [35] which defines resolution as the distance of vanishing contrast between the two PSFs. Both definitions are based on PSFs, therefore it is obvious, that excitation and emission wavelength especially play a role in resolution¹².

¹²Often spatial resolution of a microscope is among its most interesting specifications. When referring to resolution in microscopy though, one should always keep its basic definition in mind: Resolution is the minimal distance between two point like equally bright objects that allows a sufficient distinction between the objects. Not only is resolution subject to many measurement conditions, but it is also subject to an (almost) arbitrary definition of the term "sufficient". Therefore, the FWHM of the imaging PSF is a more versatile characterization than resolution. However, both of these values

2.5 Laser scanning microscopy

The concept of MPM was first experimentally proven by Winfried Denk et al. [36] in 1990. In his work, a conventional confocal laser scanning microscope (CLSM) was altered by coupling a 630 nm laser into the excitation pathway of the CLSM, choosing appropriate emission filters and by removing the confocal pinhole in the detection pathway (s. fig 2.4). This variation [37] of a "classical" CLSM [38, 39, 40, 41] was the basic concept of a 2PLSM, until non-descanned detection (s. below) was also implemented. It is necessary to include a brief description of CLSMs in this work, as certain characteristics of MPM evolved from it. The main difference between CLSM and MPM is the fact that the sectioning capability of CLSM depends on the use of a confocal pinhole in the detection path, whereas in MPM fluorescence generation is intrinsically limited to the focal volume. Therefore, the requirements of detection concepts in a CLSM are more strict than in MPM. It is important to notice, that epi-detection in LSM results in an intrinsic overlapping of excitation and detection PSF, correct system alignment provided, as the same objective lens is used for excitation and detection. This is usually not true for trans-detection systems, excluding 4π -microscopes, as the axial position of the objective lens is commonly altered, rather than the axial position of the sample, in order to perform depth resolved fluorescence measurements. The details of laser scanning microscopes are addressed in a number of textbooks [3, 23, 39] which provide a much more in-depth treatment of the subject than is possible in this work. Nevertheless, details that explain certain variations in the measurement setup relevant to this work shall be introduced in this section.

2.5.1 Confocal laser scanning microscopy

As can be inferred from Fig. 2.4, the exciting laser beam¹³ is directed via an appropriate dichroic mirror (s. Fig. 2.4; 3) on two perpendicularly orientated scanning mirrors. These scanning mirrors (s. Fig. 2.4; 4) direct the laser beam in different angles (i.e. they scan the laser) on the back aperture of the microscopes (s. Fig. 2.4; 7) objective lens (s. Fig. 2.4; 8). A telecentric combination of a scan- and a tube lens (s. Fig. 2.4; 5) ensures that the scanners movement is only transformed into different incident angles at the center

refer to a certain setup-sample combination, rather than just a measurement device. So in the end, there is not a single specification for the resolution of a microscope.

¹³The laser might have previously been coupled into an optical fiber, which is the case for many presently commercially available CLSM such as Olympus FV1000, Leica TCS SP5 and for mobile laser scanning endoscopes [39, chap. 26].

of the objective lens's back aperture, while at the same time expanding the incident laser beam to the full diameter of the back aperture¹⁴. The focus of the scan lens has to be placed in the middle of the distance vector between the two scanning mirror's rotational axes. This simple scanning geometry works best when the scanning mirrors are in close proximity and the focal length (depth of focus) of the scan lens is rather large. The exciting laser beam then is focused by the objective lens into the sample, inducing fluorescence along the complete optical path in the 1-photon excitation case, yet mainly in the focal volume (s. Fig. 2.2). Due to the scanning mirrors, the exciting focus can be shifted in the focal plane of the objective lens, hence the name "laser scanning microscopy". Fluorescence light from the sample (green path in Fig. 2.4) is

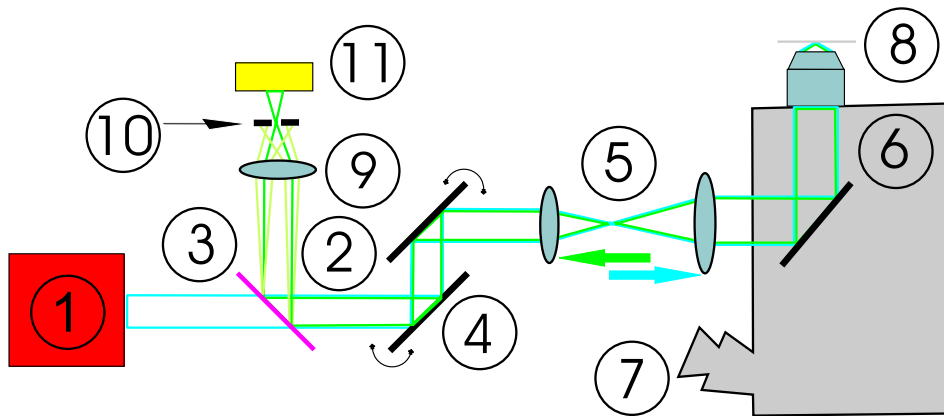


Figure 2.4: Principal setup of CLSM : 1) laser; 2) excitation beam path blue, detection beam path green; 3) dichroic mirror; 4) scanning mirrors; 5) scan/tube lens combination (telecentric); 6) 100% mirror; 7) microscope; 8) objective lens and sample; 9) tube lens; 10) (confocal) pinhole; 11) detector

then collected by the objective lens, and directed back onto the dichroic mirror (s. Fig. 2.4; 3) where exiting laser light and Stokes shifted fluorescence light are separated due to their different wavelength. As the fluorescence light propagates along the same

¹⁴The details of scanning geometries, especially for high resolution CLSM, are rather complex. In order to compensate for off axis reflection points on the second scan mirror due to rotational angles $\phi \neq 0$ of the first mirror, different techniques like additional telecentric lens relay systems, off-rotational axis (second) scanning axis or concave mirror pairs are used [39, chap. 9]. The use of two dimensional single scanning mirrors also provides a sufficient scanning geometry, but it is compromised by slow scanning speed due to increased scanner mass. Acousto-optic modulators are only useful in certain applications [42], as a descanned fluorescence detection in this setup usually results in a spatial broadening of the detection path due to the wavelength dependency of the grating's transmission angle [43].

optical path as the incident laser light, in particular, is also directed onto the scanning mirrors, it is spatially stationary after being reflected by the scanning mirrors. This means that it can be imaged stationary, independent of the scanning mirror position, i.e. the lateral exciting focus position in the sample. This imaging concept therefore is known as "descanned" detection. The stationary fluorescent light is then imaged by the effective tube lens (s. Fig. 2.4; 9) on a pinhole (s. Fig. 2.4; 10) in front of the detector (s. Fig. 2.4; 11). The pinhole is placed in the focus of the tube lens¹⁵ in order to block out-of-focus fluorescence light (s. Fig. 2.4; light green path). The 3-dimensional sectioning capability of a CLSM (s. Fig. 2.2 and 2.3, red curves) is due to the use of the confocal pinhole. The diameter of this pinhole should ideally be as small as possible, but due to signal-to-noise considerations a diameter of one (magnified) Airy disk of the exciting laser light in the sample is a good compromise [31, 33, 44]. When the pinhole is opened beyond this diameter (typically $25 \mu\text{m}$) the imaging PSF approaches the 1-photon excitation PSF (s. Fig. 2.2 and 2.3, black curves) and integrated out-of-focus fluorescence results in a considerable drop of the measurement's resolution. Note, that no complete fluorescence image of the sample is generated in descanned detection. Spatial information about the origin of the fluorescence has to be derived from the scanning mirrors' position and the relative distance between the objective lens and the sample, i.e. the axial position of the focal plane inside the sample. Therefore, 3-dimensional image generation is based on the correlation of the fluorescence intensity, measured by a point detector¹⁶ such as a photo multiplier (PMT) or an avalanche photo diode (APD), and the position of the exciting laser focus. As the 3-dimensional sectioning capacity of a CLSM relies on the use and alignment of the confocal pinhole in the position of the tube lens' focus, it is obvious that scattering of fluorescence light (mainly occurring inside the sample) results in an attenuation of signal intensity in CLSM.

2.5.2 Multiphoton laser scanning microscopy

As many of principles in MPM are the same as in CLSM, this section will only refer to the significant differences between these two types of microscopes. In section 2.2 it is made evident that excitation laser wavelengths in 2PLSM have to be approximately twice the fluorophore's 1-photon absorption wavelength, offering for example the possibility to excite ultra violet (UV) absorbing fluorophores in the visible (VIS) spectral

¹⁵Such a pinhole is usually called "confocal".

¹⁶In this case the term "point detector" does not mean that the active detector area is in the range of one Airy disk, but, that the detector only has one pixel.

range [45, 46, 47, 48]. As the typical Stokes shift for VIS fluorophores is in the range of 10 nm to 100 nm, near infrared (NIR) excitation laser light is commonly used in 2PLSM [49, 50, 51, 52, 53]. Furthermore, pulsed laser light significantly increases the fluorescent yield of 2-photon excited fluorophores (s. Eq. 2.25). Therefore, mode locked Titanium-sapphire (Ti:Sa) lasers are a very prominent laser source in 2PLSM. Many of them are wavelength tunable in a range of 700 to 1000 nm and offer pulse duration of approximately 100 fs and repetition rates of approximately 100 MHz¹⁷. While, on the one hand, the choice of NIR excitation light is of course reasoned by the cross sections of interesting fluorophores [41], it, on the other hand, offers the advantage of reduced scattering and 1-photon absorption, which results in reduced out-of-focus phototoxicity and fluorescent background in biological tissue [54, 55, 56, 57].

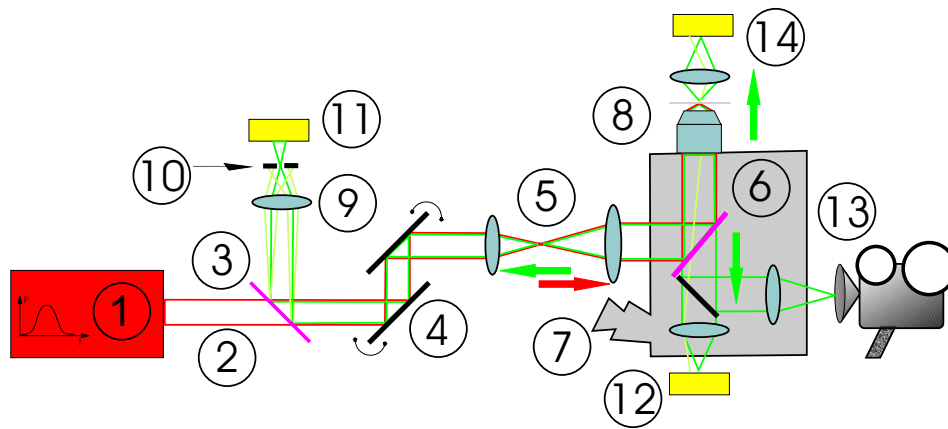


Figure 2.5: Principal setup of 2PLSM : 1) pulsed NIR laser; 2) excitation beam path red, detection beam path green; 3) dichroic mirror; 4) scanning mirrors; 5) scan/tube lens combination (telecentric); 6) 100% or dichroic mirror; 7) microscope; 8) objective lens and sample; 9) tube lens; 10) (confocal) pinhole; 11) detector; 12) epi non-descanned detector 13) camera; 14) trans non-descanned detector

The optical excitation path in MPM is in principle the same as in CLSM. Differences mainly occur due to different excitation/emission wavelength combinations, resulting in other filter/dichroic mirror combinations than in CLSM. Special care with respect to

¹⁷For 2PLSM purposes, these specifications are almost ideal. Pulse durations of 100 fs allow for sufficient fluorescent yield, yet they limit the effects of unwanted higher (>2) order excitation processes or photo ionisation. Repetition rates of 100 MHz translate into a time window of 10 ns between two laser pulses. In combination with typical fluorescence lifetimes in the same order, this prevents excitation saturation or photo ionisation due to more than one laser pulse. The wavelength range of Ti:Sa lasers is appropriate for many VIS or UV excitable dyes.

pulse broadening due to wavelength dependent dispersion has to be taken in MPM when introducing optical fibers or complex optical setups (s. section 2.5.2) in the excitation path.

Fluorescence generation in MPM is intrinsically limited to the focal volume of the objective lens. Therefore, the main differences between MPM and CLSM lie in the fluorescence detection path.

- The same descanned detection path as in CLSM¹⁸ can be used in MPM. The confocal pinhole (s. Fig. 2.5; 10) is, however, not necessary. If it remains in the detection path, it improves the measurement's resolution (s. Fig. 2.2 and 2.3, blue curves) at the cost of a loss in detection signal.
- Trans non-descanned detection (s. Fig. 2.5; 14) is commonly used when measuring SHG signals. For these measurements, it is crucial to block out exciting laser light by the use of appropriate filters and a sample which transmits sufficient intensities of fluorescence light for detection (i.e. a "thin" sample). As the excitation of fluorophores/SHG provides 3-dimensional sectioning, it is not necessary to define precise detection paths, as in the descanned detection mode, but rather to collect all excited fluorescence/SHG light by a high numerical aperture detection lens in front of the detector. Such a lens is particularly important for detecting fluorescence/SHG signal that is scattered within the sample. As non-descanned detection does not generate (time dependent, i.e. scanner position independent) stationary signal paths, it is necessary to have large area one pixel detectors, such as PMTs. The recipe for non-descanned single beam detection, especially for strongly scattering samples, is therefore simply collecting as much signal as possible.
- Epi non-descanned detection (s. Fig. 2.5; 12, 13) uses the laser focusing objective lens as the fluorescence detection lens like in the descanned detection mode. The central difference to this mode is the introduction of a dichroic mirror (s. Fig. 2.5; 6) in front of the objective lens. This mirror reflects the exciting NIR into the sample and transmits the generated VIS fluorescence from the sample¹⁹. Trough

¹⁸2PLSM was patented [58] in 1991. Therefore, only one company (until 2004: Bio-Rad Laboratories, Inc.; since 2004: Carl Zeiss Jena GmbH) may market laser scanning microscopes as MPM. But almost all major CLSM producing companies offer additional optical ports for coupling NIR lasers into their microscopes, i.e. they offer customers the option for setting up their own 2PLSM. If the detection path of these systems is not altered by the customer as well, such a system uses a descanned detection scheme.

¹⁹Additional NIR filtering in the detection path is mandatory.

the microscope's tube lens this fluorescence light is then imaged onto either a single-pixel detector (s. Fig. 2.5; 12) or a camera (s. Fig. 2.5; 12). With these two detectors different image generation schemes are realized. The single pixel detector (i.e. PMT) is used in the same manner as in trans non-descanned detection: Fluorescence images are generated by correlating the scanning mirrors' position with the fluorescence intensity. Camera detection does not require this correlation as it is intrinsically position sensitive. The exciting laser beam is scanned in the region of interest (ROI) inside the sample while the camera chip is exposed by the fluorescence light generating the image.

Non-descanned point detection

When using single-pixel detectors in non-descanned detection, image generation is also performed by the correlation of fluorescence intensity and scanning mirror position. Here it does not matter whether fluorescence photons reach the active detector area scattered or ballistically, as they are attributed to the 2-photon excitation focus. Therefore, this detection concept provides the highest imaging depths in MPM, but excludes the use of multiple simultaneous excitation foci because fluorescence can no longer be attributed to a well-defined origin.

Simultaneous epi- and trans-detection do not exclude each other and provide, especially for SHG imaging, additional information on the sample [10, 20, 59]. Furthermore, it increases the detected fluorescence intensity, because of the doubled solid angle of detection. A key consideration in the implementation of a (usually additional) trans-detection system is the transparency of the sample. As 2PLSM has especially advantages over CLSM when imaging deep within scattering media [56, 60, 61, 62], potentially in vivo [63, 64, 65, 66, 67], trans-detection is often not feasible due to thick samples. Epi-detection, however, provides imaging depth of up to 1 mm [68] in optically dense samples and has the advantage over CLSM [60] that there is no significant broadening of the imaging PSF deep within samples [69], as only ballistic NIR photons contribute to 2-photon excitation [70]. The ultimate limits for deep MPM tissue imaging are the scattering of exciting laser light, scattering of fluorescence light and, in cases of extremely high excitation intensities, out-of-focus fluorescence background [56, 62, 71, 68]. For both epi- and trans-detection in the non-descanned measurement mode, it is beneficial to place an additional large diameter focusing lens in close proximity to the collection (or tube) lens, in order to still image strongly scattered fluorescence photons onto the

detector²⁰. Imaging quality of such a setup does not play a role, as the unaltered excitation PSF defines the imaging quality of the measurement. The detection optic simply needs to collect as many fluorescence photons as possible.

Non-descanned camera detection

Detecting 2-photon excited fluorescence in a non-descanned manner provides the advantage of video rate, full frame image acquisition [73], especially when using high quantum efficiency (up to 90%) EMCCD cameras. Comparable imaging speeds are achievable with PMT-detection microscopes [74, 75] but they do not allow for multifocal multiphoton excitation or simultaneous 1-photon brightfield fluorescence excitation. Aside from the relatively uncomplicated handling and adjustment of non-descanned CCD-detectors, they offer the advantage of simultaneous spatial (x-direction on the CCD-chip) and spectral detection (y-direction on the CCD-chip) under proper experimental conditions (s. section 3.3.6). In the case of fluorescence images of deep sample planes, the ratio of scattered-to-ballistic fluorescence photons dramatically increases as can be inferred from the following formula, derived from the Lambert-Beer-like exponential decay of fluorescence power [56]:

$$\frac{N_S}{N_B} = \frac{1 - \exp(-z/l(\lambda))}{\exp(-z/l(\lambda))} \quad (2.54)$$

(N_S : number of scattered photons; N_B : number of ballistic photons; $l(\lambda)$: mean free path, wavelength and material dependent; z : depth of optical plane in sample) For non-descanned camera detection such an increase results in image haze, loss of contrast and ultimately in a loss of sectioning capacity in deep optical planes. This is due to the fact that scattered photons contribute to image generation on the wrong CCD-pixel, i.e. the information about the fluorescence light's origin is not maintained because of scattering.

Multifocal multiphoton microscopy

Due to small 2-photon action cross-section of fluorophores [76, 77], fluorescence photon statistics are a concern in MPM. Although pixel dwell times in the range of 100 ns can be achieved for full frame images with high speed laser scanning microscopes, the deciding factor for pixel dwell times of a measurement is sufficient fluorescent intensity in the sample and is therefore determined by the fluorophores under investigation. An

²⁰This is the practical solution to extend the effective aperture of the detector, which is necessary as the out-of-focus surface of the sample can be considered as the origin of the scattered fluorescence [72]

increase in laser intensity obviously leads to higher fluorescence generation but it also leads to an even steeper increase in phototoxicity [55, 78, 57], [39, chap. 38] in biological samples, limiting the average femtosecond focused pulsed laser power to some mW per focus. While a typical modern Ti:Sa laser roughly generates an average of 1.5 W, MPM just uses only a few per mill of this power. The idea of multifocal multiphoton microscopy (MMM) is to provide fluorescence generation with the additional 99% available laser power. By splitting the incident laser beam into a number (N) of beamlets and imaging the sample with N fluorescent foci simultaneously, each one of them delivering an intensity under the biologically justifiable threshold, results in an (ideally) N -fold increase of signal intensity. There have been two major approaches in splitting up the incident laser. The first approach has been the use of microlens or Nipow disk arrays to divide the expanded laser beam into a set of up to 100 beamlets [39, chap. 29], [79, 80, 81, 82, 83, 84]. Special care has to be taken in those setups to prevent unwanted optical (out-of-focus) excitation crosstalk between the beamlets [85]. Furthermore, due to the expansion of the laser beam, the beamlet's average intensity is not necessarily identical. The second approach has been the implementation of 100% and 50% mirror combinations to split up the incident laser beam [86, 87, 88, 89](s. section 3.3.1). With this setup the average beamlet intensity is identical and due to different optical path lengths neighbouring foci are temporally decorrelated. Additionally it has been shown that such a setup is capable of imaging without scanning [90], keeping the intrinsic 3-dimensional sectioning capability of high numerical aperture objective lenses. Both approaches use non-descanned video-rate camera detection for multifocal image generation. Therefore, MMM is well suitable of imaging fast biological dynamics [80, 64, 91].

2.6 Cartilage and cartilage repair

2.6.1 Cartilage

Cartilage is a highly specialized connective tissue which is found in various forms in mammals and fish, i.e. elastic cartilage (e.g. in the ear), fibrocartilage (e.g. connecting ligaments and tendons to the bone) and hyaline cartilage (e.g. covering the bone in joints). Chondrocytes are the only type of cells found in cartilage. For this work, the strongly light scattering, yet not absorbing, opaque²¹ articular cartilage is the most interesting type. Hyaline cartilage serves as a rather hard gel coating on bones in joints, e.g. the knee, as a lubricant between the two touching bones. It does not only

²¹Hence it is called "hyaline".

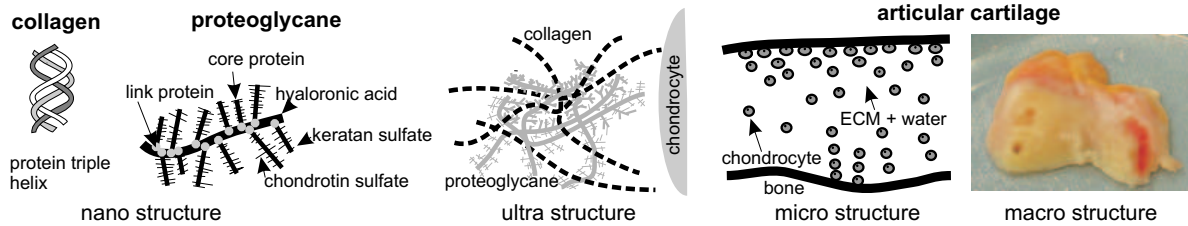


Figure 2.6: Composition and structure of ECM and cartilage.

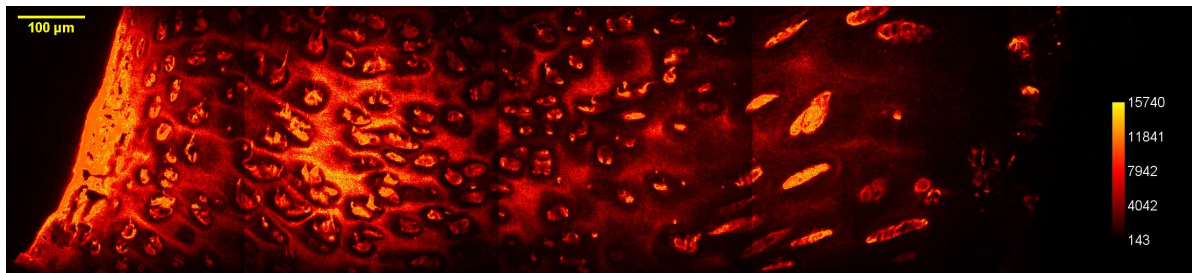


Figure 2.7: Full thickness MPM composite image of non-arthrotic bovine hyaline cartilage: Collagen VI stained with FITC according to [92]; outer cartilage surface on the left, chondrocytes located in lacunae with reduced fluorescence intensity, chondrocytes close to the bone on the right are oriented in rows

provide low friction between the two bones, it furthermore prevents bone injuries due to high impact stress, e.g. walking, running, jumping etc.. Chondrocytes both compose and maintain the cartilage. They are embedded in their extracellular matrix (ECM) and are located in cavities (lacunae) with reduced ECM density, which along with retained water (60%-80%), constitutes the functional cartilage material [93, 94, 95]. The ECM mainly consists of collagen II (10%-20%), proteoglycans (5%-7%) like chondroitin sulfate and keratan sulfate and minor parts of collagens type V, VI, XI, X, XI. The main task of the proteoglycans is the chemical and mechanical linkage between the collagens and the water. The latter two components are primarily responsible for the mechanical properties of the cartilage [96], such as stiffness and a low dynamic friction coefficient. Collagen II is found in fibrillic form in cartilage, ensuring the structural integrity of the material, while the proteoglycans repel each other due to their electronegativity and therefore create an internal pressure in the material. Cell distribution and density varies considerably within individual cartilage structures and the latter also between different individuals [97]. An overview of different cartilage components can be inferred from figure 2.6, while figure 2.7 shows the microstructure of bovine hyalin cartilage. There are no blood vessels in

cartilage, therefore the support of chondrocytes with nutrients is driven by diffusion. Not only do chondrocytes not proliferate, but, because of the dense structure of the ECM, they maintain their position inside the cartilage for decades and they do not proliferate. Therefore, cartilage has limited healing and regeneration capabilities. The degeneration of cartilage (arthritis), i.e. loss of ECM and water and therefore loss of biofunctionality, is a widespread health problem in our aging society [98, chap. 7]. Moreover, cartilage has very limited healing capacity after suffering from lesions and due to mechanical stress, a lesion most likely will accelerate the degeneration of the cartilage. Presently, there is no sufficient medical treatment for aging related degeneration of cartilage, however, there are a number of successful treatments for cartilage injuries.

2.6.2 Cartilage repair

Cartilage repair is performed with a multitude of techniques [99, 100] including microfractures, autologous chondrocyte implantation, and various transplants. Stem cell based repair is currently under investigation. The method of matrix induced autologous chondrocyte implantation (MACI) [101, 102, 103] has been of special interest in this work.

In a MACI procedure a cartilage biopsy extracted from the individual's articular cartilage during an endoscopic operation. The chondrocytes are isolated from the ECM, proliferated in vitro and sown on a porcine I/III-collagen bilayer membrane that provides a scaffolding structure for the chondrocytes adhered to the membrane. The collagen membranes are kept four to six days under cell culture conditions before it is reimplanted onto the donors cartilage defect in the actual surgical operation. The cartilage healing process starts after this implantation: Enough chondrocytes²² start to rebuild new ECM in their in vivo environment, because the collagen scaffold provides them with a 3-dimensional localization which enables the cells to again form a compact meshwork. Within approximately one to two years the collagen membrane is catabolized and new functional cartilage(-like) material covers the lesion. Aside from providing mechanical scaffolding for the chondrocytes, the collagen membrane serves two more purposes in this treatment. First, it provides mechanical protection for the chondrocytes and the newly built ECM during physiological use of the joint. Second, it supports the redifferentiation of chondrocytes so that they have improved potential to rebuild cartilage [98, chap. 7]. The optimization of this potential, which can be summarized as the goal to

²²In an unsupported natural healing process, only chondrocytes next to the lesion could contribute to ECM generation due to its dense structure.

cultivate as many redifferentiated chondrocytes on the collagen membranes as possible, is a key interest for the project partner IBA in the MeMo-project. In particular it seems to be a promising strategy to apply "knee-like" mechanical stress to the chondrocyte populated membranes *in vitro*²³, in order to support chondrocyte redifferentiation [104], [98, chap. 7]. The demand for an online quality control of tissue engineering products, such as chondrocyte populated membranes, motivates the linkage between bioreactors and 2PLSM as an excellent method to measure native macrocellular structures.

2.7 Intracellular protein dynamics using Pa-GFP

Selective measurement techniques with high spatial and temporal resolution are required in order to reveal protein dynamics in living cells. Monitoring protein movements in living cells is of key interest for the quantitative understanding of dynamics in regulatory networks that involve protein interaction. However, conventional one- and two-photon laser scanning microscopy of equilibrium states only reveals a stationary picture of protein distributions in the cell. The investigation and quantitative real-time analysis of intracellular protein dynamics therefore requires the combination of a fast microscopy technique with high spatial and temporal resolution and the ability for locally confined and selective labeling of fluorophores. These labeling techniques include "fluorescence recovery after photobleaching" (FRAP) [105, 39], photochemical changes of emission spectra of fluorophores [106, 107] and photochemical changes in absorption spectra of fluorophores. A prominent example for the latter is Pa-GFP [108, 109, 110, 111, 112]. Upon spectral activation at 408 nm, a photoconversional shift in the absorption maximum from 408 nm to 504 nm, with a maximum of fluorescence emission at 517 nm, is induced. For 1-photon excitation at 488 nm, an increase in fluorescence intensity after 408 nm-photoactivation by a factor of 100 has been reported [110].

In the 2-photon activation case, NIR radiation between 720 nm and 840 nm (peak efficiency at 750 nm [111]) enables an activation of Pa-GFP. This means that the absorption maximum is shifted from ≈ 810 nm for unactivated Pa-GFP to ≈ 920 nm for activated Pa-GFP. Thus, the 2-photon activation procedure at 800 nm induces an increase of Pa-GFP fluorescence intensity of a factor up to 5 (s. section 4.4.1, [113]) upon 920 nm 2-photon excitation. Although this type of protein highlighting is significantly less effective than 1-photon activation, it does provide the 2-photon immanent advantage of confining the activation volume to the focal volume of the objective lens [111]. Whereas

²³For an extensive control of many *in vitro* conditions, such as temperature, gas concentration, composition of cell culture medium and also mechanical stress, so called bioreactors are used.

in the 1-photon activation case Pa-GFP is activated along the complete optical path in the sample, the activation volume in the by two photons is confined to < 1 fl (s. section 2.4).

In eukaryotic cells the cell nucleus and the cytoplasm are separated from another by the nuclear envelope [114, chap. 2], [115, 116]. As proteins, also nuclear ones, are synthesized in the cytoplasm, it is obvious that nucleus and cytoplasm can not be entirely separated from another. While for example nuclear proteins need to enter the nucleus, the RNA encoding these proteins has to leave its nuclear origin to be translated in the cytoplasm. This crucial nucleo-cytoplasmatic trafficking of macromolecules through the nuclear envelope is enabled by the nuclear pore complexes (NPC). Small (up to 60 kDa [116]) macromolecules may pass the NPCs by diffusion, but larger molecules need to be actively transported. Furthermore, active transport does not only allow for the translocation of large macromolecules, but it also enables a controlled accumulation, for example it may act against concentration gradients of individual molecules, and accelerated trafficking. The facilitated translocation of cargo molecules through the NPCs is imparted by receptors such as Importin β and Exportin1 (XPO1) in *Arabidopsis thaliana*. For a cargo molecule to be actively imported or exported it needs to contain a nuclear localization signal (NLS) or a nuclear export signal (NES), respectively. These signals are recognized by their corresponding transport receptors, in the case of XPO1 directly and in the case of Importin β mediated by Importin α . The receptor-cargo complex is then transported through the NPC via an interaction between the transport receptor and the NPC. After passing the nuclear envelope, receptor and cargo dissociate, enabling the receptor to carry out its next transport cycle after passing the NPC once more.

The *Arabidopsis thaliana* MYB1R transcription factor LHY/CCA1-like1 (LCL1) contains a NLS as well as a NES sequence, so that it is subject to both, active import into and active export out of the nucleus [116, 117]. The active export of LCL1 mediated by XPO1 has been quantitatively measured by labeling these protein with Pa-GFP and activating Pa-GFP in the nucleus. Consequently, the distribution of activated Pa-GFP, i.e. the receptor facilitated translocation of LCL1, could be imaged in real-time by fluorescence microscopy. The accelerated dynamics of the active transport has been compared to the diffusional Pa-GFP distribution into the cytoplasm of the transfected tobacco BY-2 protoplast. Furthermore, control experiments performed on cells expressing an LCL1 mutant carrying an eleven amino acid point mutation in the NES region, revealed an accumulation of LCL1 in the nucleus, due to its NLS.

3 Experimental methods

3.1 Samples

Sample preparation has not been a significant part of this work, as a central goal has been to specify and alter measurement conditions so that they are sufficient for imaging untreated (unstained) samples. To derive these samples in the first place requires highly specialized expertises of biologists and physicians which therefore contributed to a great extend to this work. All biologically relevant samples in this work have been treated as carefully as possible, which means they were permanently kept under their physiological condition as far the measurement allowed for. In particular all samples have been imaged while they were submerged in cell culture medium or physiological buffer.

3.1.1 Pollen

Fluorescent labeled and fixed mixed pollen (30-4264) were purchased from Carolina Biological Supply Company.

3.1.2 Ficus Benjamini

Wild type Ficus Benjamini leafs were obtained from the plant resource center of the Department for Experimental Biophysics and Applied Nanoscience at Bielefeld University. The leafs were carefully removed from the complete plant, cut into approximately 10 mm x 10 mm pieces and mounted with water between a microscope slide and a cover slip. Samples then were imaged within 2 hours.

3.1.3 Fluorescent beads

The fluorescent beads set PS-Speck for measuring PSF was purchased from Invitrogen. It contains beads of 0.175 μm diameter with different excitation/emission wavelengths as can be inferred from Tab. 3.1. The beads have been immobilized on a cover slip by spreading 5 μl of fluorescent bead stock solution and 10 μl of H_2O on a cover slip. After

evaporation of the solution 15 μl H_2O were again spread on the cover slip and it was covered with a microscope slide. This "package" was finally sealed with nail polish (Long Lasting Nail Colour, Rival de Loop). The procedure ensured a sufficient coverage of the cover slip's surface with adhered beads.

Type	Excitation wavelength	Emission wavelength
Blue fluorescence	360 nm	440nm
Green fluorescence	505 nm	515 nm
Orange fluorescence	540 nm	650 nm
Red fluorescence	633 nm	660 nm

Table 3.1: Overview of 1-photon excitation and emission wavelengths of PS-Speck fluorescent beads.

3.1.4 I/III collagen membranes

Porcine I/III collagen membranes are produced by Matricell. Two fundamentally different types of membranes have been used in this work (s. Fig. 3.1). The first kind, a so called fleece membrane, is an extracted and sterilized natural product, as it is currently used in MACI cartilage repair procedures. The bottom layer of this material (approximately 2 mm) consists of tightly, parallel oriented, thin (diameter $> 10 \mu\text{m}$) collagen fibers, which provide the mechanical integrity of the membrane and therefore also the protective layer for the graft. The top layer (approximately 200 μm) of a fleece membrane is formed by loosely "woven" thick (diameter up to 80 μm) collagen fibers, which allow for the chondrocytes to adhere to them and therefore provide their scaffolding. The second kind, the so called sponge-like collagen membrane, is a processed type of I/III collagen. The basic collagen material is dissolved and pressed through a chilled solution which forms microscopic icicles. The collagen fibers condense around and along the icicles and therefore form a honey comb tube structure. The details of this procedure are, however, not publicly known. Chondrocytes that had been previously isolated and proliferated, have been sown onto the collagen membrane which then has been kept under cell culture conditions¹ for 3 days. For MPM examinations the membranes have been shipped directly to the Bielefeld laboratory, so that they could be imaged or re-inserted into cell culture conditions within 3 hours. This time frame is in keeping with the transplantation protocol for human MACI treatments.

¹The membranes are submerged in cell culture medium and stored at 37°C with 5% CO_2 gas concentration.

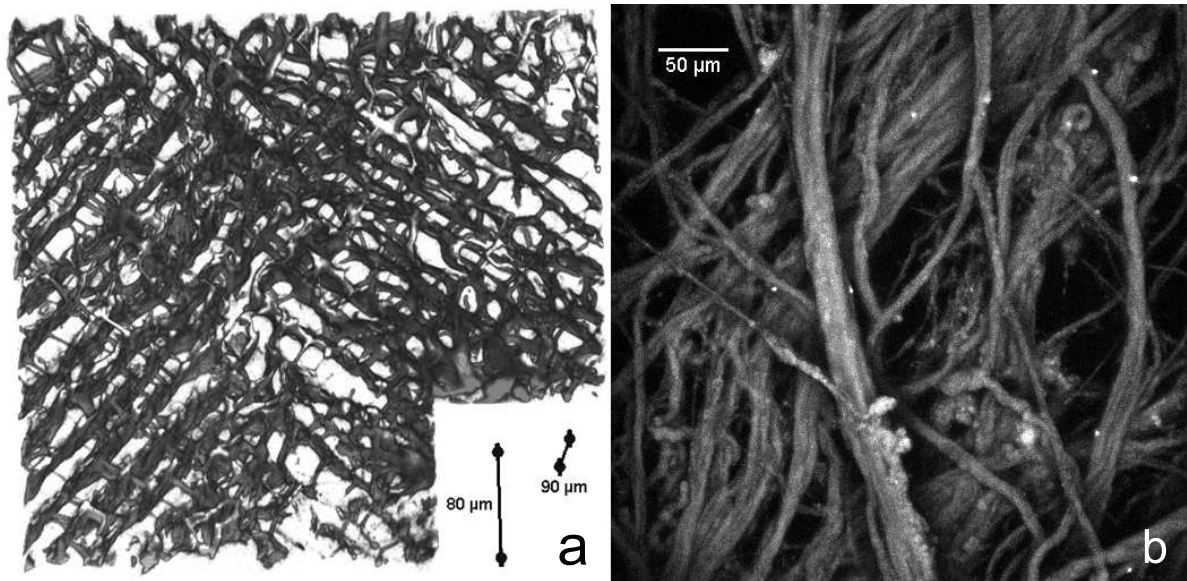


Figure 3.1: 2-photon induced autofluorescence of collagen membranes: a) sponge like collagen membrane, voxel representation, scale bars in x and z direction; b) fleece collagen membrane, maximum intensity projection of image stack covering 160 μm depth

The details of isolation, proliferation and chondrocyte seeding protocols for MACI treatments are not publicly known. A description of the respective bovine protocols can be found in [92, 95].

3.1.5 Cartilage

The bovine cartilage was directly acquired from the slaughterhouse [92]. Chondrocytes for cultivation were obtained from a fresh sample, while complete cartilage for imaging purposes was frozen after the extraction.

Human cartilage for imaging purposes was obtained from the local hospital, kept in buffer solution and imaged within 6 hours after extraction.

3.1.6 Pa-GFP transfected tobacco BY-2 protoplasts

Tobacco BY-2 protoplasts have been transfected with Pa-GFP and Pa-GFP fused to LCL1 and LCL1(NESm) at the "Institute for Genome Research" at Bielefeld University. Details on the protein LCL1 and especially its eleven amino acid point mutation LCL1(NESm) can be found in [116]. The Pa-GFP transfection protocol is described in [113]. Furthermore the protoplasts have been co-transfected with the red-fluorescent

protein (DsRed)-tagged prenylated Rab acceptor 1 (Pra1; At2g38360), a membrane-localized protein that clusters around the nuclear envelope. It is necessary for identification and visualization of successfully transfected protoplasts.

3.2 Fluorescence labeling

To evaluate the physiological state of chondrocytes on collagen membranes, staining protocols were applied after measuring the native fluorescence of the samples. As the goal of these measurements was to compare both results in order to specify sufficiency of the native fluorescence measurements, special care had to be taken to image identical sample regions. Therefore, the sample could not be moved from its original position during the native fluorescence measurement, in particular, when applying the stain. Washing of the sample and the determination of label concentrations in the sample was therefore not possible. The latter is due to the fact that the collagen membrane samples retain considerable amounts of cell culture medium in which they have to be submerged during the measurement. The amount of cell culture medium was chosen so that the collagen membrane was covered by a drop of cell culture medium. The measurement container was not filled to prevent the sample from floating. This means that the total amount of cell culture medium present in the complete sample remained unknown. The pragmatic solution to staining chondrocytes on collagen membranes was to apply 10 to 50 μl of fluorescent label on top of the collagen membrane and to wait until the cells were clearly stained. SYTO 9 (Molecular Probes, 3.34 mM, emission maximum at 500 nm) was first applied to the sample and it usually took 30 minutes until all cells were labeled. After successful staining, a complete 3-dimensional scan of the ROI was performed with respect to the emission wavelength. After this scan, Propidium Iodide (Molecular Probes, 20 mM, emission maximum at 635 nm) was applied to the sample, staining the DNA in dead cells or DNA fragments, usually after 10 minutes. Again a complete 3-dimensional scan was performed with respect to the two different emission wavelengths of the fluorescent labels. As a result, the second image stack contained all of the required information. Living cells were stained with SYTO 9 and dead cells were stained with SYTO 9 and Propidium Iodide.

3.3 The multifocal multiphoton microscope

In this section, the focus of interest for this work, the multifocal multiphoton microscope, is described. With the exception of Pa-GFP measurements for intracellular protein dynamics, the outline of this section is based on the different detection techniques rather than the relevance of these techniques regarding different samples. Pa-GFP measurements require their own experimental description, which, however, does not differ too much from non-descanned camera detection. The initial commercial experimental setup consisted of a MMM, which only allowed for non-descanned camera detection. Additional measurement modes are an integral part of the work, described in this text. Section 3.5 will summarize the described measurement modes by pointing out the most versatile setup of the MMM. As some of the measurement modes do exclude each other, there is a MPM setup that is most likely suitable for a new unknown sample.

3.3.1 Excitation

The optical excitation path remains the same in all MPM measurements. Therefore the following description applies to the components 1 to 13 in the figures 3.2, 3.3 and 3.4. Relevant alterations of the experimental setup for Pa-GFP measurements will be presented in the corresponding subsection. The NIR laser light is generated by a mode-locked femtosecond Ti:Sa laser (1) pumped by a solid-state laser (Tsunami & Millennia X, both Spectra Physics) and coupled into the multi beam scanning unit (TriM-Scope, LaVision BioTec). In this unit, the beam is directed through a step motor driven polarizer and fixed analyzer for beam intensity attenuation and through a beam expander (2) into the pre-chirp section (3). This section temporally "compresses" the laser pulses by guiding the red shifted parts of the wavelength spectrum on a longer optical path than the blue shifted ones. This compensates for later pulse dispersion in the following optics, particularly in the beam multiplexing section (4). It consists of a central 50% mirror (5) and a set of ten 100% mirrors which multiplex the incident laser beam into up to 64 beamlets, each one of them carrying the same average intensity. The number of exciting beams is selectable (1, 2, 4, 8, 16, 32, 64) by adjusting the number of passages through the 50% mirror of the incident laser, defined by the position of the mirror. The beamlets are directed through a shutter section (6) onto a dichroic mirror (7). In descanned detection exciting laser light and fluorescence light are separated by this dichroic mirror (680dcspxr, Chroma Technology Corp.). The exciting beamlets are

directed by the dichroic mirror onto the silver coated² scanning mirrors (8) and they are imaged by the telecentric scan (9, $f=50$ mm, LaVision BioTec) and tube (10, $f=180$ mm, LaVision BioTec) lens combination onto the back aperture of the objective lens (12, UPLAPO60XW3/IR with $WD = 0.28$ mm and $NA = 1.2$ or XLUMPLFL20XW with $WD = 2$ mm and $NA = 0.95$, both Olympus). Inside the sample the 2-photon excited fluorescence foci pattern (13) can then be scanned in the focal plane of the objective lens. On their way to the objective lens the beamlets are reflected by a mirror (11) that is installed in the turret of the inverted microscope (IX 71, Olympus). This mirror is therefore easily interchangeable, which is necessary as the choice of this mirror (11) defines the fundamental detection mode of the MPM. If a 100% mirror (11, LaVision BioTec) is chosen, fluorescence that is generated in the sample is reflected back via tube (10) and scan lens (9) onto the scanning mirrors (8). Therefore, fluorescence is guided into the descanned detection path. If a dichroic mirror (11, 680dcspxr, Chroma Technology Corp.) is chosen, fluorescence is detected in the non-descanned detection modes, as VIS fluorescence light passes the dichroic mirror.

In the MPM, sample positioning is performed by a motorized sample stage (Märzhäuser) while the axial position of the focal plane inside the sample is controlled by a mechanical focus drive (MFD, Märzhäuser), moving the objective lens in relation to the fixed sample. Furthermore, as a standard procedure, the excitation wavelength is measured with a spectrometer (Ocean Optics USB 2000, 700 nm - 1140 nm) during laser adjustment and 2PLSM measurements.

3.3.2 Parallel non-descanned camera detection

As can be inferred from figure 3.2 the parallel descanned camera detection is performed by directing the fluorescence light through the dichroic mirror (11) and through a short pass filter (14, E700sp-2p, Chroma Technology Corp.) to the right port of the microscope. This port is selectable by internal microscope mirrors and images through a 180 mm internal tube lens. Fluorescence light is directed through a filter wheel (17, LaVision BioTec) onto a back illuminated EMCCD-camera (18, IXON DV887ECS-UVB, Andor Technology). As the CCD-chip integrates over the exposure time, the orientation of the individual foci in the sample (usually a line) does not have an influence³ on the image

²The original scanning mirrors have been gold coated, but for descanned detection their reflectivity in the VIS fluorescence wavelength spectrum is not sufficient.

³Of course the setup can be misadjusted. If the exciting foci are set too far apart, the outer foci will be vignetted. Also, foci must not overlap because laser intensity might double in the overlap region and can therefore not be considered homogeneous throughout all foci. Furthermore, there is a difference

formation because the foci are scanned through the sample as a complete set. As the pixel size of the camera is $16\ \mu\text{m} \times 16\ \mu\text{m}$, the pixel size in the sample is 266.67 nm for the 60x objective lens and 800 nm for the 20x objective lens⁴.

In case of fluorescence lifetime imaging microscopy (FLIM), a different camera was installed in position (18). It was the Pico Star HR (LaVision) camera system, which consists of a time gated [118] image intensifier and a regular CCD camera Imager QE (LaVision). The advantage of this system is the fact that it is capable of multibeam detection. Therefore, its intrinsic disadvantage of "wasting" most fluorescence photons, due to time gating, and therefore requiring long acquisition times, is compensated for by multiple exciting foci.

3.3.3 Single beam non-descanned PMT detection

Figure 3.2 indicates the non-descanned PMT detection path by a single green line, passing the dichroic mirror (11, Chroma Technology Corp.), the short pass filter (14, E700sp-2p, Chroma Technology Corp.) and an additional focusing lens (15, $f=30\ \text{mm}$, Thorlabs). This lens is necessary because the fluorescence light generated inside the sample has to be directed onto the active area of the PMT (16, H7422-40, Hamamatsu) independent of its origin in the sample. The PMT is a high (peak 580 nm: 40%) quantum efficiency (QE) GaAsP coated detector, which is best suited for very low light applications, as it has a low dynamic range. The PMT's signal is amplified by a I-U-converter (C7319, Hamamatsu) before it is sampled by the A-D-conversion board (DAQ 2204, Adlink) in the measurement control and data acquisition computer. As indicated in Fig. 3.3 a filter wheel (17) can also be placed in front of the PMT. For practical reasons the right port of the microscope is best suited for spectrally resolved (filtered) non-descanned PMT detection.

in fluorescence intensity on the scan region edges, depending on the relative orientation of the foci.

⁴This means that the upper limit for lateral resolution in non-descanned camera detection can be calculated to 532 nm and 1600 nm respectively, due to the influence of camera pixelation. To overcome this limitation, particularly for the 20x objective lens, an additional image magnification by a factor 2.45 can be introduced by adding a negative achromatic lens ($f=-100\ \text{mm}$, ACH 25 X -100 MGF2 TS, Edmund Industrie Optik) in the detection non-descanned path. Of course, the improvement in resolution is then compromised by a smaller field of view on the camera chip and the shift of the imaging plane by 120 mm away from the microscope requires re-adjustment of the camera. The additional lens is installed in the home built prism based spectroscopy housing (s. 3.3.6) and can easily be lowered into the beam path.

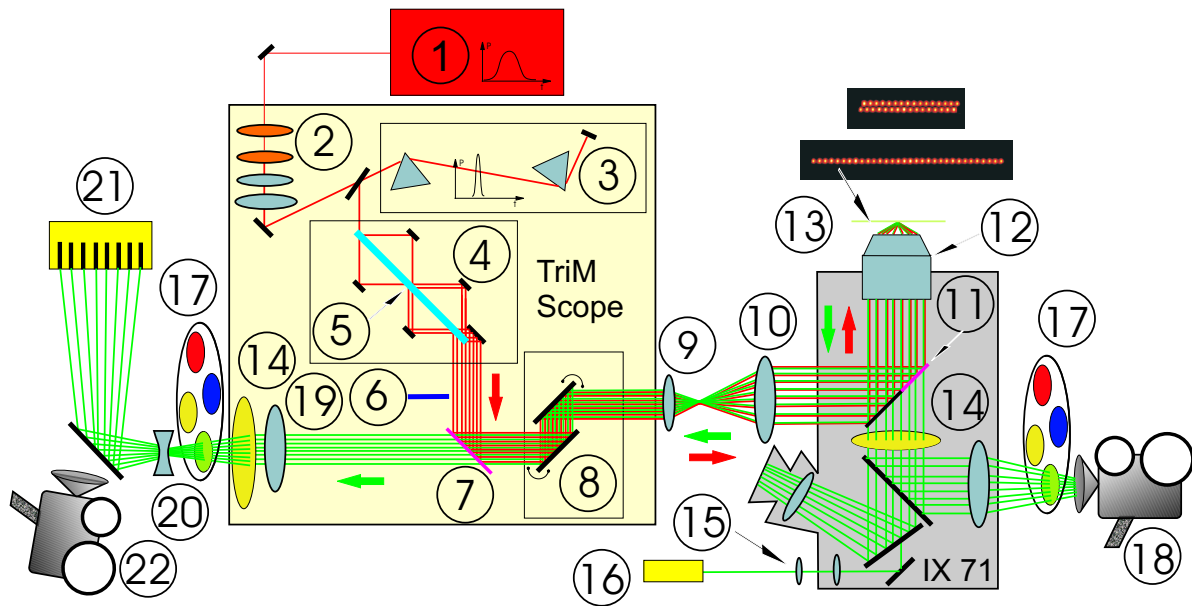


Figure 3.2: MMM imaging modes: 1) Ti:Sa Laser; 2) polarizer/analyzer and beam expansion; 3) pre-chirp section; 4) beam multiplexing section; 5) 50% mirror; 6) laser shutter; 7) dichroic mirror; 8) scanning unit; 9) scan lens; 10) tube lens; 11) 100%/dichroic mirror; 12) objective lens; 13) sample; 14) short pass filter; 15) fucussing lens; 16) PMT; 17) filter wheel; 18) imaging camera; 19) descanned tube lens #1; 20) descanned tube lens #2; 21) pinhole array and multi anode PMT; 22) control camera; unspecified black bars indicate 100% mirrors; additional (tube) lenses inside the microscope are indicated but not specified

3.3.4 Parallel descanned detection

For parallel descanned detection, fluorescence light is directed by a 100% mirror (Fig. 3.2, 11, LaVision BioTec) back onto the scanning mirrors (8). From the scanner it is directed stationarily, i.e. "descanned", through the dichroic mirror (7), through the first achromatic descanned tube lens (19, $f=300$ mm, Linos Photonics) and through the short pass filter (14, E700sp-2p, Chroma Technology Corp.). After passing the optional filter wheel (17) the fluorecence beamlets pass a second negative achromat (20, $f=-50$ mm, Linos Photonics) which is positioned 201.5 mm behind the first tube achromate (19). The combination of these two lenses form an effective focal length of $f=1570$ mm with a focal plane lying 265 mm behind the second tube lens (20)⁵. The pinhole array and 32-fold multi anode PMT (21, H7260-1 Hamamatsu) are located on this focal plane so that the

⁵The complete imaging optics defines a 1884-fold magnification for the 60x objective lens and a 628-fold magnification for the 20x objective lens.

fluorescence foci are imaged stationarily and in focus on the pinholes. This is controlled, especially during the adjustment of the foci onto the pinholes via an observation camera (22). The sizes of the pinholes⁶ may be altered by choosing different pinhole arrays with the same zig-zag pinhole pattern. This is performed by a step motor driven linear shift of the pinhole board. For low light applications it is also possible to completely remove the board in front of the PMT. It has to be noted that in parallel descanned detection 32 slightly shifted images of the sample are generated. This is due to the fact that the 32 exciting foci are separated from each other⁷ and therefore detect different sections of the sample.

The 2PLSM's software (Inspector, LaVision BioTec) currently allows for two different detection patterns. The first pattern performs a stripe scan in the sample. The width of this scan is defined by the width of the scanning foci zig-zag line (17 μm for the 60x objective lens, 51 μm for the 20x objective lens) in x-direction, as scanning is performed by sweeping this line perpendicular to its direction through the sample. This means that each focus scans along the y-direction and the image is generated by placing the linescans next to each other. In this excitation mode, fluorescence images (64 pix x 100 pix) that cover scan regions of 17 μm x 26 μm ⁸ can be generated with approximately 100 Hz.

The second pattern requires scanning of the ROI with every focus of the excitation pattern, implying that the scan region is at least 17 μm wider than the ROI. After defining a shift vector⁹ for each channel, that is dependent on the step width of the scanning mirrors, the individual pixel of the 32 images are added up with respect to the shift vector by an ImageJ macro. To properly align these different images, their size is being doubled before adding them up, so that the pixelation of the final image is 4 times smaller than in the original images.

Currently the sampling rate of the AD-conversion board (theoretically max. 90 kHz for 32 channels, e.g. resulting in one 300x300 pixel image/s) is the practical limitation for frame speed in the setup.

⁶Round pinholes: 0.8 mm, 0.7 mm, 0.6 mm, 0.5 mm, 0.4 mm diameter; elliptic pinholes: 1.3 mm x 0.8 mm, 1.2 mm x 0.6 mm

⁷They form a zig-zag line with a length of 17 μm for the 60x objective lens. This excitation pattern has been chosen to easily adjust the detection path, because neighboring foci are separated more distinctly than in an exciting line of foci and because crosstalk between neighboring foci is smaller.

The excitation pattern has to be adjusted to the detection pinholes.

⁸This size is sufficient to image individual cells for example.

⁹Usually fluorescent beads are imaged and the resulting images are aligned.

3.3.5 General considerations regarding spectral detection

Many analyses of samples in this work are based on spectrally resolved measurements. Upon using fluorescence filters the fluorescence intensity is integrated along its wavelength spectrum and therefore these measurements have to be considered already spectrally resolved. Filtering, in order to distinguish fluorophores, requires emission spectra which are well separated and filter combinations that are tuned to the particular set of fluorophores. If these conditions are fulfilled, filtering¹⁰ is a very efficient choice in LSM because it is relatively fast and the data volume for 3-dimensionally resolved measurements remains relatively small. As the examination of native fluorescence has been a central condition in this work, it has not been possible to choose a certain combination of fluorescent probes and tune the filter set to it. Rather, it was necessary to find out which emission characteristics are present in the samples of interest and simplify the spectral detection as much as possible while still being able to distinguish between the interesting native fluorophores. The basic idea has been to optimize the tradeoff between spectral resolution, data volume, acquisition time, the absence of sample scans (in contrast to beam scans) and the ability to characterize relevant fluorophores.

3.3.6 Non-descanned parallel spectral detection

The experimental setup for non-descanned parallel spectral detection is very similar to the setup in section 3.3.2. As can be inferred from Fig. 3.3 the detection path is directed through the dichroic mirror (14) and the short pass filter into the right port detection path of the microscope. It has to be pointed out that spectral detection in the non-descanned detection path requires a stationary linescan in the sample because this line has to be imaged onto the entrance slit of the spectrograph. The multiplexed fluorescence foci have to be carefully aligned along the scanline defined by one of the scanning mirrors. This way, two different properties of the fluorescence along the linescan are imaged linearly independently on the camera chip. In the direction of the linescan, the fluorescence intensity along this line, i.e. the spatial information, is imaged along the first axis of the camera chip. Perpendicular to this direction, the spectral properties of fluorescence are detected along the second camera axis. This means that a spectral camera image represents an x - λ -scan. To achieve a complete 4-dimensional x - y - z - λ -scan, it is necessary to scan the sample perpendicular (in y -direction) to the linescan (in x -direction) for a x - y - λ -scan in one optical plane (in z -direction). Two aspects of non-descanned parallel spectral detection should be apparent from these explanations:

¹⁰Potentially performed by more than one detector and dichroic mirrors and appropriate filters.

- Sample scanning in y-direction is required. For (biological) samples this an undesirable situation as it might get disturbed by acceleration, slide or positioning accuracy might be a concern.
- Data volume and scan time considerably increases. The latter can especially create a problem, as dynamics in the sample can only be observed with low temporal resolution.

Spectrograph

Two different imaging spectrographs (22) have been used for parallel spectrally resolved non-descanned measurements, a Triax 190 (Jobin Yvon Horiba) with an 100 lines/mm grating resulting in an 200 nm wide spectral range on the camera chip¹¹, or a SpectraPro 2300i (Acton Research Corp.). The gratings of this spectrograph have been chosen to be 80 lines/mm (blaze 870 nm) and 300 lines/mm (blaze 500 nm), resulting in a spectral range of approximately 319 nm and 85 nm, respectively. It has to be mentioned, however, that the transmission characteristics of gratings are wavelength dependent. Especially for wide spectral ranges, this means that obtained spectra are not true emission spectra, rather the device's transmission characteristic is multiplied to the emission spectrum. On the other hand, the spectral dispersion on the CCD-chip is linear and wavelength accuracy is better than 1 nm.

Straight vision prism

Non-descanned parallel spectral detection has also been performed by inserting a straight vision prism (331120, 71 mm, Linos Photonics) in the convergent imaging path of the microscope's right port (s. Fig. 3.3, 22). It has been permanently installed in a manner which allows the user to insert the prism into the detection path without removing the filterwheel (17) with minimal adjustment required. This adjustment is due to a shift in the focal plane by 20 mm away from the microscope. This detection mode uses only one optical element and a linescan as a slit. Its optical losses are minimal and therefore the mode is well suited for weak native fluorescence measurements. Another advantage is the fact that the spectral region to be scanned is selectable by the position of the linescan

¹¹This spectrograph has a focal plane too close to its mechanical housing to image with the C-mount compatible IXON camera that is implemented into the measurement control program. Therefore, it is necessary to insert an additional negative achromatic lens into the spectrograph in order to shift the focal plane further away from the housing. By doing so, the image is spatially and spectrally magnified, which is not desirable in the latter case.

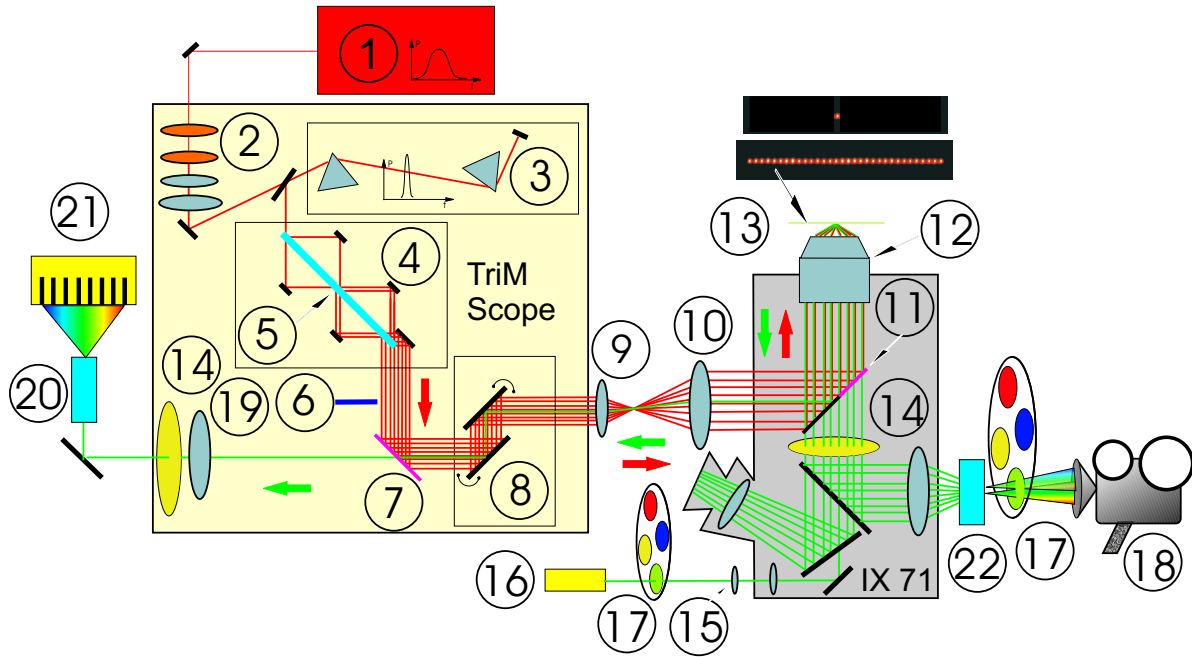


Figure 3.3: MMM spectral detection modes: 1) Ti:Sa Laser; 2) polarizer/analyzer and beam expansion; 3) pre-chirp section; 4) beam multiplexing section; 5) 50% mirror; 6) laser shutter; 7) dichroic mirror; 8) scanning unit; 9) scan lens; 10) tube lens; 11) 100%/dichroic mirror; 12) objective lens; 13) sample; 14) short pass filter; 15) fucussing lens; 16) PMT; 17) filter wheel only relevant with straight vision prism; 18) imaging camera; 19) descanned tube lens #1; 20) spectrograph; 21) multi anode PMT; 22) spectrograph or straight vision prism; unspecified black bars indicate 100% mirrors; additional (tube) lenses inside the microscope are indicated but not specified

on the prism and/or the camera position in spectral direction, as well as the spectral linearity of transmission intensity. However, the non-linearity of the dispersion with respect to the wavelength requires wavelength calibration for each linescan and camera position. This is usually performed by filters¹². The absolute wavelength calibration of this system is indeed its main disadvantage as it is not very precise ($\pm 5\%$) when performed by filters. Another possibility of calibration is to image a microfabricated slit as the sample on the microscope and illuminate this slit with a spectrograph's PMT emission port¹³. Furthermore, the exciting 2-photon focus line has to set to the

¹²Therefore the filterwheel remains in the detection path.

¹³The spectrograph then is used as a wavelength tunable light source. White light is coupled into the spectrograph and only controlled wavelength ranges pass the spectrograph. The wavelength calibration then has a precision of ($\pm 1\%$), which has been tested by using a fixed laser wavelength

slit position after deriving a camera pixel-wavelength calibration curve. The relative wavelength resolution (26.4 % criterion) has been measured (data not shown) by SHG on collagens to be below 4 nm. For the practical goal of distinguishing between different weak fluorophores in a sample, this measurement tool has proven sufficient.

3.3.7 Descanned single beam spectral detection

Spectral detection in the descanned mode is indicated in figure 3.3. A single 2-photon exciting focus is focused by a descanned tube lens (19, $f=300$, Linos Photonics) onto the entrance slit of a spectrograph (20, Spectra Pro 2300i, Acton Research Corp.). The detection is performed by a multi anode 32-fold PMT (21, H7260-1 Hamamatsu) positioned in the focal plane of the spectrograph. Using the 300 lines/mm grating this detection mode covers a spectral range of 332 nm, each segment of the PMT detecting approximately 8.3 nm of the spectrum. This spectral detection mode does not require sample scanning and is relatively fast (for example 400 x 400 pixel scan in 4.5 s). Due to the fact that it generates spectra that consist of 32 data points, the data volume of this measurement mode remains relatively small, allowing for real 3-dimensional spectrally resolved volume measurements.

3.3.8 Multifocal multispectral descanned detection

Figure 3.4 shows the schematic setup for multifocal multispectral descanned detection. Eight fluorescent foci¹⁴ are directed through the two descanned tube lenses (19, $f=160$; 20, $f=-50$, both Linos Photonics), which are spaced 120.5 mm from each other. This results in an effective focal length of 394 mm for the descanned tube lens combination. Before the descanned fluorescence beamlets pass the tube lens combination (19, 20), they are directed through a straight vision prism (21, 331120, 71 mm, Linos Photonics). This prism spectrally splits up the fluorescence beamlets, resulting in eight parallel spectral fluorescence lines. These lines are imaged onto a slit block array in front of a 8x8 multi anode PMT (22, H7546B-20, Hamamatsu), enabling this measurement mode to simultaneously detect eight different joining integrals of the spectrum of eight fluorescence foci without the need to perform sample scanning or turn a filterwheel. The detected

of 532 nm.

¹⁴The beamsplitter in this measurement mode is set to 64 foci, but only every eighth of them is directed into the sample, as three of the 100% multiplexing mirrors are blocked. This technique is used because it requires a smaller magnification by the descanned tube lenses (19, 20) and therefore, a shorter optical path, which results in better imaging quality.

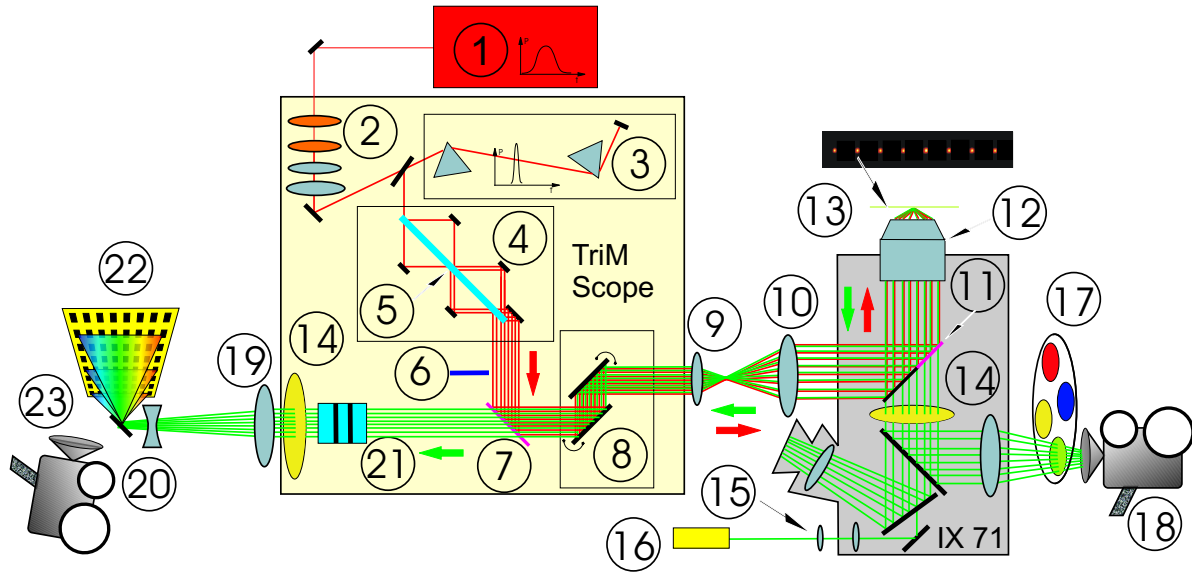


Figure 3.4: Descanned multifocal multispectral detection: 1) Ti:Sa Laser; 2) polarizer/analyzer and beam expansion; 3) pre-chirp section; 4) beam multiplexing section; 5) 50% mirror; 6) laser shutter; 7) dichroic mirror; 8) scanning unit; 9) scan lens; 10) tube lens; 11) 100%/dichroic mirror; 12) objective lens; 13) sample; 14) short pass filter; 15) focusing lens; 16) PMT; 17) filter wheel; 18) imaging camera; 19) descanned tube lens #1; 20) descanned tube lens #2; 21) straight vision prism; 22) multi anode PMT; 23) control camera; unspecified black bars indicate 100% mirrors; additional (tube) lenses inside the microscope are indicated but not specified

spectral range depends on the relative position of the PMT with respect to the beam path and prism position and therefore may be altered according to the emission characteristics of the sample. As a result eight spectrally resolved images of slightly shifted sample regions¹⁵ are generated and added up after the measurement, maintaining the spectral information. This is due to the fact that only corresponding spectral ranges of the eight foci are added, i.e. (shifted) columns of the PMT. As in parallel descanned detection, a shift vector for the eight foci has to be determined with respect to the particular stepwidth of the scanning mirrors in order to properly align the eight individual scan regions.

¹⁵As in parallel descanned detection, this is due to the fact that the exciting foci are separated from another.

3.4 Pa-GFP measurements

Pa-GFP measurements have essentially been performed in the parallel non-descanned camera detection mode (s. section 3.3.2) with the UPLAPO60XW3/IR objective lens. A schematic of the measurements is presented in figure 3.5. For some measurements, two Ti:Sa lasers (1a, Tsunami & Millennia X, 920 nm, both Spectra Physics; 1 b, 800nm, prototype Gigajet 20c, Gigaoptics), selectable by shutters (2), have been used because rapid switching between two wavelengths (800 nm and 920 nm) is required. Alternatively motorized setting screws on the wavelength adjustable laser (1a, Tsunami) performed wavelength selection within approximately 4 s between 800 nm and 920 nm. Upon using both lasers, they have been coupled into the TriM-scope (4) on the same optical path by a dichroic mirror (3, z860lp, Chroma Technology Corp.).

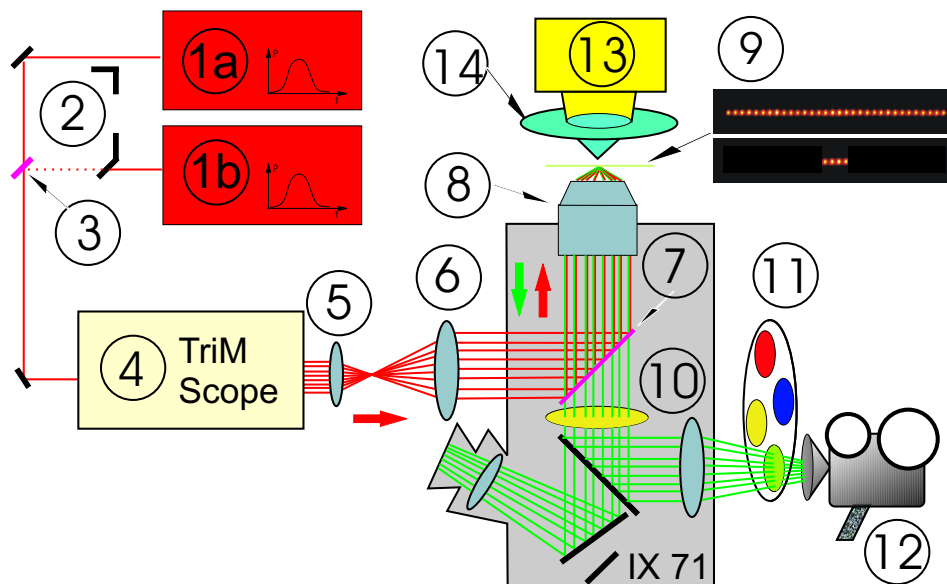


Figure 3.5: Measurement setup for Pa-GFP expressing cells: 1a) Ti:Sa Laser; 1b) Ti:Sa Laser; 2) shutter; 3) dichroic mirror; 4) scanning and multiplexing unit; 5) scan lens; 6) tube lens; 7) dichroic mirror; 8) objective lens; 9) sample; 10) short pass filter; 11) filter wheel; 12) imaging camera; 13) Hg fluorescence lamp; 14) band pass excitation filter; unspecified black bars indicate 100% mirrors; additional (tube) lenses inside the microscope are indicated but not specified

Additionally, fluorescence trans-detection has been performed using a fluorescence lamp (13, HBO 50, Zeiss) and an appropriate excitation filter (14, HQ480/20, AHF analysentechnik AG) for 1-photon excitation of Pa-GFP. Time resolved fluorescence microscopy using Pa-GFP as a selectable fluorescent probe has been performed in order to reve-

al the dynamics of the LCL1 nuclear export in tobacco BY-2 protoplasts. To achieve spatio-temporal information on the MYB transcription factor LHY/CCA1-like 1 (LCL1) transfected cells have been identified by trans-fluorescence 1-photon microscopy, tuned to the excitation/emission characteristics of DsRed, which had been tagged to the prenylated Rab acceptor 1 (Pra1; At2g38360). As Pra1 is a membrane-localized protein that groups in speckles around the nuclear envelope, DsRed fluorescence has indicated on the one hand a successful transfection of Pa-GFP in the protoplast and on the other hand it has marked the cell's nucleus. Therefore, "aiming" at the nucleus for 2-photon activation of Pa-GFP has been enabled after performing 3-dimensional wavelength resolved (DsRed and Pa-GFP) MPM at 920 nm excitation wavelength. These scans have revealed the cell's morphology, usually only by the red DsRed fluorescence, because Pa-GFP had not been activated yet. Therefore its fluorescence intensity usually did not exceed the background intensity level. Activation of Pa-GFP has been narrowed to the cell nucleus by choosing a scan region only inside the nucleus. Activation in z-direction is limited to the focal volume of the objective lens, here to approximately $1 \mu\text{m}$ at 800 nm wavelength. By reducing the number of exiting foci to 4 or 8^{16} , controlled activation of Pa-GFP only in the nucleus is guaranteed. In general the activated regions have covered areas of 50 to $70 \mu\text{m}^2$ depending on the nucleus dimension. The power of the activation laser bursts varied between 30 mW to 70 mW equally distributed in the exciting foci. The practical result of this procedure is that fluorescence of Pa-GFP can be selectively "switched on" in the cell nucleus. Within up to six seconds, Pa-GFP throughout the cell nucleus is activated due to fast diffusion within the nucleus. After the activation, Pa-GFP distribution and therefore protein dynamics (here: LCL1 and LCL(NESm)) fused to Pa-GFP have been monitored. Three protocols have been applied in protein dynamics measurements.

- Simultaneous 2-photon activation and trans 1-photon fluorescence microscopy: Classical 1-photon fluorescence, induced by a fluorescence lamp in combination with an appropriate excitation filter, has been monitored in non-descanned camera detection. Here a filter cascade of two emission filters (HQ 525/50 and HQ510/20) to effectively block out exciting light has been introduced in the detection path. In this measurement mode it is possible to monitor Pa-GFP fluorescence, while 2-photon activation of Pa-GFP at 800 nm is performed via the dichroic mirror in the typical non-descanned detection manner.

¹⁶This is necessary, because the line of foci gets longer than the nucleus dimension if more than 8 exciting foci are selected.

- Subsequent 2-photon activation and 2PLSM by using two Ti:Sa lasers at 800 nm and 920 nm: The activation of Pa-GFP has been performed by the first Ti:Sa laser (prototype Gigajet 20c, Gigaoptics) and subsequent scanning of the entire cell by the second Ti:Sa laser (Tsunami, Spectra Physics) at 920 nm has detected the protein dynamics. On the one hand this protocol provides 3-dimensional optical sectioning in the imaging plane in combination with a very good signal to background ratio, because 2-photon induced fluorescence is detected in epi-direction. On the other hand, this protocol generates an observation gap of approximately 5 s, because new scanning parameters (number of beams and scan region) have to be set and the exciting laser has to be reset by a shutter.
- Subsequent 2-photon activation and 2PLSM by switching the wavelengths of one Ti:Sa laser between 800 nm and 920 nm: By motorized setting screws the wavelength of the Tsunami Ti:Sa laser can be adjusted between 800 nm and 920 nm in approximately 4 s. Therefore an activation and detection cycle has basically the same properties as the two laser cycle described above. In particular there is also a 5 s observation gap between activation and detection in this measurement protocol.

The fluorescence decay in the cell nucleus and the distribution of activated Pa-GFP throughout the cell's cytoplasm has been measured by a time series of fluorescence images after activation. The intensity analysis has been performed by choosing a ROI inside the nucleus and by measuring the average intensity in this ROI with the ImageJ "z-profiler" plugin. Furthermore a final 3-dimensional, spectrally resolved 2PLSM scan completed the measurement, in order to document the steady state distribution of proteins in the cell.

3.5 The versatile experimental setup

As can be inferred from a comparison of the different schematics of measurement modes (Fig. 3.2, 3.3 and 3.4), some of the measurement modes do exclude each other. Therefore, for an unknown new sample there is a flexible setup, which allows for relatively fast changes between the measurement modes, depending on the sample's fluorescence characteristics. In non-descanned detection, the single beam detection PMT is installed without a filter wheel on the left port of the microscope (s. Fig. 3.2, 16), while the right port is equipped with the filter wheel and the non-descanned camera (s. Fig. 3.2, 17, 18). Changes between the modes only require the selection of the different microscope's

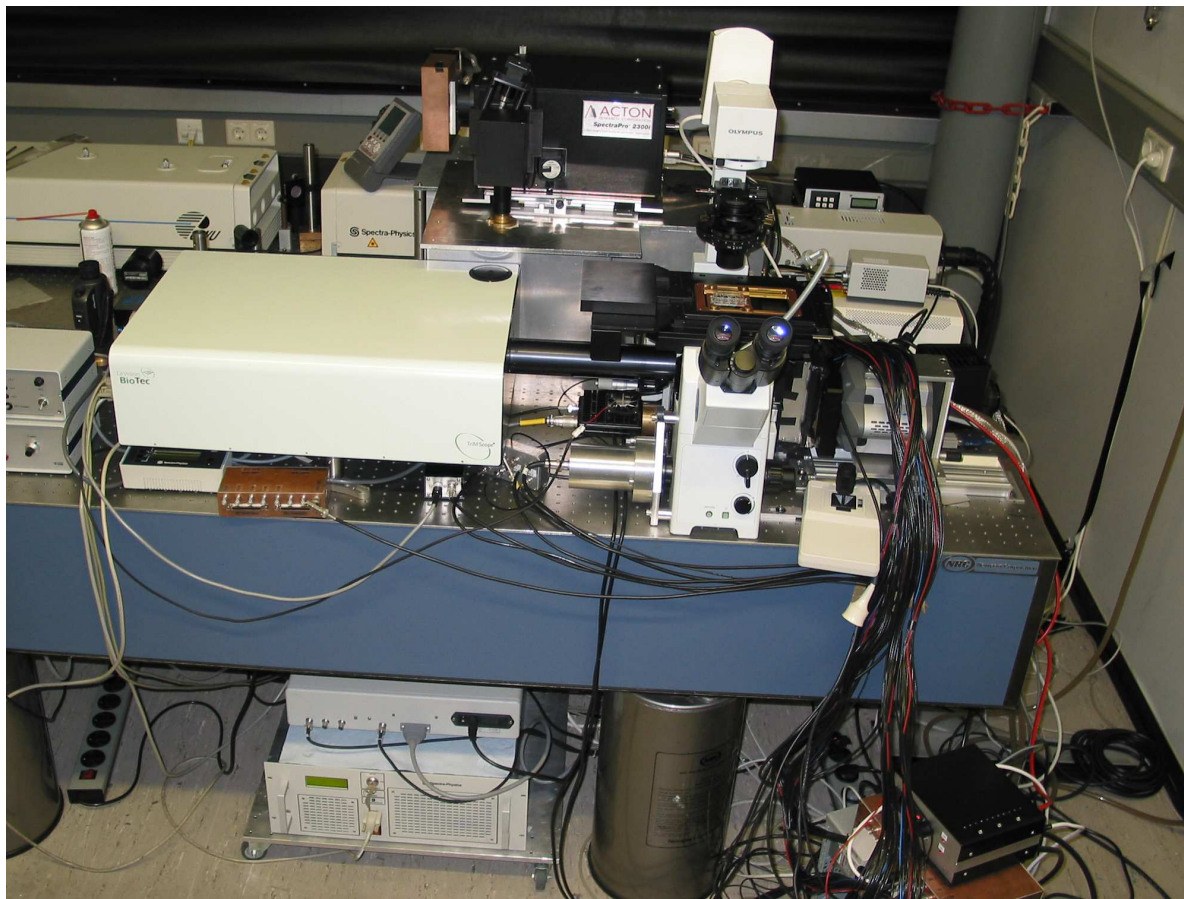


Figure 3.6: The experimental setup

ports and the correct measurement parameters in the software settings. If necessary, the straight vision prism can be inserted into the non-descanned camera detection path (s. Fig. 3.3, 22) and spectrally resolved measurements can be started after adjusting the camera position, i.e. within a few minutes. In descanned detection, it is convenient to have the multifocal multispectral measurement mode installed (s. Fig. 3.4). If single beam spectral descanned detection is required (s. Fig. 3.3), only the first descanned tube lens (s. Fig. 3.3, 19) has to be adjusted correctly and an additional mirror has to be inserted into the descanned detection path. This is due to the fact that the rather large spectrograph and the multi anode PMT (s. Fig. 3.3, 22, 21) can be positioned on top of the multifocal multispectral descanned detection mode housing. Figure 3.6 shows this combination of measurement setups.

3.6 Multi anode PMT electronics

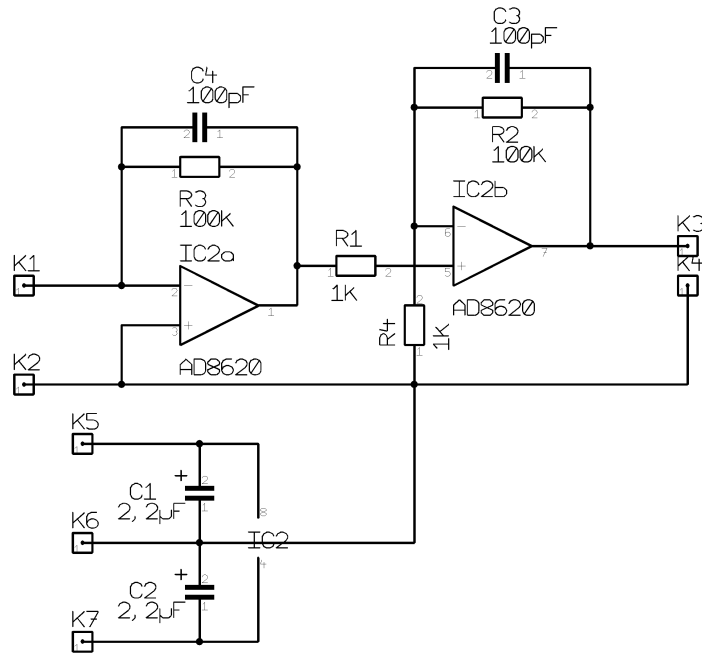


Figure 3.7: Circuit of PMT amplifier for one anode

The use of the two multi anode PMTs (H7260-1 and H7546B-20 both Hamamatsu) in parallel descanned detection, requires a suitable amplification and sample-and-hold electronics, as the individual channels are sampled by a multiplexed AD-conversion board (DAQ 2204, Adlink). The first component of the detection electronics, is an inverting transimpedanz two stage amplifier for each individual channel of the PMTs (s. Fig. 3.7). All 32 (64 respectively) amplifiers are located directly on the PMT's connector circuit board. The operational amplifiers (AD8620) used for these circuits have particularly low offset voltages and low thermal drift. This is an important feature, as the second stage of the complete detection electronics consists of a dual integration electronics (s. Fig. 3.8), which integrates the amplified PMT anode's currents during two read-outs of the AD-conversion board. This integration has to be performed, because during the delay times between two read-outs, i.e. the time while the other 31 (63 respectively) channels are being sampled, fluorescence photons can not contribute to the generation of a fluorescence image, although they are being detected. This should be evident from Fig. 3.9, which shows an oscilloscope screenshot. A typical one photon detection event occurs on PMT anode # 2 and it is recorded on the oscilloscope's channel 1. When comparing the

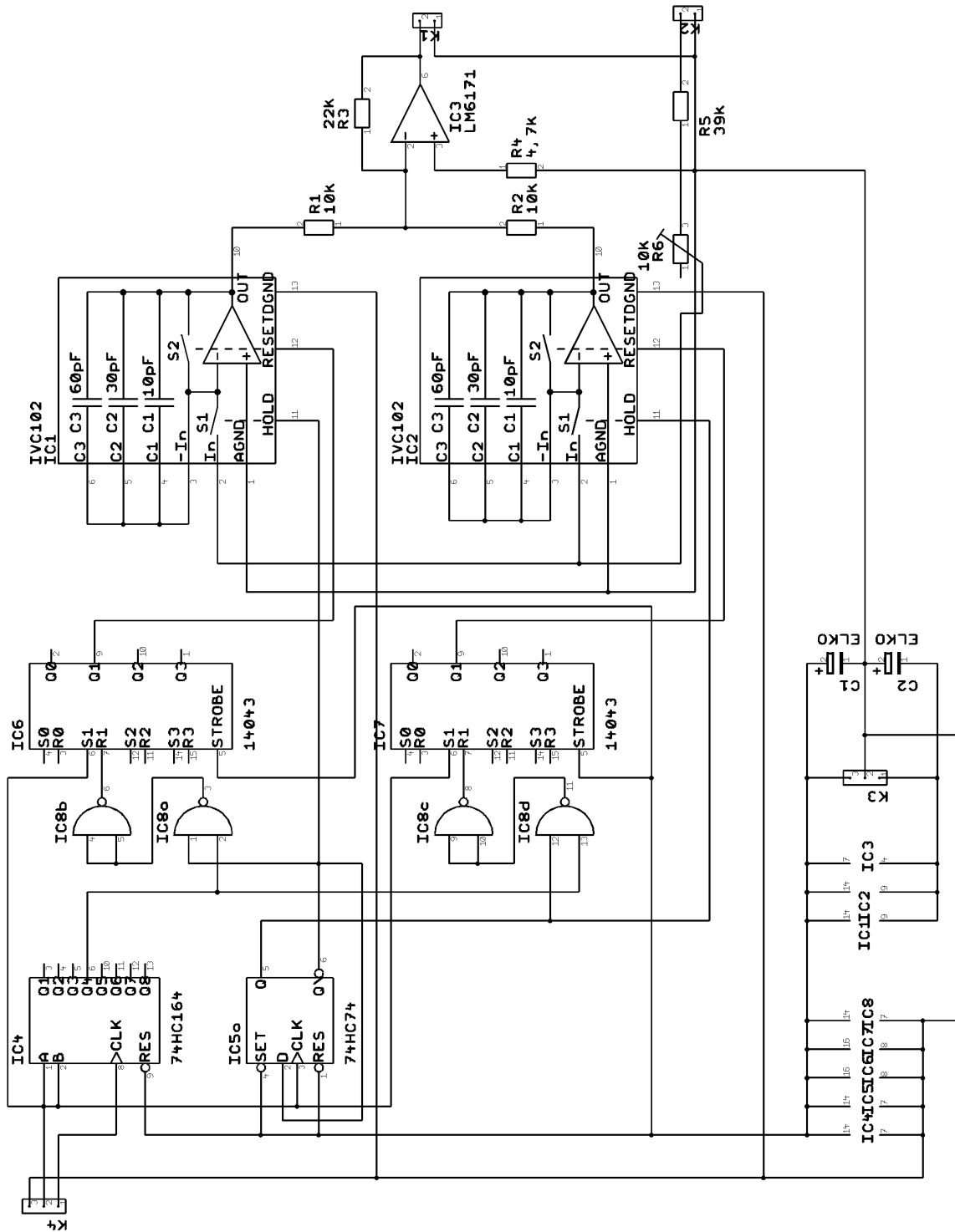


Figure 3.8: Circuit of PMT integrator for one channel. Central elements are the two integrators IVC102 by Burr-Brown. They are integrated circuits, containing an operational amplifier, capacitors and digital switches.

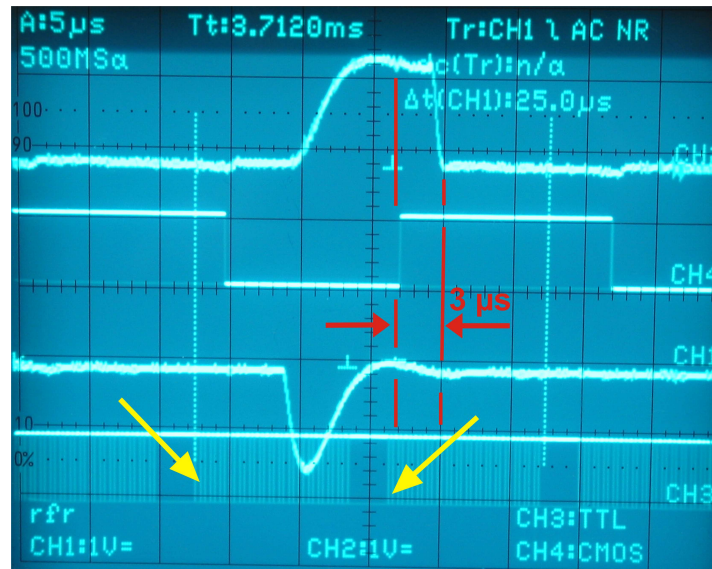


Figure 3.9: Oscilloscope screen shot of relevant signals: channel 1 amplified PMT signal (anode #2), single photon event; channel 2 integrated signal; channel 3 AD-conversion trigger signal; 4 "select" signal for dual integration circuit; yellow arrows indicate sample trigger for channel #2; erase time indicated by red lines

trigger signals for AD-conversion, generated by the AD-conversion board, one can easily see that the photon detection event falls between two AD-conversion triggers (arrows in Fig. 3.9) for PMT anode # 2. This photon signal would have not been sampled. The integrated signal (oscilloscope's channel 2) is however present at the moment of sampling. After sampling, it is deleted, which takes about $3 \mu s$. During the erasing cycle, the second integrator circuit for channel # 2 is active. The selection of the different integrators (s. Fig. 3.9, channel 4) is performed by digital counter electronics, the time-base of which is the AD-conversion trigger from the AD-conversion board. Therefore, the integration electronic is automatically triggered by software.

3.7 Software

Measurement control and data analysis, in particular spectral unmixing and fluorescence decay time fits for FLIM measurements are performed with Inspector (LaVision Bio-Tec). Image addition and various other analyses are performed with ImageJ [119] and necessary the plugins and macros for ImageJ. 5-dimensional representations (including spectral and temporal axis) are performed with Imaris 4 (Bitplane). Representations of

spectra and fluorescence intensity decay curves and fits for these measurements are performed with Origin 6.0 (Microcal). Theoretical PSFs have been calculated with Matlab 6.5 (Mathworks). The SpectraPro 2300i spectrograph has been controlled by its driver software SpetraPro Vision 3.33 (both Acton Research Corp.).

3.8 Spectral unmixing

Spectral unmixing is a powerful tool to differentiate between fluorophores/components on the basis of their emission characteristics. The basic idea of spectral unmixing is a test on linear dependence. Because emission spectra of different fluorophores often do overlap, for a certain wavelength(range) it can not be decided to which fluorophore the emission intensity has to be assigned to. In spectral unmixing the spectral emission characteristics of every pixel in an image is compared to example spectra by determining the proportional share of all example spectra to the particular pixel's spectra. After determining a best fit, the coefficients of contribution are assigned to corresponding pixels in images that represent the different example spectra [39, chap. 36]. For the fundamental idea it does not matter whether the spectral differentiation is based on emission spectra or just on different filtered images. The advantage of this tool is its relative insensitivity towards overlapping emission characteristics, even if they differ considerably in intensity. The Imspector (LaVision BioTec) software package is equipped with this image processing option. Figure 3.10 a, b and c show different spectral emission channels which all show both, chondrocytes (round objects in lacunae) and ECM (unstructured background). In figure 3.10 d all of these channels have been overlapped and chondrocytes can be easily recognized, because they are present in all channels. The two indicated areas (A and B) are the origin for a spectrally resolved comparison of absolute intensities in figure 3.10 e. On the basis of these linear independent (with respect to the different emission filters) intensities the image has been spectrally unmixed (s. Fig. 3.10, f). This image clearly exhibits chondrocytes (red) embedded in ECM (green). The main advantage of this image, next to slightly improved contrast in comparison to figure 3.10 d, is the fact that chondrocytes and ECM now are represented in two different channels, meaning they are functionally separated. The data set used in this example for spectral unmixing is also the basis for further investigations presented in section 4.1.2.

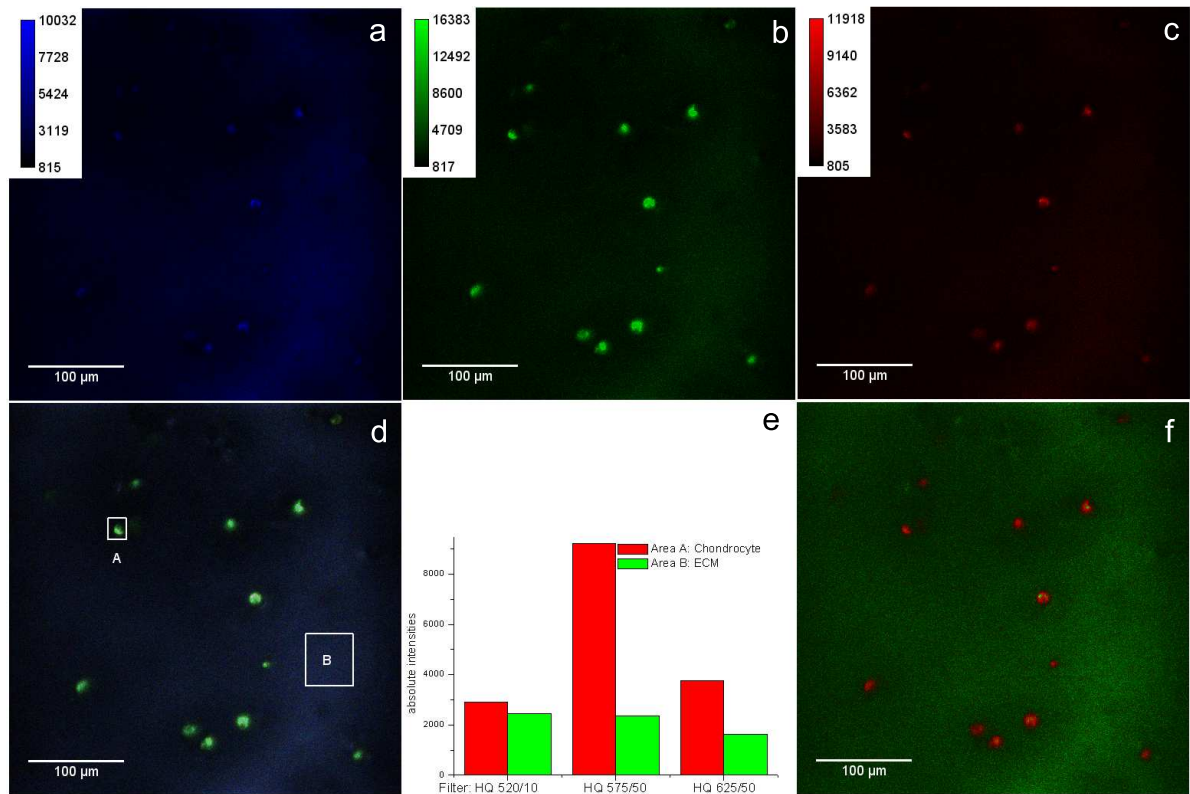


Figure 3.10: 2-photon induced fluorescence of human cartilage: a) emission filter HQ 520/10; b) emission filter HQ 575/50; c) emission filter HQ 625/50; d) composite image of a), b), c), area A shows chondrocyte, area B shows ECM; e) absolute intensities of area A and B; f) spectral unmixing result on the basis of intensities presented in e), chondrocytes in red and ECM in green; all images in minimum-maximum representation, excitation wavelength 800 nm

4 Results

4.1 Cartilage

It is of great interest for MACI procedures to evaluate the quality of the basic biopsy material: the cartilage. Not only is the number of chondrocytes derived from a biopsy crucial for the successful construction of the tissue engineered implant, but it is also necessary to evaluate the arthrotic state of the cartilage. Presently, a sufficient number of chondrocytes for the MACI treatment is guaranteed by a minimal volume that the surgeon has to extract in the initial biopsy. This procedure does not account for individual variations in chondrocyte density in the cartilage or compromised chondrocyte viability. The characterization of the cartilage's arthrotic state is performed by the surgeon during the biopsy. As long as the surgeon does not diagnose osteoarthritis, the cartilage's state has no influence on the following treatment. In reference to the first 2PLSM approved for clinical use (DermaInspect, JenLab), which is currently used for multiphoton tomography of the human skin, it is interesting to evaluate information that can be gathered on unstained and unfixed cartilage.

4.1.1 Bovine cartilage

The examination of functionally labeled bovine cartilage with 2PLSM at Bielefeld University has been extensively documented in [92]. Native fluorescence of osteoarthrotic bovine cartilage (s. Fig. 4.1) has been examined because in addition to the principal benefits of using unstained samples, fluorescent labeling of cartilage particularly revealed problems with a homogeneous distribution of the dye throughout the full thickness of the sample. Figure 4.1 A displays the chondrocyte distribution throughout the examined volume ($595 \mu\text{m} \times 572 \mu\text{m} \times 460 \mu\text{m}$). Especially in individual optical planes (s. Fig. 4.1, B, C) their position in the lacunae, as well as their grouping in lines can easily be inferred. Furthermore, the fibrillation of the ECM in degenerative cartilage [120] can be inferred from figure 4.1, C by the diagonally oriented increased fluorescence intensity. The high imaging depth ($460 \mu\text{m}$) that has been achieved without considerable attenua-

tion of fluorescence intensity in deeper optical layers (note intensity scales in Fig. 4.1, B and C) indicates a reduced ECM density, again in keeping with the characteristics of osteoarthritis. These interpretations of the 3-dimensionally imaged cartilage sample would already provide valuable additional relevant information about the sample, if it was to be used in a MACI tissue engineering process. Especially because no staining has been required and because the sample has been kept in physiological buffer solution (Ringer solution), it maintains its capability to serve as a resource for chondrocytes.

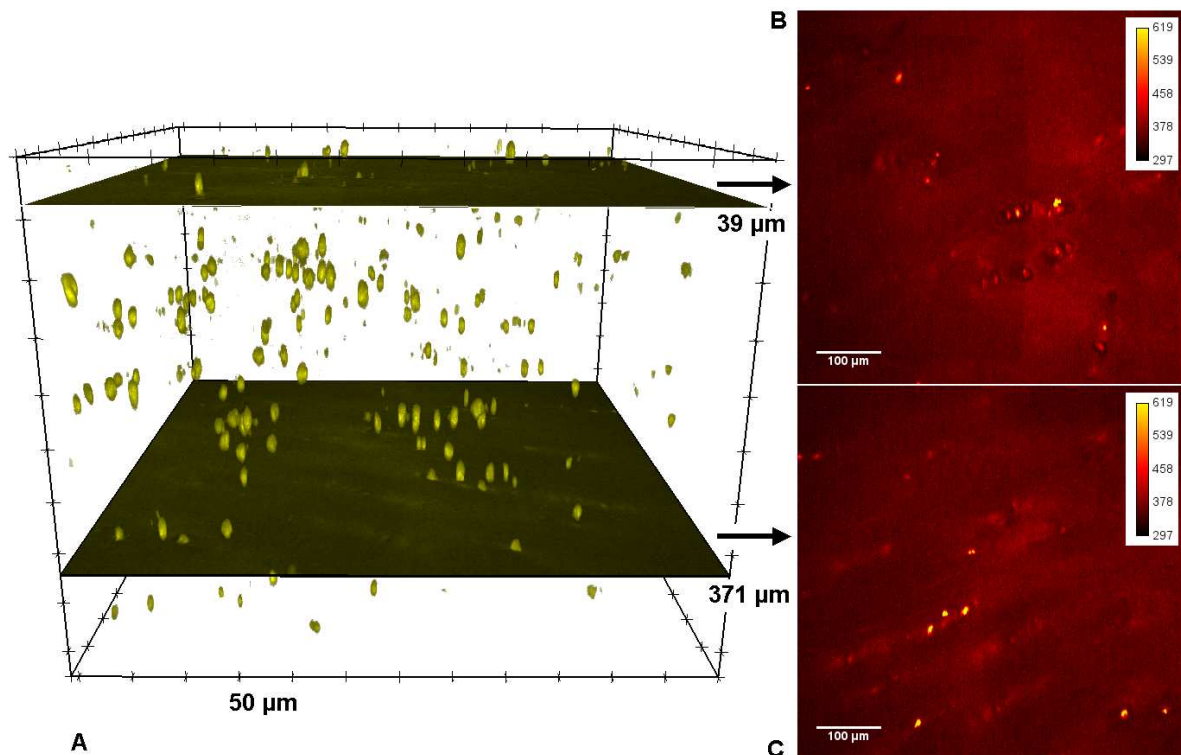


Figure 4.1: Native 2-photon induced fluorescence of osteoarthrotic bovine hyaline cartilage: Excitation wavelength 800 nm, single beam non-descanned PMT detection, no emission filter, data set contains optical planes down to 460 μm inside the sample; A) voxel representation of the complete data set, lower limit threshold 454 counts to exclusively show chondrocytes, gridlines on coordinate system 50 μm , clipping planes at 39 μm and 371 μm depth indicate optical planes B) and C)

4.1.2 Human cartilage

Unstained healthy and osteoarthrotic human hyaline cartilage have been examined with 2PLSM [121, 120]. Special care has been taken to keep laser power at 800 nm under 5

mW (240 mW for 64 foci) per focus [55]. In figure 4.2 the autofluorescence images, filtered by a HQ525/50 emission filter, of the two macroscopically diagnosed samples of the same female test person are compared. The non-arthrotic sample (Fig. 4.2, A) clearly exhibits a considerably higher (3-fold) autofluorescence than the arthrotic one (Fig. 4.2, B). This indicates a higher ECM density in non-arthrotic cartilage. Furthermore, it is evident that the two surface structures significantly differ in respect to smoothness and morphology. While the healthy cartilage surface is smooth and isotropic, the arthrotic one has a rough, fibrous surface. This is consistent with increased friction, wear and algetic exposure upon using the joint, which are typical symptoms of osteoarthritis. This direct comparison of healthy and osteoarthrotic cartilage by 2PLSM clearly indicates, that this method is potentially suitable for future diagnostic applications, not only for quality control of cartilage biopsies used in autologous transplantation protocols, but also as an evaluation tool for arthrotic states in general.

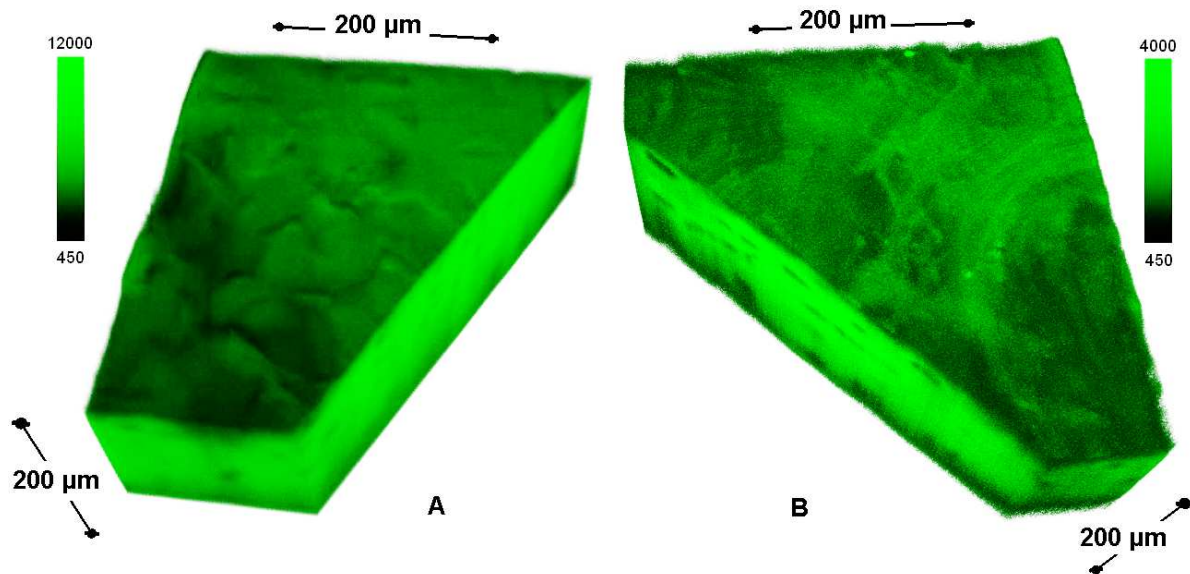


Figure 4.2: Native 2-photon induced fluorescence of human hyaline cartilage of the same test person: Excitation wavelength 800 nm, 240 mW, 64-foci parallel non-descanned camera detection, HQ525/50 emission filter, voxel representation of the complete data set, A) non-arthrotic (macroscopical diagnosis), B) arthrotic (macroscopical diagnosis)

Furthermore, unstained cartilage has been examined to derive a functional characterization of its components on the basis of the emission characteristics of ECM and chondrocytes [122]. This characterization is possible with appropriate emission filters and spectral unmixing of the autofluorescence data as it has been already presented in

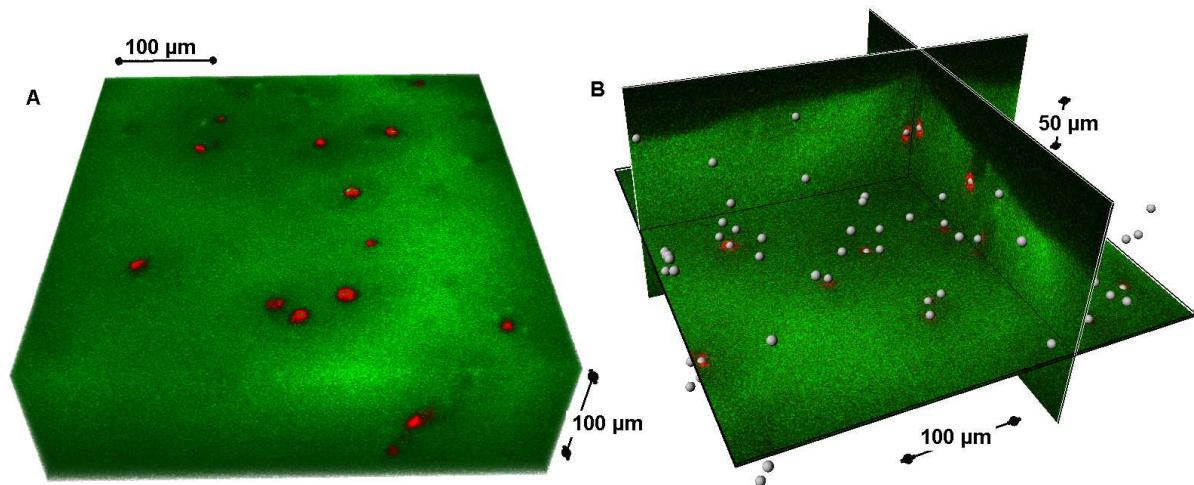


Figure 4.3: 2-photon induced autofluorescence of human cartilage: A) voxel representation of spectrally unmixed data set, top optical plane identical to Fig. 3.10 f; B) chondrocyte distribution in the sample, white balls represent automatically detected chondrocytes

section 3.8. On the basis of the spectrally unmixed data (s. Fig. 4.3, A), it was possible to detect chondrocytes in an automated manner, using the spot detection option of the Imaris 3D-presentation software. Figure 4.3 B shows the detected chondrocytes, represented by white balls. To compare the position of some of the successfully detected cells, three additional clipping planes were added to the detected cells. These planes indicate the outer limits of the ECM (green) on the one hand, but also show spectral unmixing positions of some of the cells as red coronas around the balls. Furthermore the green ECM channel was rendered by Imaris to measure the volume of investigated cartilage. The chondrocyte density for this sample has been calculated to be approximately $3000 \frac{\text{cells}}{\text{mm}^3}$. Depending on different positions in relation to the bone, but also on differences between individuals, chondrocyte densities roughly vary between $2,000 \frac{\text{cells}}{\text{mm}^3}$ and $25,000 \frac{\text{cells}}{\text{mm}^3}$ [97]. The automated calculation of chondrocyte densities shows another potential use of 2PLSM following biopsy to derive cartilage samples for autologous transplantations procedures. If cell densities could be calculated in a non-destructive manner on the site of surgery, the amount of biopsy material could be adjusted to the need for reimplantation purposes.

4.2 Chondrocytes on I/III-collagen membranes

4.2.1 Emission spectra

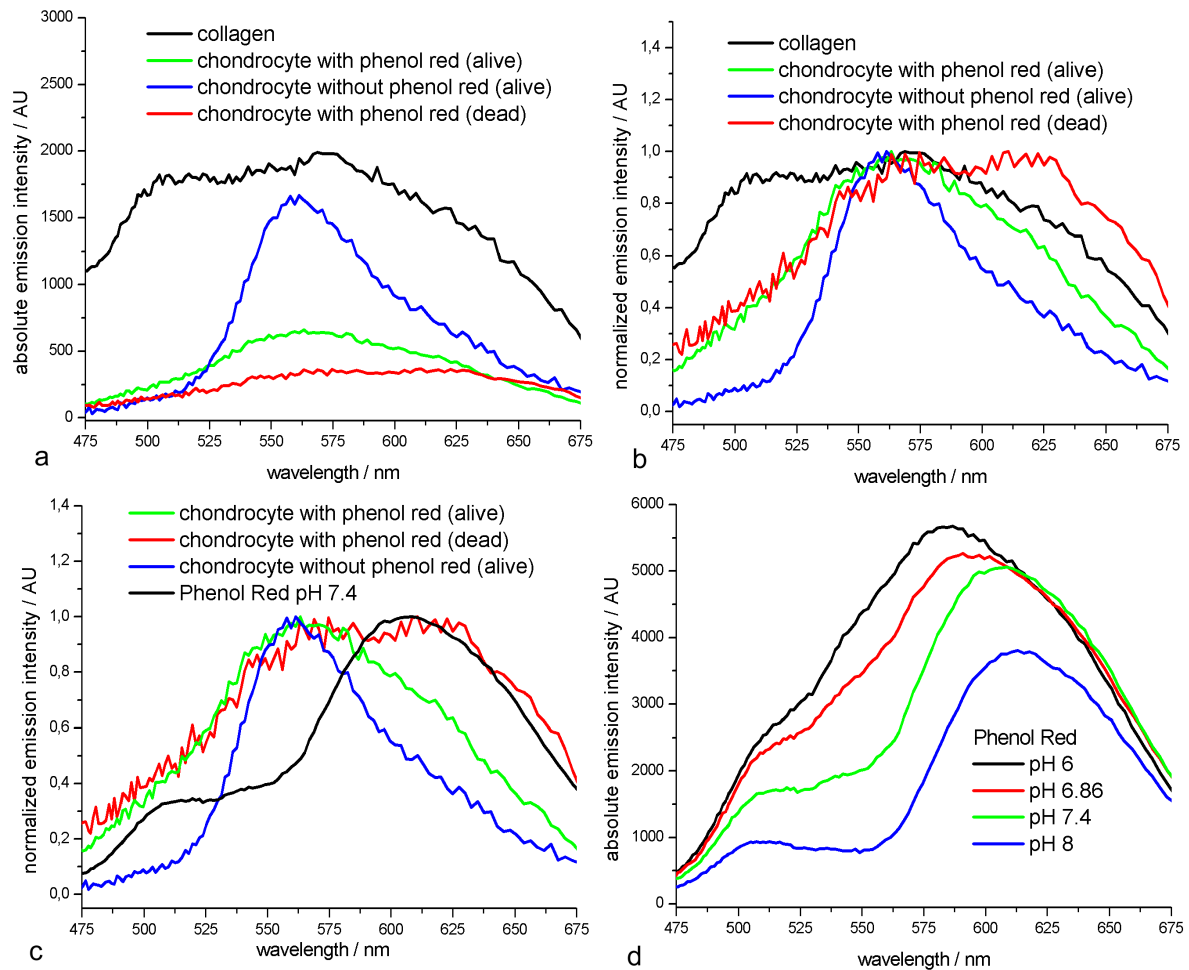


Figure 4.4: 2-photon induced emission spectra: excitation at 800 nm, non-descanned prism based spectral detection, wavelength calibration accuracy $\pm 5\%$, collagen emission spectrum derived from region d in Fig. 4.12 B, chondrocyte with Phenol Red (alive) emission spectrum derived from region a in Fig. 4.12 B, chondrocyte with Phenol Red (dead) emission spectrum derived from region c in Fig. 4.12 B, chondrocyte without Phenol Red (alive) emission spectrum derived from region d in Fig. 4.8 a; a) absolute emission spectra; b) normalized emission spectra; c) comparison of normalized emission spectra; c) pH-dependent Phenol Red emission spectra

In figure 4.4 fluorescence emission spectra of components that have been identified as relevant for the cell populated collagen membranes' fluorescence are presented. This iden-

tification represents a major contribution to the optical characterization of chondrocytes and collagen membranes. A comparison of the spectra with published 2-photon induced emission spectra (s. Fig. 1 in [28]) clearly indicates that Riboflavin is the main source of the chondrocyte's autofluorescence. Among others, Nicotinamide Adenine Dinucleotide (NADH) has also been reported as a source of cells' autofluorescence [28, 123], but in the case of chondrocytes it did not make a considerable contribution¹. The emission spectra in figure 4.4 suggest that chondrocytes and collagens should be easily distinguishable by the use of emission filters and spectral unmixing because they clearly show differences in the spectral range of 475 nm to 515 nm, while both fluorophores exhibit overlapping fluorescence signal between 550 nm and 600 nm² [124]. As presented in sections 4.2.2, this is indeed the case. The presence of Phenol Red in the cell culture medium, which applies to most of the examinations of collagen membranes, does cause difficulties in the characterization of collagens and cells. As can be induced from figure 4.4 b the chondrocytes emission spectrum changes into a broadened one that is barely distinguishable from collagen's emission spectra through the use of emission filters only. Using complete 3-dimensionally resolved emission spectra, a characterization is possible (s. section 4.2.3) but data volume and acquisition time becomes a problem in these measurements. On the other hand, Phenol Red in the cell culture medium is a standard procedure in cell cultivation performed by the project partner IBA and furthermore provides additional information on the cells as presented in section 4.2.3. Hence, functional imaging of collagen membranes is also desirable for culture conditions that include Phenol Red. The following section will now deal with spectral characterization techniques that have been successfully tested on the two different types of collagen I/III-membranes populated with chondrocytes.

4.2.2 Cell culture conditions without Phenol Red

Collagen membranes and chondrocytes populating them could be spectrally distinguished by the use of filters, when the cell culture medium did not contain Phenol Red.

¹From the absorption spectra in Fig. 1 in [28] it is evident that for 800 nm excitation wavelength the action cross-section of NADH is smaller than the one of Riboflavin by a factor of 500. As the TriM-scope's operative wavelength range is 760 nm to 960 nm, a considerable share of NADH fluorescence has not been detected because shorter excitation wavelengths would be required.

²Such a spectral overlap is a good example for the usefulness of the spectral unmixing algorithm. Just by representing the fluorescence data of each emission filter with a different color would render chondrocytes barely visible, as their *absolute* peak fluorescence emission is only approximately a fourth of the collagen's peak fluorescence emission (s. Fig. 4.4, a).

As using fluorescence emission filters allows for non-descanned camera detection with multiple foci, such a measurement takes relatively little time (< 10 min) and contains an acceptable data volume (< 1 GB). Therefore 3-dimensional image stack down to a depth of approximately $250 \mu\text{m}$ for fleece membranes and $70 \mu\text{m}$ for sponge-like membranes can be generated with stepwidths between $1 \mu\text{m}$ and $2 \mu\text{m}$.

Sponge-like collagen membranes

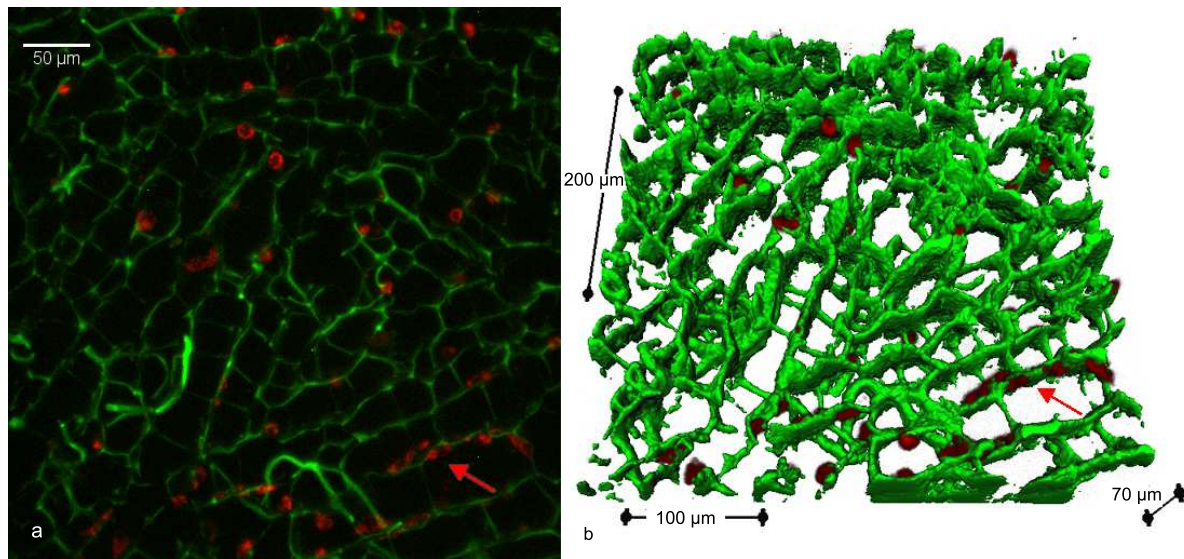


Figure 4.5: 2-photon induced autofluorescence of sponge-like collagen membrane populated with bovine chondrocytes: 790 nm excitation, 320 mW, 64 foci; objective lens: XLUMPLFL; non-descanned camera detection, 465 ms/frame; spectral unmixing result base on emission filter HQ475/50, FF01-525/30, FF01-560/25, HQ605/55, HQ625/50 and unfiltered; imaging depth down to $70 \mu\text{m}$ a) maximum intensity projection of spectrally unmixed data set, green: collagen, red: chondrocytes ; b) green collagen unmixing channel rendered, red: voxel representation of chondrocytes

In figure 4.5 the superficial $70 \mu\text{m}$ of a cell populated sponge-like collagen membrane are presented. Other measurements have revealed that chondrocytes do not considerably migrate into this type of membrane (pore size $10 \mu\text{m}$ to $40 \mu\text{m}$) much deeper than $50 \mu\text{m}$ (s. Fig. 4.11 a, b). The chondrocytes in figure 4.5 are generally evenly distributed throughout the examined area and distinguishable from each other. In different sections of the same membrane they either cluster in several layers on the outer surface of the sample (s. Fig. 4.11 a), or (almost) no chondrocytes are present. Another characteristic

of the chondrocytes is their shape. In many cases they form an ellipsoid. Usually the longest axis follows the direction of a collagen fiber and may be as long as 20 μm . All of the 65 chondrocytes (counted by Imaris spot detection option) in figure 4.5 have this elongated shape, although most of them appear as circles. This is due to the fact that both images mainly represent the lateral extension of the data-stack, while the chondrocytes are elongated along the axial direction of the data-stack following the collagen "tube walls". The elongated chondrocytes can be recognized best in the regions indicated by an arrow.

Fleece collagen membranes

The advantage of reduced data volume is especially important when imaging cell populated fleece membranes, because the 3-dimensional distribution of chondrocytes on these membranes is particularly pronounced. This means that the cells are not mainly located in a relatively thin superficial region of the membrane but are present in the complete volume of the loosely woven thick scaffolding fibers (approximately 200 μm). Using filters has made it possible to distinguish them from the collagen fibers within the complete thickness of this top membrane layer, as can be inferred from figure 4.6. It can be concluded from these representations that chondrocytes adhere to the collagen fibers and that they are elongated along them. A typical fluorescence pattern that chondrocytes show is a rhomb-shape with a dark circle in the middle (s. Fig. 4.6 arrows). This circle can be attributed to the cell nucleus, which is non-fluorescent under NIR (2-photon) excitation conditions. This shape often causes imperfect rendering (s. Fig. 4.6 b) of the cells and the spot detection option of Imaris tends to detect two particles in one cell³. Furthermore, figure 4.6 reveals that the cells are distributed rather homogeneously throughout the examined volume, provided that scaffolding collagen fibers are present. In fact, large cell clusters with "stacked" cells have not been detected in fleece membranes, unlike in sponge-like membranes. As it is of great interest for the project partner IBA to perform long term studies on the same collagen membrane in order to achieve a feedback mechanism for the variation of the cell culture conditions, identical membrane regions have been monitored subsequently, usually with a time of 12 to 16 hours. In figure 4.7 two data sets are presented which show identical membrane regions and have been investigated at a time interval of 15 hours. This sample has been kept on

³Other 3D-representation and analysis programs like Volocity by Improvion offer the option of defining classifications for the objects of interest. It would be interesting to see if such a program is more successful in detecting the chondrocytes correctly.

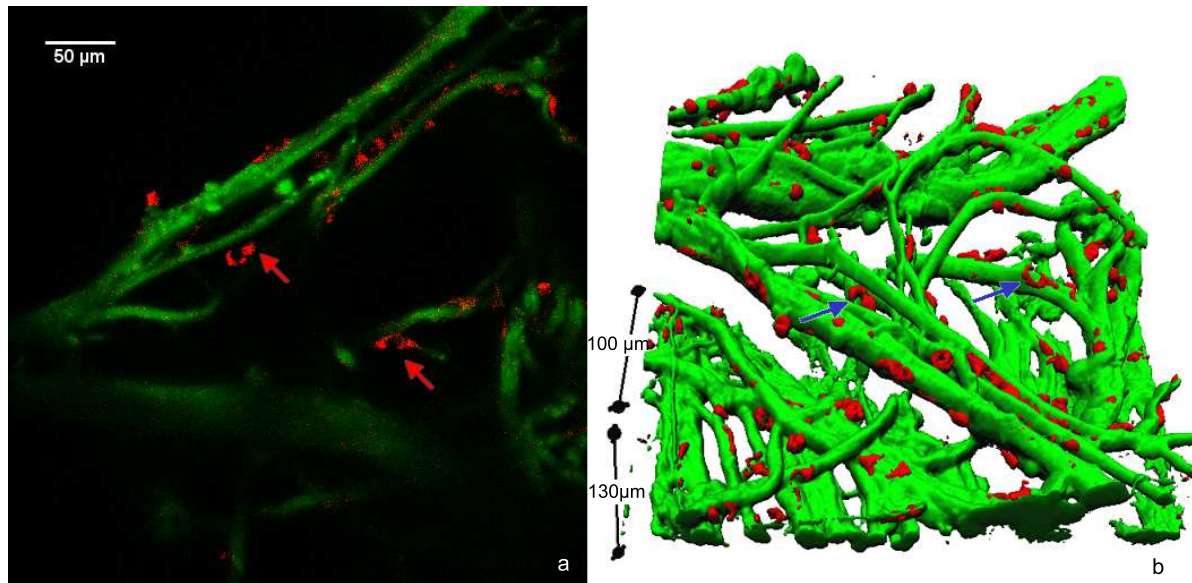


Figure 4.6: 2-photon induced autofluorescence of sponge-like collagen membrane populated with bovine chondrocytes: 790 nm excitation, 320 mW, 64 foci; objective lens: XLUMPLFL; non-descanned camera detection, 465 ms/frame; spectral unmixing result base on emission filter HQ475/50, FF01-525/30, FF01-560/25, HQ575/50, HQ605/55, HQ625/50 and unfiltered; imaging depth down to 170 μm a) optical slice 90 μm inside the sample, green: collagen, red: chondrocytes ; b) rendered data set

the microscope⁴ and therefore the cells did not have appropriate conditions for example, in their required temperature and CO_2 concentration. The sample has however been submerged in cell culture medium. In spite of the insufficient conditions the cells have been kept in only one cell (indicated by arrows) in the complete data set disappeared, meaning it finished its apoptosis cycle (s. Fig 4.7). Other long term examinations (s. section 4.2.3) however suggest that approximately half of the cells die within 12 hours under these inappropriate conditions. This means in reverse, that after the chondrocytes are adhered to the collagen membrane, their position remains relatively stable on the membrane. The migrating dynamic of the cells, especially during the first 24 hours, will be an interesting field of research for the project partner IBA because it should reveal how the cells distribute themselves on the fleece membrane without forming large cell clusters. The examination in figure 4.7 documents, that these examinations should be

⁴This is necessary to find the same sample region again. Thus the bioreactor developed at the project partner IBA is positioned directly on the microscope and cell culture conditions can be maintained and controlled during the examination via 2PLSM.

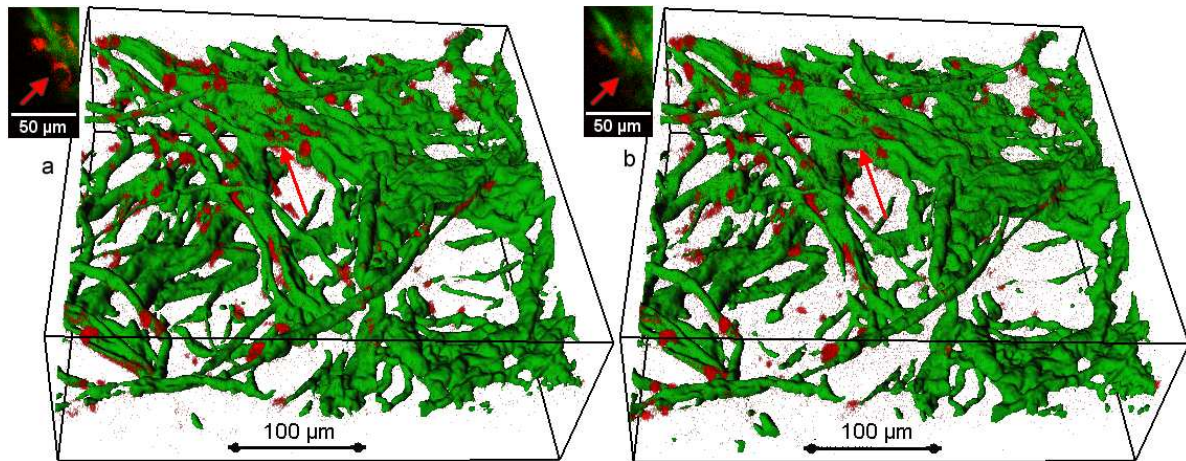


Figure 4.7: 2-photon induced autofluorescence of sponge-like collagen membrane populated with bovine chondrocytes: 790 nm excitation, 320 mW, 64 foci; objective lens: XLUMPLFL; non-descanned camera detection, 465 ms/frame; spectral unmixing result base on emission filter HQ475/50, FF01-525/30, FF01-560/25, HQ575/50, HQ605/55, HQ625/50 and unfiltered; imaging depth down to 154 μm ; insets show ROI of optical slice 36 μm inside the sample green: collagen (rendered), red: chondrocytes (voxel representation) ; a) first data set b) second data set, 15 hours later

possible.

Non-descanned spectral detection

Chondrocyte populated sponge-like collagen membranes have been examined with respect to their fluorescence emission spectra in the range between 475 nm and 675 nm. As described in section 3.3.6 emission spectra are generated for each pixel in the sample. On the basis of these emission spectra, spectral unmixing can then be performed for each pixel. Figure 4.8 A shows the spectral unmixing result for the emission spectra in figure 4.8 D. The emission spectra have been derived from selected regions of interest that could clearly be identified on the basis of their morphology. Region b (s. Fig. 4.8 A) shows a collagen fiber, while regions c and d each contain a chondrocyte. All spectra have been background corrected with a spectrum derived from region a. Dead/alive staining (s. section 3.2) following the autofluorescence measurements revealed that the chondrocyte in region c has to be considered dead, while the one in region d is living (s. Fig. 4.8 B, C). The emission spectra in figure 4.8 D do not exhibit considerable differences for the two chosen chondrocytes. In fact, a thorough comparison of the emission

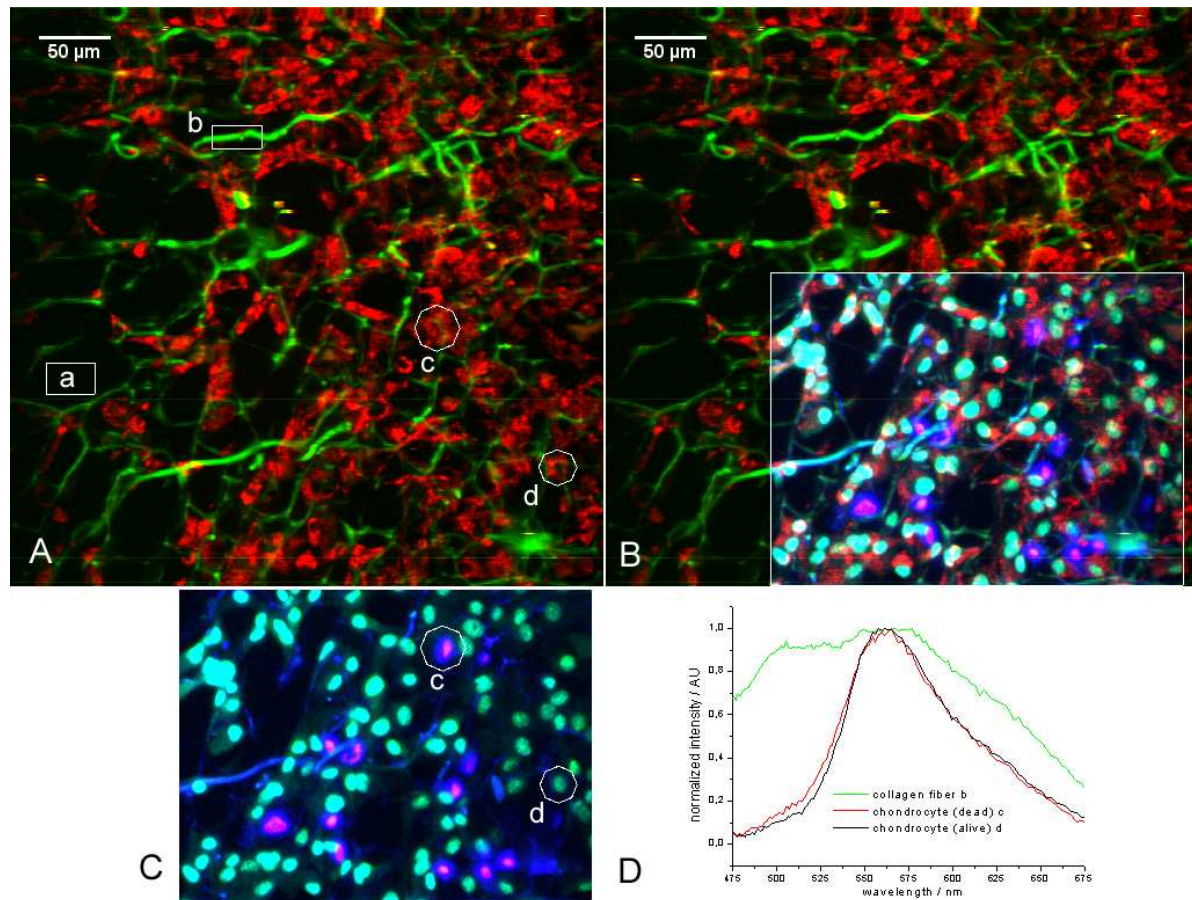


Figure 4.8: 2-photon induced fluorescence of chondrocyte populated sponge-like collagens: A) Cell culture medium without Phenol Red, autofluorescence, 2-photon excitation at 800 nm, 64 foci, 5 mW/focus; 200 ms exposure time per linescan; spectral detection with prism based spectrometer, calibration accuracy $\pm 5\%$, maximum intensity projection of image stack covering a depth of 50 μm , spectral unmixing result on the basis of emission spectra in D, b: collagen, c: dead cell, d: living cell; B) superposition of A and C in the according sample region; C) sample stained with Syto 9 and Propidium Iodide, maximum intensity projection of image stack covering a depth of 50 μm , spectral unmixing result on the basis of emission filter HQ475/50 for collagen, HQ 525/50 for Syto 9 and HQ 625/50 for Propidium Iodide, nuclei of dead cells in red and of living cells in green, collagen in blue ; D) normalized emission spectra of different sample regions indicated in A, spectra are background corrected with spectrum from region a.

spectra of all clearly distinguishable cells in this data set did not indicate any significant differences in the emission spectra of the chondrocytes, whether they have been stained dead or living afterwards. The chondrocytes' emission spectra are hypothesized to be entirely due to Riboflavin⁵. On the basis of the emission spectra, the collagen membrane and the chondrocytes can be clearly distinguished, but no further information on the cells can be based on these. Two aspects of a comparison between stained and unstained fluorescence images are noteworthy. First, while both stains Syto 9 and Propidium Iodide stain the nuclei, the autofluorescence of Riboflavine is located in the cytoplasm of the cells. Therefore, slight shifts in the image of an individual cell may occur when comparing the native fluorescence and the fluorescent probe. Second, in many cases in this data set the staining results suggest the presence of a dead cell, which can not be found in the autofluorescence image. Most likely this is due to cell nuclei or DNA fragments which are remnants of dissolved dead cells.

4.2.3 Cell culture conditions with Phenol Red

SHG on fleece collagen membranes

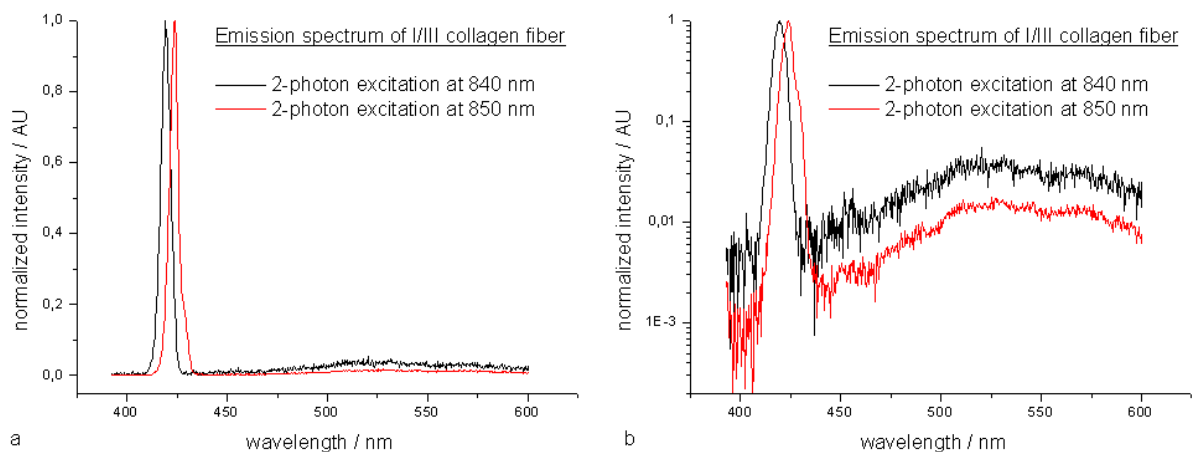


Figure 4.9: Emission characteristics of collagen I/III fiber: Single beam excitation at 840 nm and 850 nm, epi-nondescanned spectral detection with TRIAX 190 spectrograph

Strong SHG signals from thick collagen fibers have been detected in single beam non-descanned epi-detection mode (s. Fig. 4.9). As can be inferred from these spectra the emission peaks at 420 nm and 425 nm, respectively, are indeed due to SHG because

⁵For a comparison of native 2-photon induced emission spectra of cell components see [20].

they are shifted by only 5 nm upon changing the incident exciting laser wavelength from 840 nm to 850 nm. In particular, figure 4.9 b shows that the SHG signal can be more intense than the autofluorescence signal from the fibers. Furthermore, figure 4.9 b indicates that the intensity ratio between SHG and autofluorescence increases with higher wavelength. This is most likely due to reduced 2-photon absorption cross-sections of collagens for higher wavelengths. 2-photon action cross-sections have not been determined in this work, but the excitation wavelength dependency of fluorescence emission intensity has been tested⁶. It was found, that excitation of collagens and chondrocytes is best performed between 790 nm and 800 nm in the existing 2PLSM. When detecting SHG however, wavelengths > 810 nm are preferable because the transmission of the dichroic mirror, the short pass filter and the objective lens drops considerably below 400 nm. As the SHG signal of collagens can be fairly easily spectrally distinguished from the

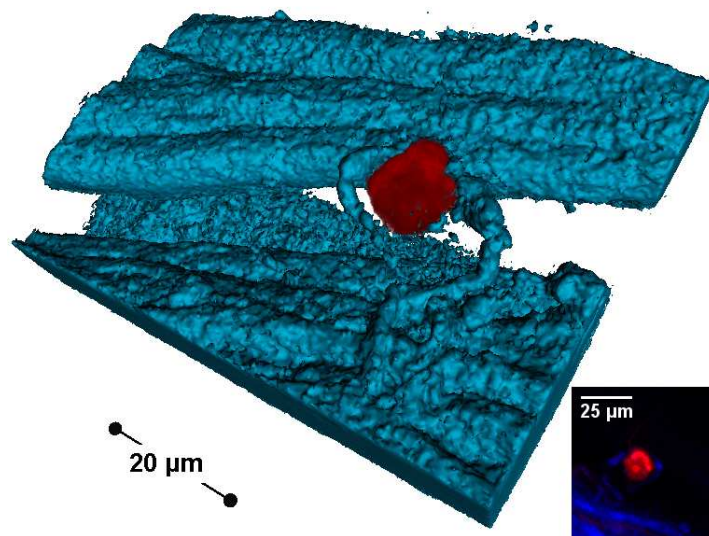


Figure 4.10: Chondrocyte adhered to collagen fiber: Excitation 820 nm, 15 mW; single beam non-descanned PMT detection of native fluorescence and SHG signal; spectral unmixing on the basis of emission filters HQ 525/50, HQ 575/50 and HQ 410/20; collagen fiber in blue, rendered surface; chondrocyte in red, voxel representation, inset shows spectrally unmixed optical plane of the original data set

broad autofluorescence signal of cells (s. section 4.2.1) by filters, providing a functional

⁶This pragmatic approach was chosen, as measurements of 2-photon action cross-sections are difficult. They include measuring the wavelength dependency of laser intensity in the sample, meaning that not only laser power has to be determined but also the laser pulse width. For the purpose of finding out how to most efficiently excite in a given setup, 2-photon action cross-sections are not necessary.

contrast mechanism for collagens and chondrocytes regardless of Phenol Red in the cell culture medium. As can be inferred from figure 4.10, chondrocytes can be distinguished from collagen fibers by using appropriate emission filters and the spectral unmixing algorithm. Only I/III-collagen fibers of fleece membranes exhibited sufficient SHG signals in epi-detection to use the effect for distinguishing cells and collagen. SHG on sponge-like membranes could not be epi-detected with sufficient intensities upon using average laser power up to 15 mW per focus on superficial regions of the membrane. Trans-detection of SHG is not possible because the I/III-collagen membranes currently used in MACI treatments are too thick.

Non-descanned camera detection

By using fluorescence emission filters⁷ it has been possible to distinguish between sponge-like collagen and chondrocytes by spectral unmixing. However, the results have been rather poor. Therefore, it is beneficial to use Phenol Red free cell culture medium in order to achieve more reliable results, when the intention is to gain information about cell morphology.

Descanned single beam spectral detection

In section 3.3.7 the use of a spectrograph in descanned detection mode for a single exciting focus is described. In this mode it has also been possible to distinguish between collagens and chondrocytes which have been cultivated in cell culture medium containing Phenol Red. This can be inferred from figure 4.11. Due to the reduced data volume in the descanned single beam spectral detection mode, 3-D measurements are possible, making this mode especially feasible for fleece collagens. Two aspects of the chondrocyte distribution on the sponge-like collagens are particularly interesting (s. Fig. 4.11 a, b). Firstly, the chondrocyte density considerably drops with sample depth. This means, that on these membranes there is no 3-dimensional chondrocyte distribution as it would be required in a MACI treatment in order to built functional cartilage. Secondly, large clusters of chondrocytes can be seen in figure 4.11 a. Again, these clusters are not desirable in MACI treatments. An increase in pore sizes of the sponge-like membranes is expected to help distribute the chondrocytes more homogeneously throughout the membrane and therefore provide a more functional basis for successful treatments.

⁷HQ475/50, FF01-525/30, FF01-560/25, HQ575/50, HQ605/55, HQ625/50

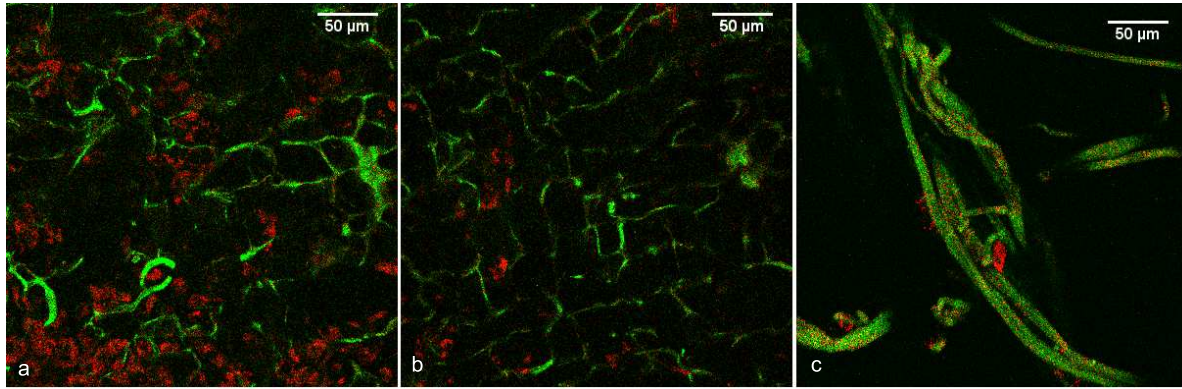


Figure 4.11: 2-photon induced autofluorescence of chondrocyte populated collagen membranes: Single beam excitation, 800 nm, 10 mW; descanned spectral detection with Acton Spectra Pro 2300i spectrograph and 32-fold linear multi anode PMT; spectral unmixing result, green: collagen, red: chondrocyte; a) grouped maximum intensity projection of optical planes 12 μm to 20 μm inside sponge-like collagen membrane b) grouped maximum intensity projection of optical planes 36 μm to 44 μm inside sponge-like collagen membrane c) grouped maximum intensity projection of optical planes 75 μm to 87 μm inside fleece collagen

Non-descanned spectral detection

Chondrocyte populated sponge-like collagen membranes, which had been kept in cell culture medium with Phenol Red, have been examined with 2PLSM in the prism based non-descanned spectral detection mode. Subsequent dead/alive staining (s. section 3.2) of the same sample region has been performed to achieve information on the vital state of the cells and then to compare the vital state with the autofluorescence results. Figure 4.12 shows two maximum intensity projections of those subsequent experiments. Figure 4.12 A is a maximum intensity projection of the spectrally unmixed staining experiment⁸. The data set contains optical planes down to 45 μm in the sample. Cells stained with Propidium Iodide (dead) are represented in this red, while cells that have been stained only with Syto 9 are presented in green. The spectrally unmixed maximum intensity projection of the autofluorescence data set is presented in figure 4.12 B. The basis for spectral unmixing are the emission spectra in figure 4.4 a. In figure 4.12 B the collagen is represented in blue, dead chondrocytes are represented in red and living ones are represented in green. On the basis of a comparison of figure A and B it can

⁸Additionally a maximum intensity projection of a the autofluorescence signal filtered by an HQ 535/50 filter is superimposed in blue in this image. This channel shows the scaffolding collagen and enables to compare positions of chondrocytes in the images.

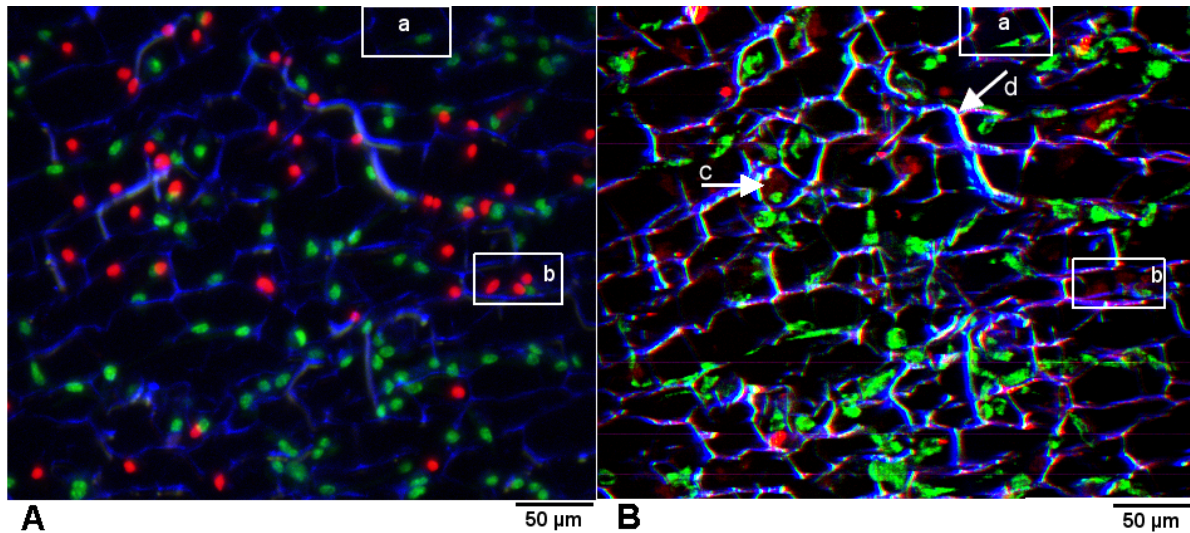


Figure 4.12: Chondrocyte populated sponge-like collagens: Cell culture medium with Phenol Red; A) maximum intensity projection of spectral unmixing result for stained (Syto 9 and Propidium Iodide) sample, red: dead chondrocytes, green: living chondrocyte; blue: scaffolding collagen detected by autofluorescence filter HQ 535/50; B) maximum intensity projection of image stack covering a depth of $45 \mu\text{m}$, spectral unmixing result on the basis of emission spectra in Fig. 4.4 a; 2-photon excitation at 800 nm, 64 foci, 5 mW/focus; 200 ms exposure time per linescan

be concluded that in almost all cases the characterization of cells on the basis of autofluorescence is identical to the characterization in the staining experiment (s. region a with one living cell and region b with three dead cells and one living one). It has to be admitted that the native characterization in many cases is not quite as obvious as one might hope, especially not in printed versions of the image. In general, the living cells are easier to detect as the dead ones. Furthermore, there are certain spots in figure 4.12 A that suggest that a dead cell is present. When comparing these regions with the autofluorescence data set, no cell is visible at all. This means, that in such a region only DNA fragments or the cell nucleus is left. Spot detection with Imaris failed to sufficiently detect dead and living cells in the spectrally unmixed autofluorescence data set. On the other hand, figure 4.12 B provides a good basis of evaluating the ratio of dead to living cells, because when comparing regions of the sample that clearly exhibit a cell, the user can always correctly⁹ determine whether the cell is dead or living. In

⁹This has been tested throughout the complete data set. No cell has been characterized incorrectly on the basis of spectral unmixing.

conclusion, non-descanned spectral detection of chondrocyte populated sponge-like collagen membranes provides reliable information on the viability of individual cells. Fully automated detection algorithms could, however, not yet be developed.

Fluorescence lifetime imaging microscopy

As chondrocytes adhered to collagen membranes start to produce ECM in vitro, the question whether certain ECM components can be characterized on those membranes, arose. Collagen II, a crucial component of the ECM, is of particular interest and it exhibits autofluorescence. Because a characterization of different types of collagens on the basis of fluorescence lifetime has been reported [125], a characterization of the collagen membrane and the newly produced collagen II of the ECM would be desirable. Therefore, to test the general feasibility of FLIM-based contrasts, chondrocyte populated collagen membranes have been imaged using a time gated image amplifier (s. section 3.3.2). Figure 4.13 shows a typical FLIM result. In figure. 4.13 A the complete fluorescence intensity of an optical plane 15 μm inside the membrane clearly exhibits chondrocytes (red arrow, region b) adhered to the bordering collagen scaffolding structure. The fluorescence lifetime image (Fig. 4.13 B), derived by a monoexponential fit to the fluorescence decay of each pixel, revealed that the autofluorescence lifetimes of scaffolding collagen and chondrocytes considerably differ in most regions of this sample. Chondrocytes and collagen exhibit fluorescence lifetimes of about 800 ps and 1300 ps, respectively. While these lifetimes seem to enable a clear characterization, the lifetime image (Fig. 4.13 B) is not as crisp as the decay times suggest. On the left side of the image four chondrocytes are clearly detectable, while the right side appears very dynamic and exhibits overall longer lifetimes and a less clear characterization. This impression is supported by the fluorescence lifetime histogram (Fig. 4.13 C, D). The fluorescence lifetime distribution of the complete imaged region is continuous rather than consisting of two distinct regimes. When comparing the fluorescence lifetime image (Fig. 4.13 B) and its basis, the fluorescence intensity image (Fig. 4.13 A), it becomes evident that the right side of the latter already appears blurred as it is suffering from more scattering of fluorescence in higher sample regions than the left side of the image. In conclusion, the monoexponential fit of fluorescence lifetime decay is in principal capable of characterizing chondrocytes and I/III-collagen membrane. A more in-depth analysis of the fluorescence lifetimes, based on the data set presented in figure 4.13, is documented in figure 4.14. Regions that have been clearly identified as collagen (s. Fig. 4.13 A, region a) and a chondrocyte (s. Fig. 4.13 A, region b) and that exhibit a comparably homogeneous and clearly discriminable

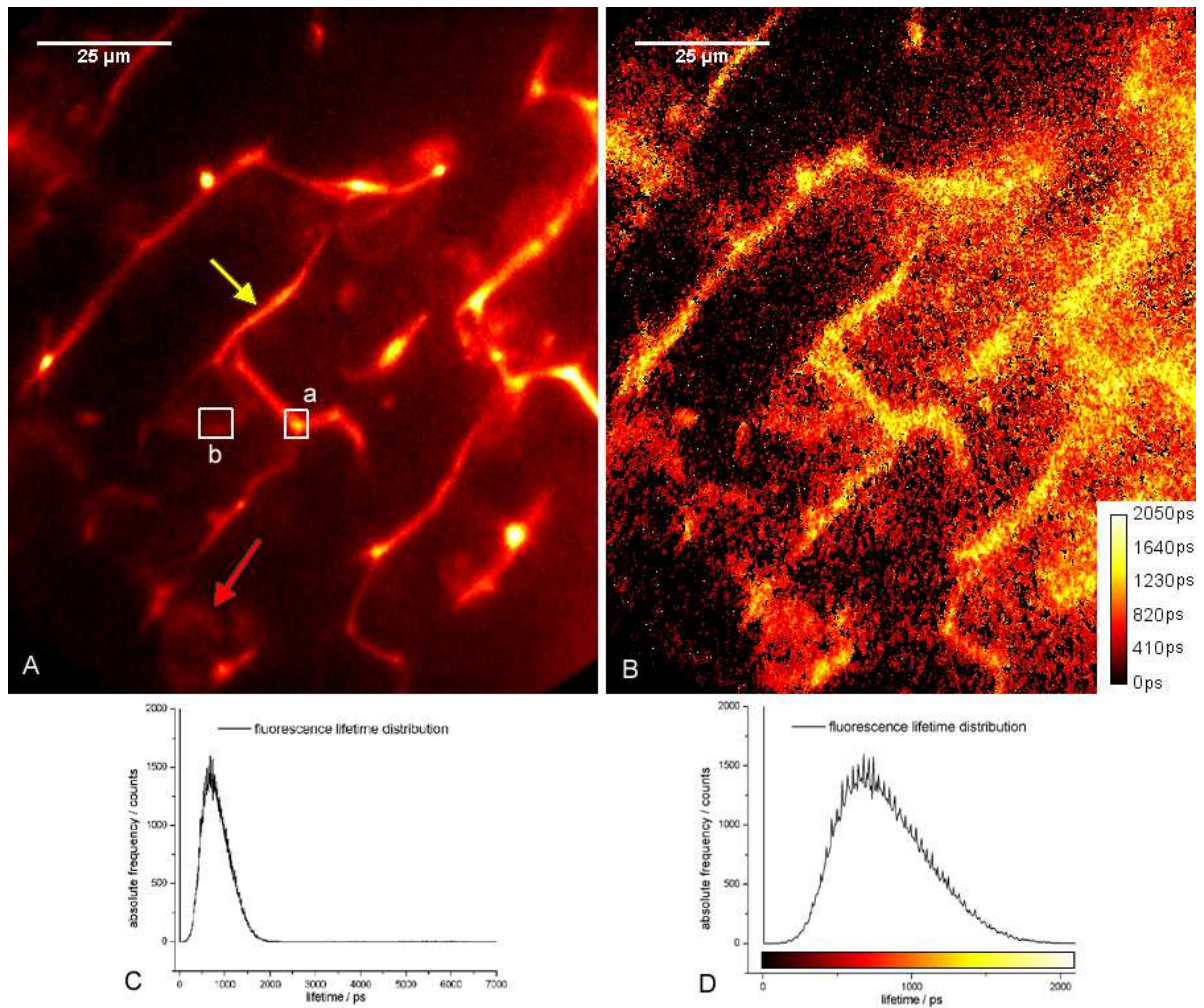


Figure 4.13: 2-photon induced autofluorescence of sponge-like collagen membrane populated with bovine chondrocytes: 785 nm excitation, 320 mW, 64 foci; objective lens: UPLAPO60XW3/IR; non-descanned camera detection with time gated Pico Star, 1000 ms/frame, frame shift 100 ps, frame width 1000 ps, total lifetime 10 ns observed; A) added fluorescence intensity, collagen in region a is basis for fluorescence lifetime measurement in Fig. 4.14 a, yellow arrow indicates collagen fiber, chondrocyte in region b is basis for fluorescence lifetime measurement in Fig. 4.14 b, red arrow indicates chondrocyte; B) monoexponential fluorescence lifetime fit of data set, lifetimes color coded as indicated by calibration bar; C) histogram of monoexponential lifetime distribution covering all calculated lifetimes; D) histogram of monoexponential lifetime distribution covering lifetimes presented in B

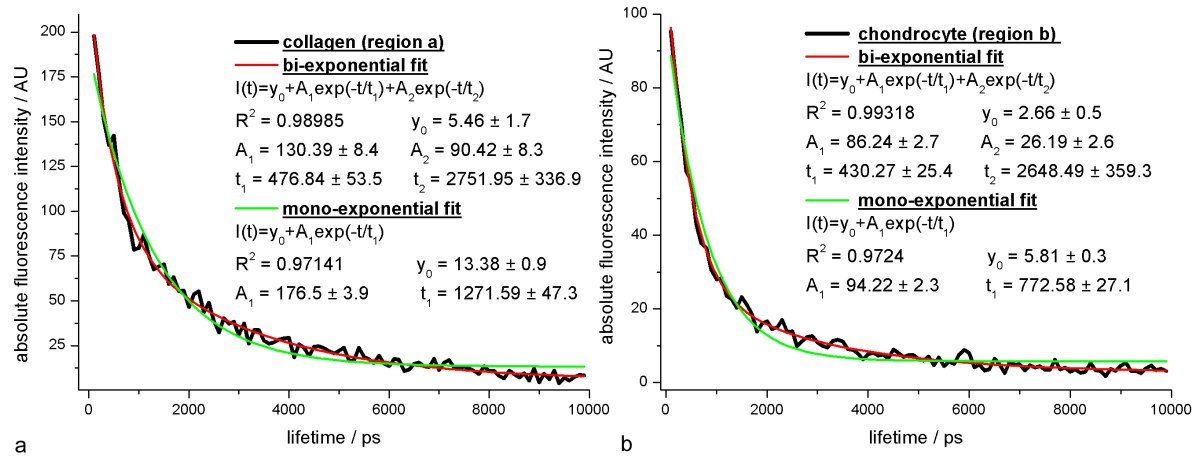


Figure 4.14: Fluorescence lifetime analysis of selected sample regions: a) fluorescence lifetime of collagen derived from Fig. 4.13 A, ROI a; b) fluorescence lifetime of chondrocyte derived from Fig. 4.13 A, ROI b

fluorescence lifetime, have been subject to further investigations¹⁰. Figure 4.14 a and b, clearly show¹¹ that the monoexponential fit, represented in figure 4.13 B, can be improved by a biexponential fit of the fluorescence lifetime data. Interestingly, while the monoexponential fits for both ROIs calculate lifetimes of ≈ 1270 ps for collagen and ≈ 770 ps for the chondrocyte, the biexponential fits for the two regions yielded almost identical time constants, ≈ 450 ps and ≈ 2700 ps respectively. Different relative contributions of both time constants (s. fit data in Fig. 4.14 a, b: A_1/A_2) to the biexponential fit, 1.4 for collagen and 3.3 for the chondrocyte, explain the different monoexponential time constants. Due to software limitations, it has not been possible to fit the complete data set biexponentially for each pixel and evaluate the usefulness of these improved fits yet. Furthermore, as all fluorescence lifetime measurements have been performed under cell culture conditions with Phenol Red, its influence on the measurement should be eliminated in following FLIM measurements.

Considering these preliminary measurements and analysis of chondrocyte populated collagen membranes, FLIM measurements appear to be promising, but their capabilities have to be further evaluated.

¹⁰Other regions in the sample revealed similar results.

¹¹The improved R^2 values and an obviously improved fit for decay times > 7000 ps document this.

4.3 Parallel descanned detection

In this work a new descanned parallel pinhole and photomultiplier detection array for multifocal multiphoton microscopy that effectively reduces the blurring effect of scattered fluorescence photons in strongly scattering biological media has been developed. As described in section 3.3.4, spectrally resolved images are generated by the use of a filterwheel. Figure 4.15 shows the spectrally unmixed autofluorescence image of a Ficus Benjamini leaf 25 μm inside the leaf as an example for the new parallel descanned detection mode. The image nicely reveals for example stomata, a vascular bundle and the red fluorescent chlorophyll.

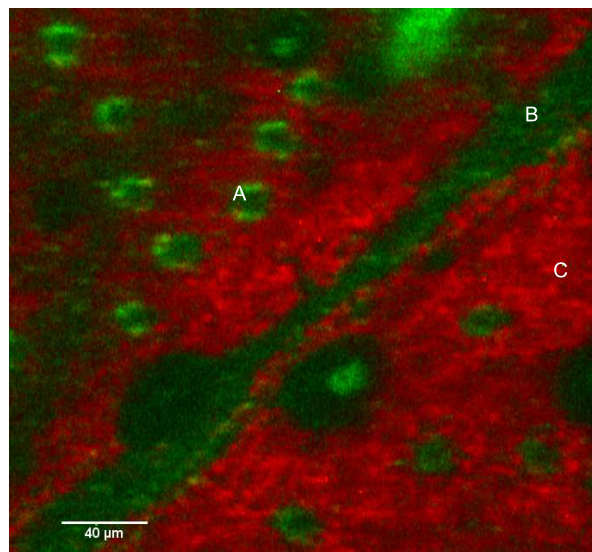


Figure 4.15: Parallel descanned detection of autofluorescence of Ficus Benjamini leaf 25 μm inside the sample in spectral unmixed representation: 800nm excitation, 32 beams (5 mW/focus), emission filters: HQ 525/50, HQ 535/50, HQ 575/50, HQ 625/50, spectral unmixing result, A: stoma, B: vascular bundle, C: granular chloroplasts, chlorophyll in red

4.3.1 Scattering suppression

As explained in section 2.5.2, non-descanned camera detection suffers from image blur in strongly scattering media, because fluorescence light that has been scattered in the sample contributes to image formation on the wrong CCD-pixels. This problem does not occur in single beam PMT detection because images are generated on the basis of the excitation properties of the 2-photon microscope. Scattered NIR photons do not

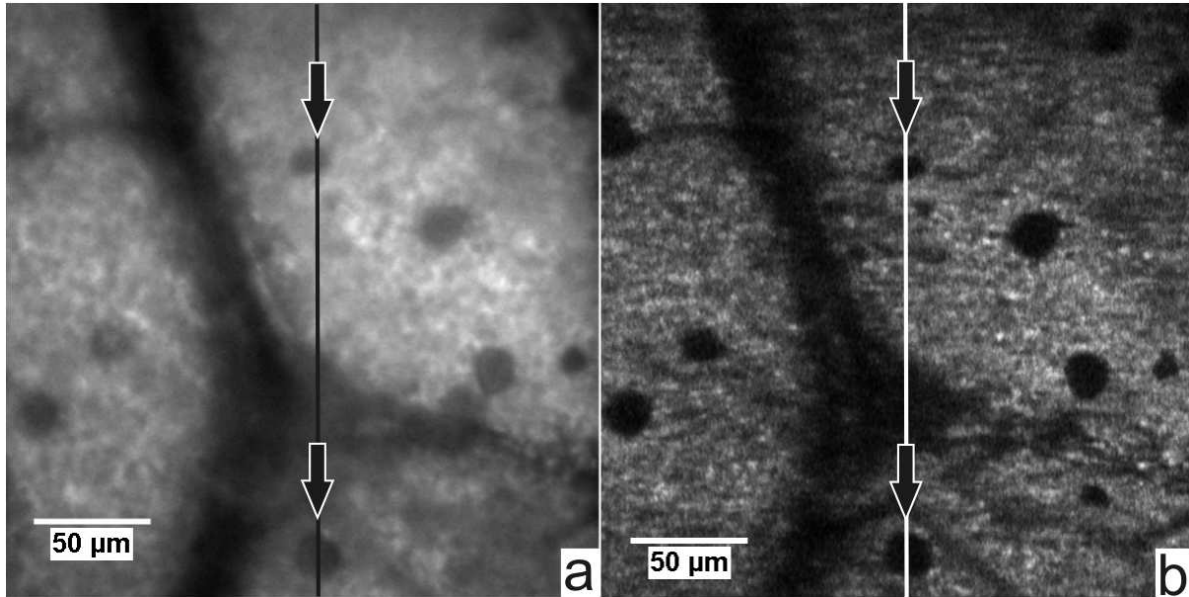


Figure 4.16: Multifocal 2-photon (800nm) excited autofluorescence of *Ficus Benjamini* leaf 45 μm inside the sample in minimum-maximum representation: a) non-descanned camera detection b) 32-fold parallel descanned detection; lines indicate profiles in Fig. 4.17

contribute to fluorescence generation in the excitation path. Scattered 2-photon induced fluorescence light does not contribute to image formation at all if it does not reach the detector, otherwise it does not result in image blur. To overcome the limitation of single focus excitation, a 32-fold descanned pinhole and detector array has been set up (s. section 3.3.4), which is due to the use of pinholes inherently insensitive to scattering of fluorescence, regarding image haze. In parallel descanned detection the depth limitation is the complete loss of the ballistic fluorescence signal and not the increased contribution of scattered fluorescence as in non-descanned camera detection.

A typical example of a blurred parallel non-descanned camera detected image is presented in figure 4.16 a), where a *Ficus Benjamini* autofluorescence image 45 μm inside the leaf is presented. The blur effect described in section 2.5.2 is evident from this image. Once more it has to be stressed that the loss in imaging quality is not due to a lack of detected fluorescence light, it is due to a loss of image contrast. Figure 4.16 b) presents the same sample measured in parallel descanned detection mode, using 0.4 mm diameter detection pinholes. It is obvious that the contrast in this image is considerably improved and therefore more image details are maintained. In order to quantify the gain in contrast, two vertical intensity profiles (Fig. 4.17) have been extracted from both images,

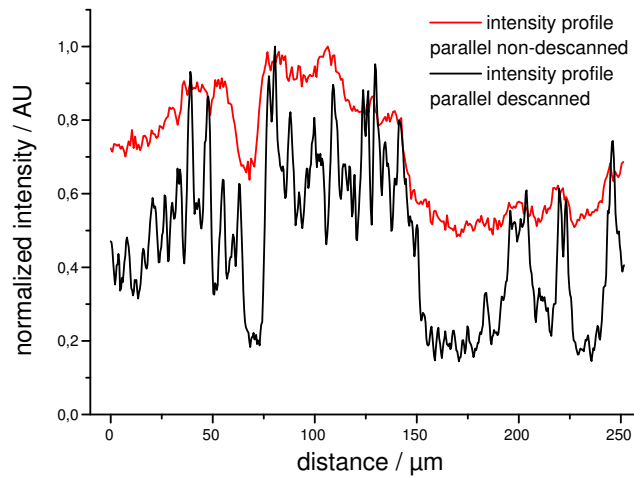


Figure 4.17: Fluorescence intensity profile along vertical lines in 4.16; normalization is based on absolute image maximum

as indicated by the two lines in 4.17. Both profiles have been normalized to compare their dynamics. From the profiles in Fig. 4.17, it is evident that the parallel descanned detection image (Fig. 4.16 b) yields higher dynamics (i.e. granular chloroplasts), a larger absolute minimum-maximum ratio and steeper edge slopes at large, distinct image features (note the two organelles in Fig. 4.16 indicated by arrows and their corresponding fluorescence intensities located at 70 to 75 μm and at 225 to 240 μm in Fig. 3).

4.3.2 Confocal detection

As described in section 2.4, it is possible to reduce the size of the detected PSF in 2PLSM if additional pinholes are introduced in the detection path. This is the case in parallel descanned detection. In order to measure point spread functions, green fluorescent beads (s. section 3.1.3) have been imaged. Special care has been taken to properly adjust the coverslip correction of the UPLAPO60XW3/IR objective lens. The pinhole size was set to 0.4 mm, significantly smaller than the magnified diameter of the airy disk for a 515 nm point source ($= 0.985$ mm), for confocal parallel descanned detection. Typical results of these measurements are presented in Fig. 4.18. Both axial and lateral PSF of the confocal parallel descanned detection clearly show improved FWHM when comparing them to a theoretical 2-photon excitation PSF as well as to an experimental PSF in the non-descanned detection mode. PSF measurement data have been fitted to

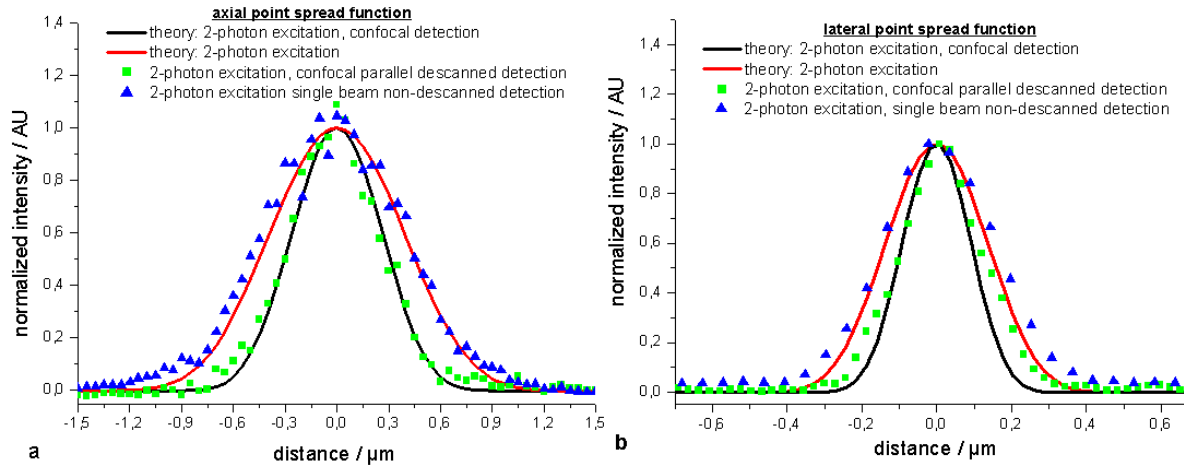


Figure 4.18: Axial (a) and lateral (b) point spread functions, theoretical curves calculated for high aperture objective lens ($\text{NA}=1.2$) from Eq. 2.50, experimental PSF measured with 2-photon excitation (800 nm) of fluorescent beads (emission maximum 515 nm) in water (refractive index $\eta = 1.33$)

a Gauss profile and their FWHM has been calculated from the Gauss fit. The optical resolutions have been calculated for emission wavelength of 515 nm, assuming Gauss profiles and applying the Rayleigh criterion. Results are listed in Tab. 4.1, where it can be inferred that experimental and corresponding theoretical FWHM values match very well. Furthermore, a comparison with the non-descanned PMT detection mode reveals that axial and lateral resolutions in the confocal parallel descanned detection mode are improved by 35% and 21%, respectively. This improvement is due to the use of point-like rather than finite size detectors. The slight broadening of the PSF's experimental values in comparison to the theoretical ones is probably due to overfilling of the back aperture of the objective lens and aberrations in the magnifying optics in the parallel confocal detection case. Additionally, the broadening of lateral PSF in the confocal parallel descanned detection mode is most likely due to imperfect shift vectors for adding up the 32 PMT channels.

Improved resolution has been tested by performing 3-D fluorescence measurements of a fixed pollen sample (s. Fig. 4.19). Especially when examining optical planes close to the massive core body of the pollen¹², improved resolution of the confocal parallel descanned detection became apparent. While the non-descanned detection mode (Fig. 4.19 e) suf-

¹²In 4.19 a spectrally resolved voxel representation shows the fluorescence data set of the pollen lying under the optical plane (in z-direction) that is presented in figure 4.19 d and e.

Detection mode	FWHM	Resolution
Confocal parallel descanned, axial	618 nm ± 25.5 nm	735 nm ± 30.3 nm
Confocal parallel descanned, lateral	266.1 nm ± 17.1 nm	316.4 nm ± 20.4 nm
Single beam non-descanned PMT detection, axial	943.8 nm ± 53.4 nm	1122.2 nm ± 63.5 nm
Single beam non-descanned PMT detection, lateral	337.3 nm ± 33.6 nm	401 nm ± 40 nm
Theoretical 2-photon excitation, axial	887.8 nm	1055.6 nm
Theoretical 2-photon excitation, lateral	313.2 nm	372.4 nm
Theoretical 2-photon excitation, confocal detection, axial	602.6 nm	716.5 nm
Theoretical 2-photon excitation, confocal detection, lateral	211.9 nm	252 nm

Table 4.1: Overview of measured and calculated PSF: 2-photon excitation 800 nm, emission 515 nm, NA=1.2, $\eta = 1.33$, s. Eq. 2.50

fers from significant fluorescent background of the pollen body, confocal parallel descanned detection (Fig. 4.19 d) filters this background out due to its improved z-resolution. This becomes obvious when comparing the two normalized intensity profiles¹³ in Fig. 4.19 b, which have been derived from the fluorescence intensity data presented in Fig. 4.19 d, e. For the confocal parallel descanned detection mode in this measurement fluorescence signal-to-noise and signal-to-background are improved by 200% and up to 350%, respectively.

4.3.3 Detection efficiency

In order to quantify improvements in the photon statistics, fluorescence intensities of Rhodamin 6G (1 mM) dissolved in water in descanned and non-descanned detection mode have been measured upon using the identical detector (H-7422-40) and experimental parameters (laser power etc.). In both measurement modes, detection efficiencies are almost identical when placing the detector in the focal distance of the first imaging lens (s. Fig. 3.2 19), which results in a 360-fold magnification of the exciting focus. This means that descanned detection in our setup does not result in a loss of signal intensity for ballistic photons. When comparing descanned detection between the above mentioned 360-fold magnification and the necessary 1880-fold (627-fold respectively) magnification, a loss in signal intensity of approximately 23% has been measured with the multi anode PMT (H7260-01) for a single beam. This loss is due to aberrations in the magnifying optics that image outside the active detection area (0.8 mm x 8 mm) of the PMT. Further losses in fluorescence intensity occur when the pinhole array is introduced in front of the PMT (e.g. a total loss of a factor of 4 for pinholes with a diameter of 0.8 mm). These losses are dependent on the area of the pinholes, as can be inferred from figure 4.20. At the same time the pinholes are necessary to block out scattered light from the other fluorescent foci. This means that choosing a particular set of pinholes, is a tradeoff between signal intensity and suppression of scattered light. Considering the advantage of the 32-fold generation of fluorescence, parallel descanned detection of ballistic photons with 0.8 mm diameter pinholes has a 4-fold increased photon statistics compared to non-descanned single beam detection with a high quantum yield H-7422-40 PMT. This calculation includes the fact, that the single beam PMT's Q.E. is roughly twice the Q.E. of the multi anode PMT. The efficiency for the two detection methods can easily be compared when assuming that the detected fluorescence intensity $I_{sb} = I_s + I_b$ for non-descanned single beam detection is composed of all scattered I_s and ballistic

¹³The intensity profiles have been measured along the indicated lines in Fig. 4.19 c, d and e.

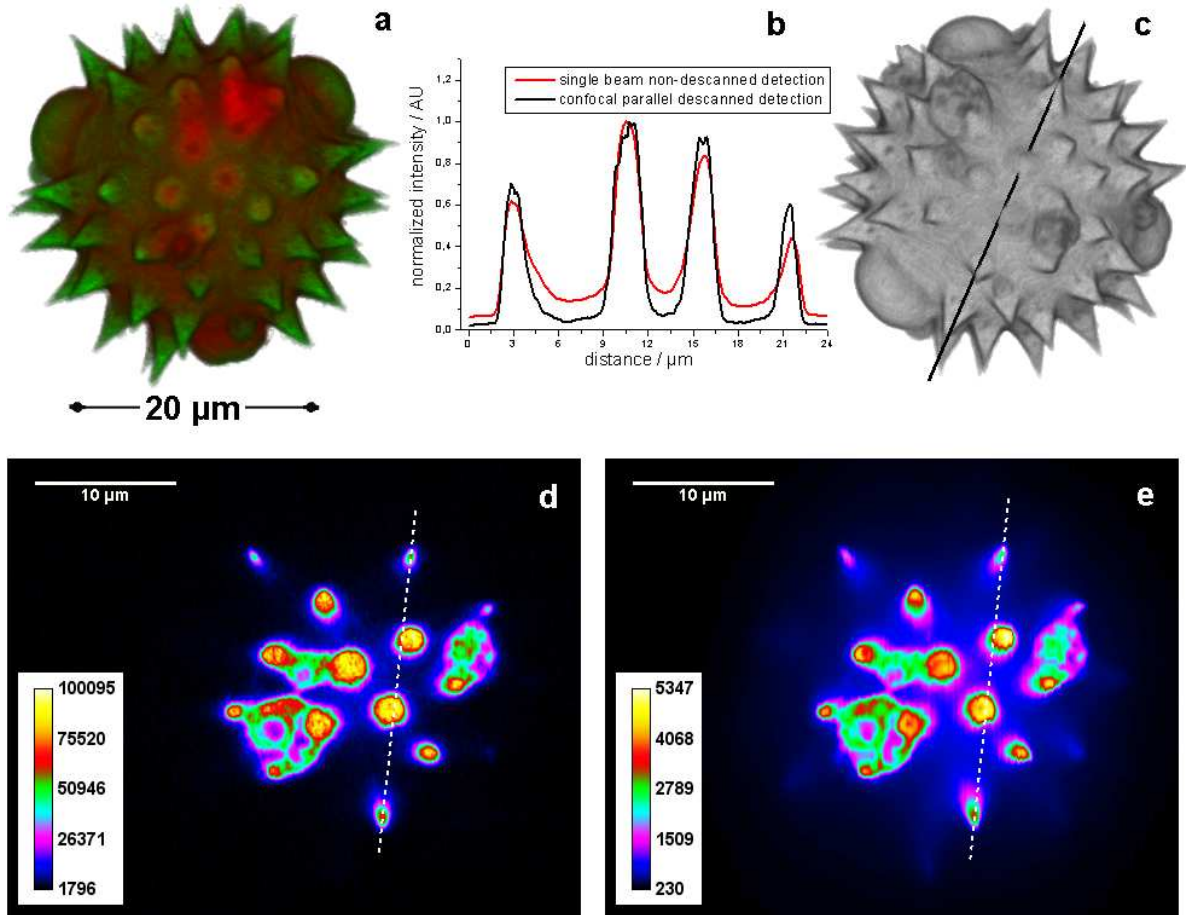


Figure 4.19: 2-photon (800 nm) excited fluorescence of pollen: a) spectrally resolved voxel representation of optical planes lying under optical the plane presented in d and e, emission filters HQ525/50 and HQ575/50 in green, emission filter HQ625/50 in red, confocal parallel descanned detection; b) normalized intensity profile along indicated lines in c, d and e; c) intensity voxel representation of the complete data set, no filter, confocal parallel descanned detection; d and e are located $1.5 \mu\text{m}$ above the massive central pollen body, spikes of pollen are penetrating the optical plane, dashed lines indicate profile in b, minimum-maximum representation; d) confocal parallel descanned detection; e) single beam non-descanned detection

I_b fluorescence light, while the detected fluorescence intensity I_{pd} for parallel descanned beam detection was measured to be $I_{pd} = 4 \cdot I_b$. Hence parallel descanned detection provides better photon statistics than non-descanned single beam detection as long as the ratio of scattered to ballistic photons remains smaller than a factor of three (s. Eq. 2.54). Because of the higher Q.E. of the single beam detector and the losses due to the pinholes for parallel descanned detection, single beam non-descanned detection is more

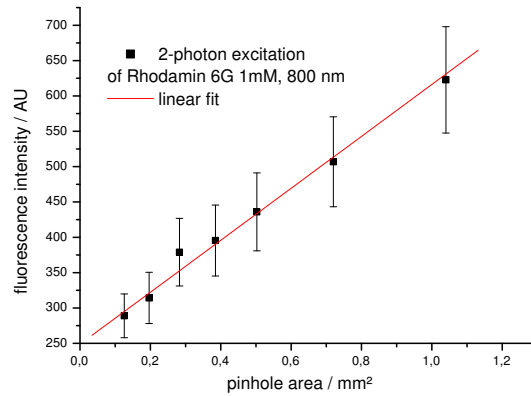


Figure 4.20: Measurement of detection efficiency dependence on pinhole area: 2-photon induced fluorescence intensity of 1 mM Rhodamin 6G, 800 nm, 600 V PMT (H7260-01) anode voltage, error bars represent standard deviation of measurements

appropriate for weak fluorescence applications, when the signal-to-noise ratio becomes the limiting factor of the measurement. Additionally, this detection method is relatively insensitive to scattered fluorescence so that especially low fluorescence detection in scattering samples is performed best by non-descanned single beam detection.

In conclusion, parallel descanned detection is best suited for samples with a relatively high fluorescence level, so that blocking of scattered fluorescence from deep imaging planes does not result in a complete loss of signal and the high Q.E. of the single beam PMT is not required. For such applications, the developed parallel descanned detection has advantages over both single beam non-descanned detection, because of improved photon statistics, and multi-beam non-descanned camera detection, because of drastically reduced scattering haze. Furthermore parallel descanned detection often¹⁴ provides an improved resolution compared to the other 2PLSM imaging modes.

4.3.4 Multifocal multispectral descanned detection

In section 3.3.8 the basic idea of simultaneously imaging spectral properties of eight fluorescent foci is presented. In short, this measurement mode enables a simultaneous detection of eight sections of the fluorophores' emission spectrum. In this measurement mode the spectral detection properties can be tuned to a certain extent by adjusting

¹⁴For example in the typical case of imaging a GFP (emission maximum 508 nm) expressing cell imaged with the UPLAPO60XW3/IR objective lens and a set of 0.8 mm pinholes.

the position of the 8x8 multianode PMT. Therefore, it offers great flexibility for imaging samples with emission characteristics that require emission filters which are not at hand. Furthermore, due to simultaneous spectral detection, this imaging mode should be rather fast when imaging several different fluorophores. Pixel dwell times are, however, currently limited by the sampling rate of the AD-conversion board so that, for an 8-fold spectrum of 8 exciting foci, only 45,000 pixels/s can be scanned. Special care has

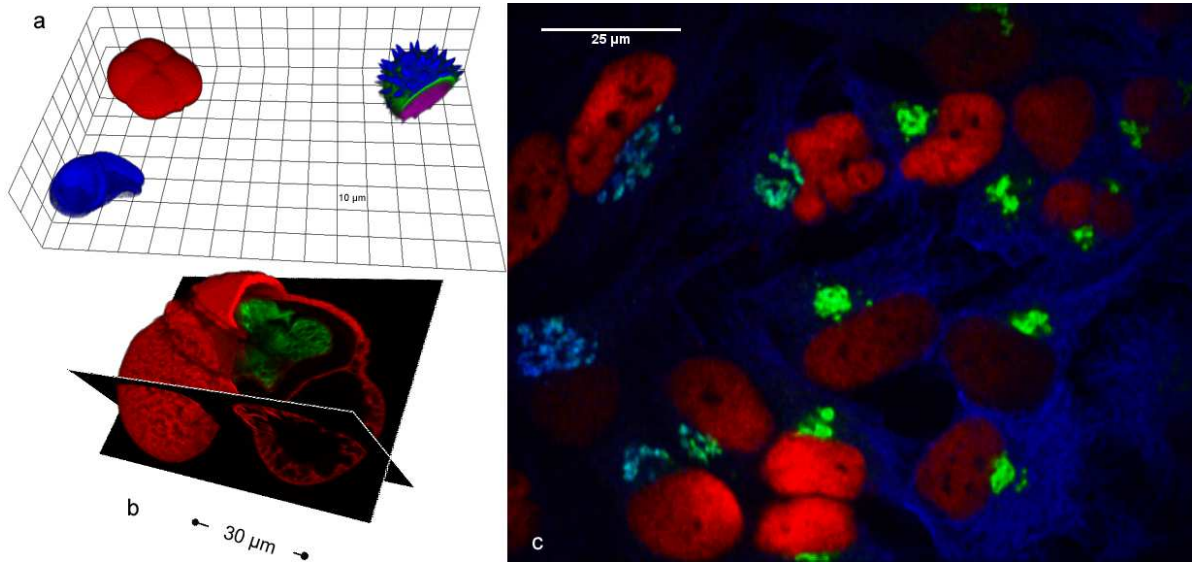


Figure 4.21: Multifocal multispectral 2-photon induced fluorescence detection: excitation at 800 nm, 8 foci, 2 mW/focus, UPLAPO60XW3/IR, all data sets generated with minimal pixel dwell time possible, slit width: 0.5 mm, spectral detection range: ≈ 530 nm to ≈ 640 nm; a) three pollen imaged simultaneously, voxel representation, spectral unmixing based on four different spectral emission characteristics, upper right pollen has been digitally "cut" open to show its inside with its own emission characteristic, gridlines represent $10 \mu\text{m}$, acquisition time: 6.2 s for each optical plane; b) individual pollen, voxel representation, spectral unmixing based on two different spectral emission characteristics, pollen digitally "cut" open to show its inside with its own emission characteristic, acquisition time: 4.4 s for each optical plane; c) spectral unmixing result of HeLa-cells functionally stained with different quantum dots (from Quantum Dot Corp.), cell nuclei (red): 655 nm, golgi apparatus (green): 585 nm, microtubules (blue): 525 nm, acquisition time: 6.2 s

been taken to align the exciting foci in a straight line so that the detected spectral range in a particular PMT-row is identical for all eight foci. This is however not necessary. Through a controlled relative shift of the exciting foci, different spectral ranges can be detected by different foci. This has to be accounted for in the subsequent superposition

of the images. In the presented measurements the detected spectrum ranged between ≈ 530 nm and ≈ 640 nm¹⁵ so that each row of PMT segments detected a spectral range of ≈ 11 nm. These values have been estimated by filtering fluorescence light of Rhodamin 6G and correlating the filter cut-off wavelengths with the PMT-rows they have been imaged on. As the used filters have rather broad emission characteristics, the spectral data have to be considered an estimation rather than a calibration. However, on the basis of this detection mode, it has been possible to functionally differentiate between up to four different fluorescence characteristics by using spectral unmixing. The presented data sets have been acquired in 6.2 s (Fig. 4.21 a, c) and 4.4 s (Fig. 4.21 b) for each optical plane, generating, after data processing, eight spectrally resolved images of the same sample region. Figure 4.21 represents the first test of this imaging mode. Further, in depth analysis of the imaging properties, i.e. resolution and sensitivity towards scattered light, have to be performed. Even more important, the spectral characteristics of the system have to be evaluated and optimized. A spectral detection range wider than 110 nm, as has been used in the presented measurements, is desirable. Whether an extension of the spectral range to about 300 nm¹⁶ can be realized by shifting the prism position in the optical path, possibly by positioning the prism between the two tube lenses, has to be tested. Optionally, a different type of prism or transmission gratings could be implemented in the setup. However, these first imaging tests justify an evaluation and optimization of this imaging mode because its theoretical potential for simultaneous and therefore rapid imaging of different fluorophores in combination with a tunable spectral detection range makes it attractive from the practical point of view.

4.4 Intracellular protein dynamics using Pa-GFP

Three different cases of Pa-GFP activation and fluorescence decay measurements in cell nuclei have been performed to quantify protein dynamics in transfected tobacco BY-2 protoplasts. The diffusion of Pa-GFP proteins and the active translocation of Pa-GFP-tagged LCL1 proteins out of the cell nucleus has been measured and the localization of the export-negative mutant Pa-GFP-LCL(NESm) has been verified. Three time constants have been determined in these measurements. They can be attributed to a short term greening effect of DsRed [106], induced by a 3-photon photoconversion,

¹⁵This spectral range was originally meant to enable a spectral discrimination of collagen and chondrocytes.

¹⁶This value seems reasonable because every row of the PMT would detect ≈ 35 nm, sufficient for discriminating most dyes.

to the translocation and diffusion time constants and to photobleaching of Pa-GFP. As all three time constants considerably differ from another, they are easily distinguishable, although in some cases two time constants have been relevant in one individual measurement.

4.4.1 Pa-GFP diffusion from the nucleus into the cytoplasm

A typical selection of five images from a complete series of 1P-transmission-fluorescence images is presented in figure 4.22. The images have been consecutively taken at the start of recording before photo-activation (0 s), at the start of photo-activation (26 s), and at 33 s, 180 s and 1000 s after the start of fluorescence recording. The cell nucleus is indicated by a red ellipse that has been selected as the ROI for the temporal analysis of the fluorescence intensity. The decrease of fluorescence intensity in the nucleus over time, as can be inferred from figure 4.22 c, d and e, is accompanied by an increase in fluorescence intensity in the cytoplasm of the cell. This documents the diffusion of Pa-GFP from the nucleus into the cytoplasm and can be determined by the decrease in fluorescence intensity in the nucleus. The rectangular shape of the strong fluorescence signal at time point 26 s displays the $7 \mu\text{m} \times 8 \mu\text{m}$ activation area of Pa-GFP, accomplished by scanning four laser foci for 3 seconds within the nucleus. The fluorescence intensity of Pa-GFP

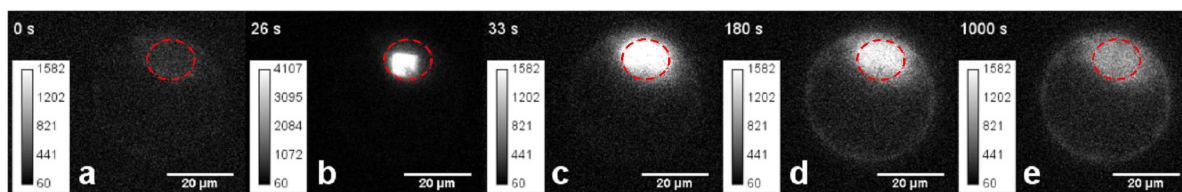


Figure 4.22: Pa-GFP diffusion into the cell: five selected 1P-transmission fluorescence images of a tobacco BY-2 protoplast expressing Pa-GFP, activation at 800 nm for 3 seconds covering an area of $7 \mu\text{m} \times 8 \mu\text{m}$ with 4 parallel laser foci, 10 mW per focus; a) before activation; b) during 2P-activation of Pa-GFP; c-e) after 2P-activation, taken at the times indicated

within the chosen ROI (red ellipse in Fig. 4.22) over the whole time series is presented in figure 4.23. The 1P-fluorescence intensity curve is dominated by a sharp peak at 26-29 s after the start of recording, indicating the photo activation of Pa-GFP by the 3 s laser scanning cycle with 800 nm wavelength¹⁷. Following Pa-GFP activation, approximately 30 s after the start of recording, the averaged fluorescence intensity has increased by a

¹⁷The 800 nm laser intensity does not only activate Pa-GFP but also induces fluorescence.

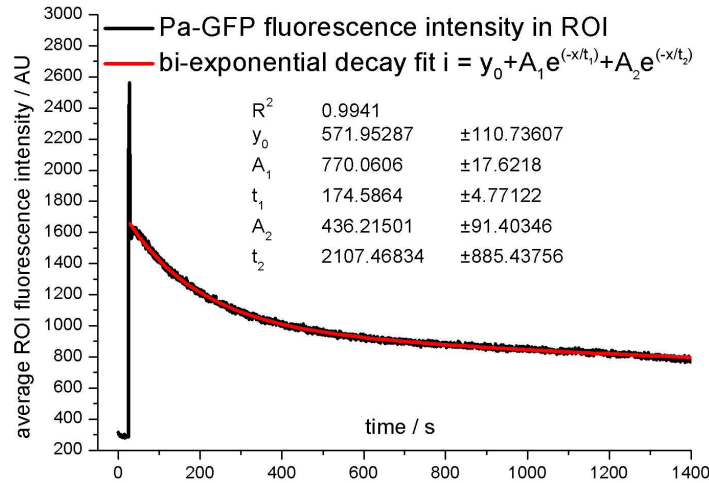


Figure 4.23: Quantitative analysis of Pa-GFP diffusion from the nucleus into the cytoplasm: Before activation the averaged 1P-fluorescence intensity in the nucleus (ROI) is low (averaged intensity ≈ 300). Between 26 s and 29 s a fluorescence burst is induced by 800 nm fs-laser activation. Directly after activation, the averaged fluorescence intensity is increased by a factor of 5 compared to the pre-activation intensity, followed by a decrease of fluorescence in the ROI. The monitored decrease of fluorescence intensity in the cell nucleus is mainly due to diffusion of the activated Pa-GFP into the cytoplasm. Photobleaching becomes noticeable for long examination durations. Bi-exponential fitting describes the overall decrease of fluorescence in very good approximation (red line). A diffusion time constant of 175 s was calculated for this experiment.

factor of about 5, as compared to the pre-activation intensity. Afterwards, the decrease of nuclear fluorescence intensity in time, which is due to the diffusion of activated Pa-GFP fluorophores out of the nucleus into the cytoplasm (compare Fig. 4.22 c, d), has been recorded. Photobleaching becomes noticeable afterwards, as can be deduced from the over all reduction in fluorescence intensity in the entire cell (s. Fig. 4.22 d, e). This interpretation is supported by the fact that the decrease of nuclear fluorescence over time can not be properly fitted by a single exponential decay function. In contrast, bi-exponential fitting describes the observed intensity decrease in good approximation (s. Fig. 4.23, red line). With this fit, time constants for the two processes after Pa-GFP photo-activation in the nucleus have been calculated, resulting in 175 s for Pa-GFP diffusion and in 2100 s for photobleaching (s. Fig. 4.23) in this measurement. In order to determine the equilibrium 3-dimensional distribution of proteins within a BY-2 protoplast, the DsRed and Pa-GFP fluorescence has been imaged by 2PLSM before and after Pa-GFP activation.

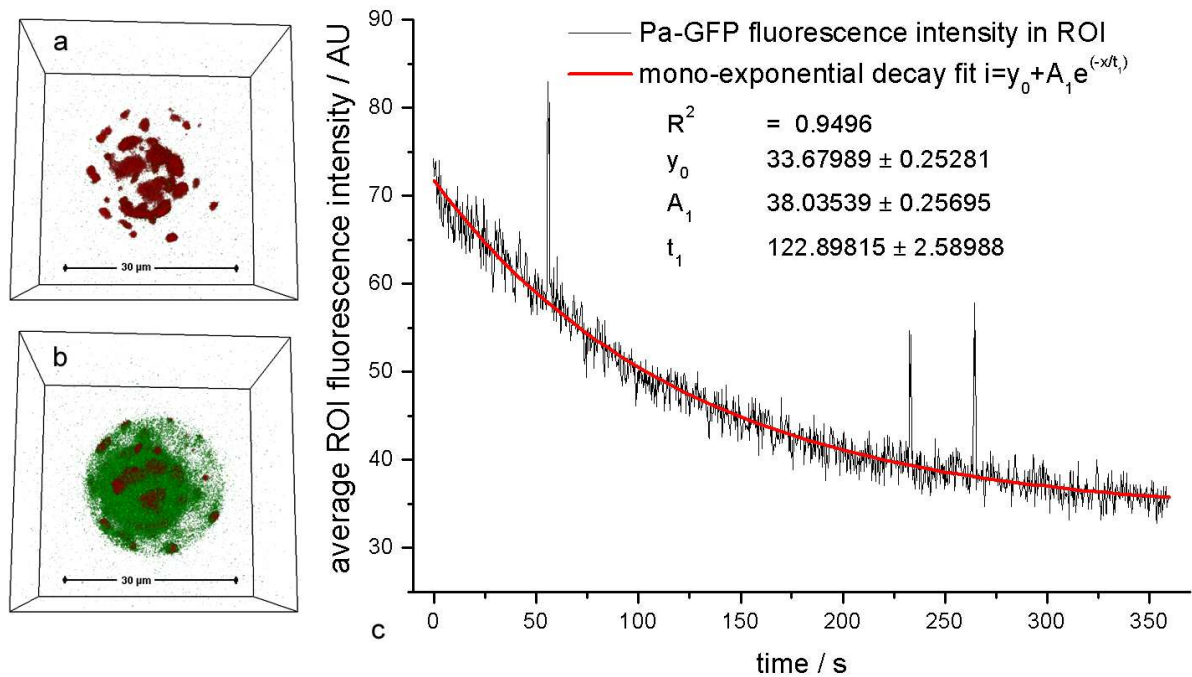


Figure 4.24: Quantitative analysis of diffusional Pa-GFP dynamics and 3D equilibrium monitoring of At2g38360-DsRed and Pa-GFP-LCL1 before and after photo-activation in the nucleus of a tobacco BY-2 protoplast: Voxel representation of equilibrium distribution of DsRed (red) and Pa-GFP (green), 2PLSM measurement in parallel non-descanned camera detection, 64 foci, 920 nm, 240 mW, filter HQ 510/20 for Pa-GFP and HQ 625/50 for DsRed; a) before activation; b) after activation of Pa-GFP in the nucleus and fluorescence decay measurement; c) quantitative analysis of the post-activation fluorescence decrease of Pa-GFP in the nucleus (black), measured by 2-photon induced fluorescence at 920 nm in parallel non-descanned detection, mono-exponential fit (red), a time constant of 123 s was calculated for the nuclear fluorescence decrease of Pa-GFP due to diffusion

Imaging at 920 nm excitation wavelength has been performed in parallel non-descanned camera detection, using appropriate emission filters (HQ 510/20 for Pa-GFP and HQ 625/50 for DsRed). The fluorescence voxel representations are shown in figure 4.24 a, b, where DsRed and Pa-GFP are displayed in red and green, respectively. Whereas the transfected protoplast only exhibits the red fluorescence of the transfection marker At2g38360-DsRed (s. Fig. 4.24 a) before photo-activation, Pa-GFP, that had been exclusively activated in the nucleus, clearly diffused into the cytoplasm (s. Fig. 4.24 b). This distribution from the nucleus has been measured 400 s after Pa-GFP activation, while its corresponding decrease has been detected over 350 s by 2P-epifluorescence induced

by the second Ti:Sa laser tuned to 920 nm. Due to the above mentioned intrinsic time gap of five seconds for re-setting the measurement, the activation cycle is not present in figure 4.24 c. The nuclear fluorescence decay within the first 350 s is presented together with a mono-exponential decay fit, confirming the interpretation that photobleaching is relevant only in long term (> 10 min) measurements. The analysis yielded a diffusion time constant of 123 s for this experiment, in agreement with the diffusion time constant presented in the similar experiment described above.

The distribution of Pa-GFP within the protoplast, after localized 2P-activation in the nucleus, is solely due to diffusion. For Pa-GFP only fluorescence intensity decay data that could be mono- or bi-exponentially fitted with $R^2 > 0.94$ have been included in the calculation of the average time constant for diffusional translocation. Eight cells met biological and statistical criteria, revealing an average diffusion time constant of $125.06 \text{ s} \pm 33.15 \text{ s}$, while standard deviation of individual fits remained below 5.26 s. This result compares very well with a diffusional decay time constant of 200 s as published by Chen et al. [112].

4.4.2 Active translocation of the MYB transcription factor LCL1 fused to Pa-GFP

The measurement and analysis protocols for active translocation due to facilitated nuclear import versus nuclear export are identical to Pa-GFP diffusion measurements through the nuclear pore complexes. Protoplasts co-transfected with At2g38360-DsRed and Pa-GFP-LCL1 have been 2-photon-activated in the nucleus and their decrease in nuclear fluorescence intensity has been monitored with 1P-fluorescence microscopy (s. Fig. 4.25 a, b). Bi-exponential decay fitting of the nuclear fluorescence intensity decay (s. Fig. 4.25 b, red curve) has allowed for a quantitative analysis of these data, calculating two time constants of 4.7 s and 20.6 s, respectively. While the first time constant can be attributed to non-linear short term photoconversional "greening" of DsRed¹⁸, the time constant of 20.6 s reflects the net translocalization of Pa-GFP-LCL1 from the nucleus

¹⁸The effect of three-photon greening, i.e. a shift of DsRed peak emission wavelengths from 590 nm to 495 nm, has been described in [106]. This article states that under certain conditions, for example excitation wavelengths < 760 nm, the greening effect is rather stable. Under 800 nm excitation/activation conditions in the Pa-GFP measurements it has been measured in this work that greening of DsRed does occur, but that it is not stable. On the contrary, it decreases with rapid time constants between 2.6 s and 5 s. In particular this has been measured not only in living protoplasts but also on clearly identifiable DsRed fragments, where no translocalization of Pa-GFP could have occurred.

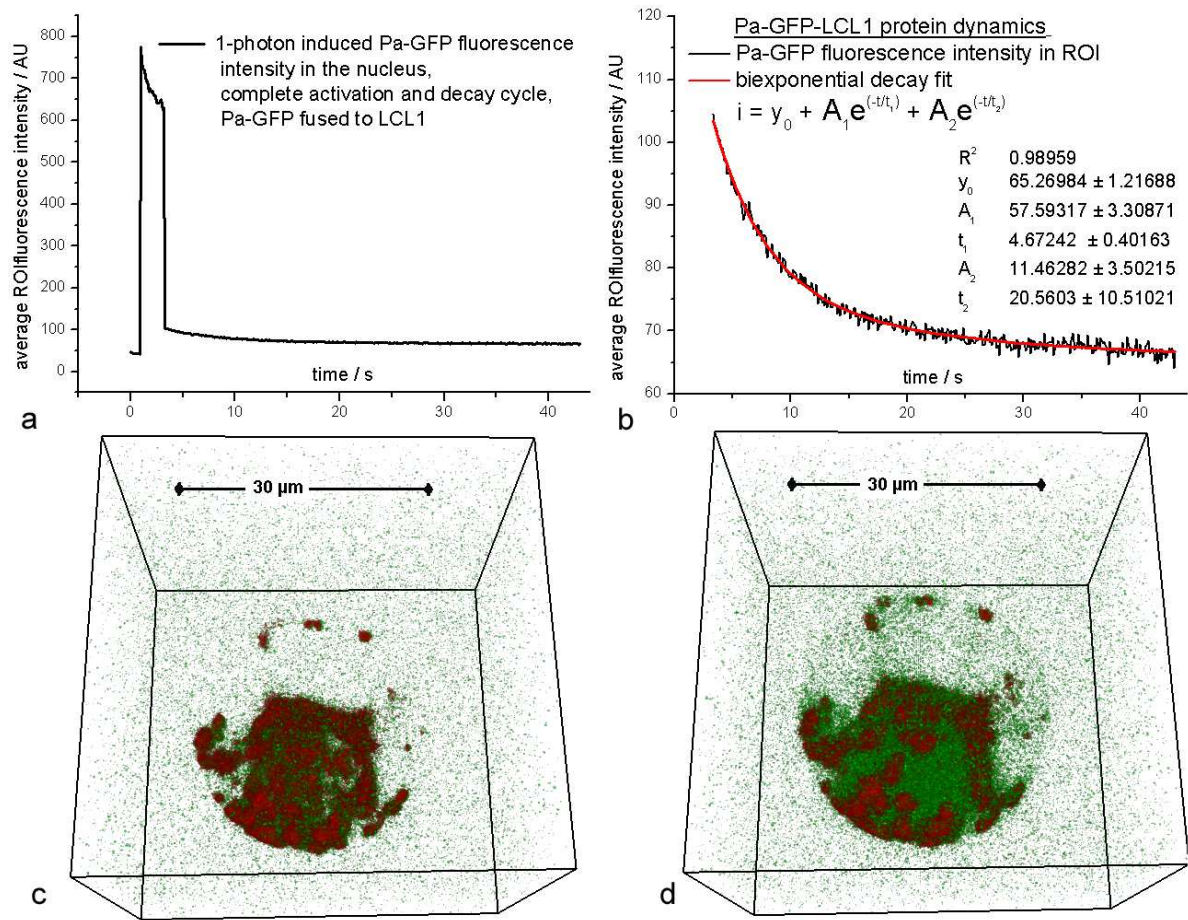


Figure 4.25: Quantitative analysis of actively translocated Pa-GFP-LCL1 dynamics and 3D equilibrium distribution of At2g38360-DsRed and Pa-GFP-LCL1 before and after photo-activation in the nucleus of a tobacco BY-2 protoplast: a) 1P-fluorescence of Pa-GFP in the nucleus including 2P-activation of Pa-GFP at 800 nm for 2.2 s; b) quantitative analysis of the post-activation fluorescence decrease of Pa-GFP in the nucleus (black), bi-exponential fit (red), a time constant of 20.6 s was calculated for the nuclear fluorescence decrease of Pa-GFP-LCL1 due to active transport; voxel representation of equilibrium distribution of DsRed (red) and Pa-GFP (green), 2PLSM measurement in parallel non-descanned camera detection, 64 foci, 920 nm, 240 mW, filter HQ 510/20 for Pa-GFP and HQ 625/50 for DsRed; c) before activation; d) after activation of Pa-GFP in the nucleus and fluorescence decay measurement

into the cytoplasm that finally results in the equilibrium localization observed for GFP-LCL1 represented in figure 4.25 d. This time constant is considerably smaller than the one of diffusional Pa-GFP translocation (compare section 4.4.1). This demonstrates, that active translocation of Pa-GFP facilitated by LCL1 does indeed result in a more rapid turnover of proteins from the nucleus into the cytoplasm. The fact that protein export from the nucleus into the cytoplasm is the reason for fluorescence decay in the nucleus is further supported by the 2PLSM 3D voxel representation of DsRed and Pa-GFP. The corresponding data sets have been measured just before activation of Pa-GFP (s. Fig. 4.25 c) in the nucleus and after monitoring of the fluorescence dynamics, 45 s after starting the complete measurement cycle (s. Fig. 4.25 5d). These two steady state representations of the fluorescence intensity clearly show increased intensity of activated Pa-GFP in the cytoplasm, which means that the Pa-GFP-LCL1 fusion protein has distributed from the nucleus throughout the entire cell.

For the statistical analysis of Pa-GFP-LCL1 fusion proteins, only fluorescence decay data have been used which could be fitted with $R^2 > 0.95$ to mono- or bi-exponential decays. Seven cells met biological and statistical criteria to be taken into account for determining the average time constant for facilitated nucleo-cytoplasmic partitioning of Pa-GFP-LCL1 after photo-activation in the nucleus. The average value has been calculated to be $50.97 \text{ s} \pm 38.5 \text{ s}$, while each standard deviation of individual fits remained below 10.6 s.

4.4.3 Protein dynamics of the export-negative mutant Pa-GFP-LCL(NESm)

An export-negative mutant of LCL1 has been fused to Pa-GFP and its dynamics after 2P-activation in the nucleus has been quantitatively analyzed. In figure 4.26 a typical experiment is presented with a protoplast expressing At2g38360-DsRed and Pa-GFP-LCL1(NESm) including 2P-activation of Pa-GFP in the nucleus and quantitative analysis of protein dynamics by a 1P-fluorescence intensity measurement. After the activation, the average activated fluorescence intensity in the ROI remains almost constant for 300 s. The marginal decrease of nuclear fluorescence intensity has to be attributed to photobleaching of Pa-GFP. Therefore, no exponential fit could be applied to the post-activation intensity data, since suppositional nuclear fluorescence decrease time constants would have been considerably larger than the duration of the experiment. Facilitated translocation or diffusion of the activated Pa-GFP-LCL1(NESm) from the nucleus into the cytoplasm was not observed. This is also supported by the corresponding 2PLSM 3D vo-

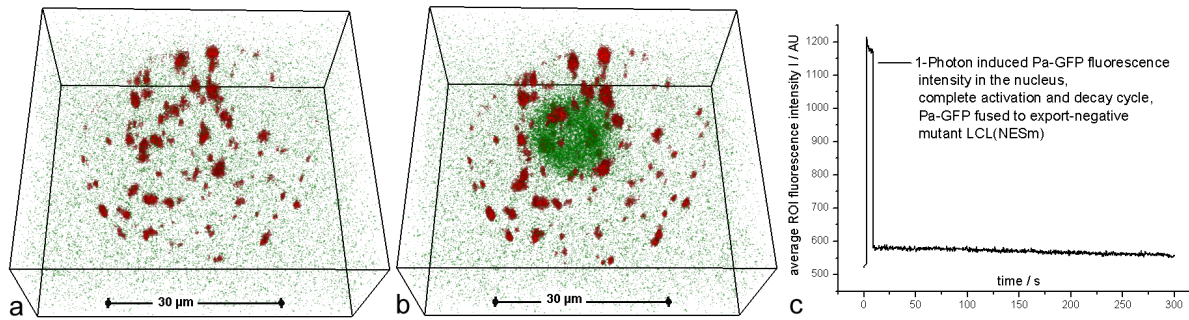


Figure 4.26: Quantitative analysis of the nuclear export-negative mutant Pa-GFP-LCL1(NESm) and 3D equilibrium monitoring of At2g38360-DsRed and Pa-GFP-LCL1(NESm) before and after photo-activation in the nucleus of a tobacco BY-2 protoplast: Voxel representation of equilibrium distribution of DsRed (red) and Pa-GFP (green), 2PLSM measurement in parallel non-descanned camera detection, 64 foci, 920 nm, 240 mW, filter HQ 510/20 for Pa-GFP and HQ 625/50 for DsRed; a) before activation; b) 300 s after activation of Pa-GFP in the nucleus and fluorescence decay measurement; c) quantitative analysis of 1P-fluorescence of Pa-GFP in the nucleus including 2P-activation of Pa-GFP at 800 nm for 6 s, after 2P-activation nuclear fluorescence intensity decreases extremely slowly indicating, the nuclear localization of Pa-GFP-LCL1(NESm)

oxel representation (s. Fig.4.26 a, b) before and after monitoring the nuclear fluorescence decay over time. They clearly show that Pa-GFP has been activated in the nucleus where it remains over the 6 minute course of the experiment. Diffusional translocation is compensated for by active nuclear import, resulting in an exclusively nuclear Pa-GFP-LCL1(NESm) localization.

For none of the examined Pa-GFP-LCL1(NESm) fusion protein expressing cells could fluorescence decay in the nucleus be measured, that had to be attributed to translocation. Only long term photobleaching or occasional short term DsRed greening occurred in these measurements. 2PLSM images before and after photoactivation always revealed a nuclear Pa-GFP localization. In conclusion the LCL1(NESm) mutant of the LCL1 transcription factor has indeed lost the active translocation activity out of the nucleus and is therefore trapped within it.

5 Conclusion and Outlook

In this work a rather broad range of functional biological imaging and the development of new detection techniques has been presented. The following discussion will summarize the central results and point out the next steps for further investigation. At first however, some suggestions regarding the improvement of the 2PLSM by equipping it with the latest technological developments and useful additional features shall be mentioned: In order to improve reproducibility and scanning speed, the mechanical focus drive should be extended with a piezo focus drive. New generations of dichroic mirrors (HC 735 LP, BrightLine, Semrock) and emission short pass filters (FF01-750/SP-25 BrightLine, Semrock) would considerably improve ($\approx 20\%$) the fluorescence transmission in the non-descanned detection modes. Finally, 64-bit computer technology with the capability of addressing more than 4 GB RAM should be used for data acquisition as soon as this technology is available, because at this point (spectrally resolved) fluorescence data sets often can not be measured with the desired depth resolution.

Cartilage

Chondrocytes and ECM in native bovine and human cartilage have been differentiated by their spectral properties. Characteristic differences in arthrotic and non-arthrotic cartilage have been identified on the basis of 2PLSM and chondrocyte densities in the examined cartilage have been calculated by an automated procedure. Therefore, fundamental properties of the cartilage can be investigated by a contact-free, label-free, non-destructive and sterile¹ manner. Complete 3-dimensionally resolved emission spectra of cartilage have not yet been generated, but they would help to identify the relevant fluorophores in the chondrocytes and the ECM. Due to the fact that native cartilage can be imaged relatively easily by 2PLSM, it is promising to plan high sample throughput measurements in order to achieve statistically founded information regarding sensitivity

¹The advantage of sterile measurements is that it enables a pre-examination of bovine cartilage before the extraction of chondrocytes for the population of scaffolding collagen membranes, the findings of which can then be correlated with the quality of the tissue engineering product afterwards.

and specificity of automated chondrocyte detection. Furthermore, reproducible criteria for the characterization of arthrotic and non-arthrotic cartilage should be tested and defined. Both fields require a close collaboration with veterinarians or orthopedic specialists in order to compare the 2PLSM results with classical medical analyses of identical samples.

Chondrocyte populated collagen membranes

Chondrocytes and I/III-collagen membranes can be distinguished from each other on the basis of 2-photon induced fluorescence or SHG light. Imaging depths in these strongly light scattering materials are sufficient to 3-dimensionally represent the chondrocyte distribution on the scaffolding collagens. Furthermore the feasibility of long term investigations and a functional characterization of living and dead cells has been proven while keeping average the power per focus at 5 mW. The influence of Phenol Red in the cell culture medium on the emission characteristics of the chondrocytes could be explained phenomenologically. However, the details of quenching and the broadening of the emission characteristics of Riboflavin in the cells remain unclear. Therefore further measurements to reveal more information on Phenol Red in the cell culture medium need to be performed. Fluorescence emission spectra of cells that have been proliferated in cell culture medium containing Phenol Red need to be compared to emission spectra of cells that have been grown in cell culture medium without Phenol Red. Both types of chondrocytes need to be examined while they are submerged in medium with and without Phenol Red. This change of medium is the crucial and difficult part of the measurement. As identical sample regions should be examined, this type of measurement should be performed in a bioreactor that is coupled to the 2PLSM, such as at the project partner IBA. By doing so, the medium can be replaced while a particular sample region remains in the field of view of the 2PLSM. The same series of four comparative measurements should also be performed using the fluorescence lifetime contrast. As the project partner IBA has the ability to perform both types of measurements, the newly developed non-descanned prism based spectral measurement mode and a time correlated single photon counting measurement mode, these measurements should be unproblematic with their 2PLSM.

Aside from the interpretation of the influence of Phenol Red on the emission spectra, scaffolding collagens and chondrocytes can be differentiated from each other on the basis of their spectral autofluorescence emission properties by using Phenol Red-free cell culture conditions and emission filters. Especially in order to reveal cell migration

and the influence of mechanical stimulation on the cells, this method is advisable. A differentiation between individual dead and living cells will not be possible with these measurements, but as cell viability under proper cell culture conditions is $\approx 96\%$ and most dead cells are not visible by autofluorescence, imageable cells can be considered living in a first approximation. Therefore, detected cell densities will contain the required feedback mechanism for cell culture conditions when 2PLSM-imaging is performed without Phenol Red.

Prism based non-descanned spectral detection

The newly developed prism based, non-descanned spectral detection mode has evolved into a standard measurement method to generate 3-dimensionally resolved autofluorescence emission spectra. The wavelength calibration accuracy for the measurements presented in this text is $\pm 5\%$. This is due to lack of a sufficient calibration method at the time the measurements were taken. Calibration has been performed by using cut-off wavelengths of emission filters. A better calibration method has only just recently been developed. When imaging a micro-fabricated slit and illuminating this slit with defined wavelengths, calibration accuracy can be significantly improved to under $\pm\%$. However, this measurement mode is capable of detecting complete emission spectra and their relative differences depending on the fluorophores present in the examined ROI. Due to the simple setup, and therefore low losses in the optical path, spectrally resolved measurements, even of weakly fluorescing fluorophores like chondrocytes, can be performed with acceptable excitation intensities and pixel dwell times. Furthermore, this measurement mode can be set up within a few minutes which is beneficial for time-critical measurements on living biological samples. Altogether, this measurement mode is a pragmatic way to learn more about the emission characteristics of the sample under investigation. Therefore, it has also been implemented into the project partner's (IBA) 2PLSM.

Evaluation of the acquired data sets is performed by choosing small ROIs in the images and displaying the spectral emission characteristics in these ROIs. For regions that show clear morphological differences, the emission characteristics can be compared in this way. As the last step in this analysis, spectral unmixing is performed on the basis of clearly distinguishable emission spectra. Thus, a spectral unmixing result represents a color-coded compression of a few hundred megabytes of fluorescence emission data. Some of the spectrally unmixed images presented in this text are not as distinct as one might hope for, but when examining the emission spectra of interesting sample regions, the interpretation of this region is usually distinct. In conclusion, the prism based spectral

detection mode offers (almost) uncompromised optical throughput and is therefore ideal for weak native fluorescence yield, as exhibited by chondrocytes.

Descanned detection

Three different descanned detection modes have been implemented in the existing 2PLSM. All of them use multianode PMT detectors. Therefore, improvements in the amplification electronics, the AD-conversion board and the data acquisition software would be beneficial for all these measurement modes.

Regarding descanned single beam spectral detection, it can be concluded that this measurement mode fulfilled its theoretical advantages in practice. These include the broad spectral detection range, acceptable data volume and image acquisition speed, the abandonment of sample scanning and, last but not least suppression of scattered light. Although this measurement mode would benefit from improved amplification electronics (s. below), it can be considered fully functional and useful.

As the improved photon statistics in multifocal multiphoton microscopy are usually used to reduce image acquisition time, this advantage can not be realized in most cases in the present descanned measurements, because the multiplexed 3 MHz sampling rate of the AD-conversion board, translating into approximately 90 kHz for 32 detection channels and 45 kHz for 64 detection channels, is considerably smaller than the 10 MHz camera sampling rate. Only for certain small ROIs (s. explanation in section 3.3.4) are parallel descanned measurements faster than non-descanned camera detection, as the current software does not allow for other suitable scan patterns which could decrease the frame time for freely selectable ROIs. Image generation with these imaging patterns additionally suffers from "stitching" artifacts in the image. This means, that due to different light amplification characteristics of each PMT channel, caused by different PMT-segment QEs, varying amplifier characteristics and imperfect optical alignment of individual detection beamlets, neighboring images generated by linescans of two neighboring foci exhibit different fluorescence intensities. Images that are composed of linescans of different foci therefore presently consist of 8 (in multifocal multispectral imaging) or 32 (in parallel descanned detection) visible image stripes. These considerations could be interpreted as suggesting that the implementation of multifocal descanned detection was not successful. This is not the case. Both measurement modes, multifocal multispectral and parallel descanned detection, were meant to test the general feasibility of parallelized descanned detection and both modes did prove their functionality. While parallel descanned detection was extensively tested, revealing an improved reso-

lution and an efficient suppression of scattered fluorescence, further evaluation of the multifocal multispectral detection mode is still required. However, the first results that have been generated in this imaging mode are very promising because up to four different spectral emission characteristics could be detected simultaneously. At this point of detector development it is necessary to improve the detection electronics and the data acquisition software. Regarding the detection electronics there seem to be two possibilities for advancement. The first option consists of a complete change in the data acquisition concept. The PMT photon signals could be processed by digital counter electronics (including fast amplifiers, matching Schmitt trigger and digital counters for each channel) which transfer photon count rates digitally to the computer. With this detection concept, electronic noise should be minimal, the electronic detection efficiency for all channels should be identical and therefore the sensitivity should be improved. The other option for an improvement in the detection electronics could be an automated calibration tool for the integrating electronics (s. section 3.6). By replacing potentiometer R6 in figure 3.8 with a digital potentiometer (for example DS1267-10) the detection electronics could be automatically calibrated for each alignment of fluorescence foci. Both options require software alterations which would benefit from further software improvements. Image alignment and superposition should be implemented in the image acquisition software, resulting in reduced data volume and real time image generation. For multifocal multispectral descanned detection image acquisition, time and data volume could be reduced by selecting only interesting spectral ranges (rows on the PMT) that are being sampled. For both measurement modes, image acquisition time could be accelerated by allowing different scan patterns. Finally, the magnification optics in descanned detection could be optimized by custom-made lens combinations.

However, all of these suggested improvements seem to fall into the field of activity of the project partner LaVision BioTec because they are development rather than research problems.

In summary, the efforts in descanned detection provided effective suppression of scattered fluorescence light in the sample, improved photon statistics for ballistic photons, simultaneous spectrally resolved image generation without sample scanning and improved resolution.

Intracellular protein dynamics using Pa-GFP

Intracellular protein dynamics, diffusion and active transport have been investigated in a tobacco model system. Different time constants for the different mechanisms of pro-

tein translocation out of the cell nucleus have been determined. Furthermore, the shift in equilibrium localization of the export negative mutant of the protein LCL1 to the cell nucleus has been verified. The results document the strength of selective protein highlighting as it allows for quantitative dynamics measurements. However, due to low the transfection success ($< 1\%$) of the protoplasts, the statistical basis for the calculation of time constants remained rather small. Therefore, stable cell lines expressing Pa-GFP have been grown. Now diffusion of Pa-GFP, localization to the cell nucleus of LCL1(NESm) and active transport of LCL1 and LCL2 can be investigated in vivo. First tests in *Arabidopsis thaliana* roots revealed that 2-photon Pa-GFP activation works efficiently and reliable in vivo. Nevertheless, these measurements will be challenging because cell nuclei are rather small ($\approx 3\ \mu\text{m}$ diameter) and difficult to detect. Thus, Pa-GFP activation within them might require a NIR coated 100-fold magnification objective lens. With the stable cell lines at hand, nuclear import measurements are also possible. When activating Pa-GFP in the cytoplasm exclusively, in this case 1-photon activation at 400 nm may be advisable, the fluorescence accumulation in the nucleus due to diffusion and active import should be measurable.

As the results of selective 2-photon Pa-GFP activation for protein dynamic measurements have been successful, they may trigger further research activities in the field of protein dynamics. Multifocal multiphoton microscopes offer three key characteristics in this field: Video rate image acquisition with sufficient image contrast, high resolution and 3-dimensionally localized labeling volumes. Whether Pa-GFP activation or highlighting techniques for different fluorophores, e.g. greening of DsRed, photoswitching of CFP etc., are used, has to be decided on the basis of the biological system under investigation.

Bibliography

- [1] LAKOWICZ, J. R. (Editor): *Principles of Fluorescence Spectroscopy*. Kluwer Academic / Plenum Publishers, New York, 2nd Edition, 1999.
- [2] DENK, W and K SVOBODA: *Photon Upmanship: Why Multiphoton Imaging Is More than a Gimmick*. *Neuron*, 18:351–357, 3-1-1997.
- [3] DIASPRO, ALBERTO (Editor): *Confocal and Two-Photon Microscopy: Foundations, Applications, and Advances*. Wiley-Liss, Inc., New York, 1st Edition, 2002.
- [4] NAKAMURA, O.: *Fundamental of two-photon microscopy*. *Microsc.Res.Tech.*, 47(3):165–171, 1-11-1999.
- [5] ESPOSITO, A., F. FEDERICI, C. USAI, F. CANNONE, G. CHIRICO, M. COLLINI and A. DIASPRO: *Notes on theory and experimental conditions behind two-photon excitation microscopy*. *Microsc.Res.Tech.*, 63(1):12–17, 1-1-2004.
- [6] HAKEN, H.: *Licht und Materie*. Bibliographisches Institut AG, Zürich, 1st Edition, 1979.
- [7] BOYD, R. W.: *Nonlinear Optics*. ACADEMIC PRESS, INC, San Diego, 1st Edition, 1992.
- [8] KAISER, W. and C. G. B. GARRETT: *TWO-PHOTON EXCITATION IN Ca:F₂:Eu²⁺*. *Phys.Rev.Lett.*, 7(6):229–231, 15-9-1961.
- [9] HARPER, P. G., WHERRETT B. S. (Editor): *Nonlinear Optics*. Academic Press Inc. Ltd., London, 1st Edition, 1977.
- [10] WILLIAMS, REBECCA M., WARREN R. ZIPFEL and W. W. WEBB: *Interpreting Second-Harmonic Generation Images of Collagen I Fibrils*. *Biophys.J.*, 88:1377–1386, 2005.

-
- [11] MOREAUX, L., O. SANDRE and J. MERTZ: *Membrane imaging by second-harmonic generation microscopy*. Journal of the Optical Society of America B (Optical Physics), 17(10):1685–1694, 2000.
- [12] BORN, M. and E. WOLF: *Principles of Optics*. Pergamon Press, Oxford, 6th Edition, 1986.
- [13] SHEN, Y. R.: *The Principles of Nonlinear Optics*. John Wiley & Sons, Inc., New York.
- [14] FRANKEN, P. A., A. E. HILL, C. W. PETERS and G. WEINREICH: *GENERATION OF OPTICAL HARMONICS*. Phys.Rev.Lett., 7(4):118–119, 15-8-1961.
- [15] FINE, S. and W. P. HANSEN: *Optical Second Harmonic Generation in Biological Systems*. APPLIED OPTICS, 10(10):2350–2353, 1971.
- [16] CAMPAGNOLA, P. J., H. A. CLARK, W. A. MOHLER, A. LEWIS and L. M. LOEW: *Second-harmonic imaging microscopy of living cells*. J.Biomed.Opt., 6(3):277–286, 2001.
- [17] MOREAUX, L., O. SANDRE, S. CHARPAK, M. BLANCHARD-DESCE and J. MERTZ: *Coherent scattering in multi-harmonic light microscopy*. Biophys.J., 80(3):1568–1574, 2001.
- [18] CAMPAGNOLA, P. J., M. D. WEI, A. LEWIS and L. M. LOEW: *High-resolution nonlinear optical imaging of live cells by second harmonic generation*. Biophys.J., 77(6):3341–3349, 1999.
- [19] MERTZ, J. and L. MOREAUX: *Second-harmonic generation by focused excitation of inhomogeneously distributed scatterers*. Optics Communications, 196(1-6):325–330, 1-9-2001.
- [20] ZIPFEL, WARREN R., REBECCA M. WILLIAMS, RICHARD CHRISTIE, ALEXANDER YU NIKITIN, BRADLEY T. HYMAN and W. W. WEBB: *Live tissue intrinsic emission microscopy using multiphoton-excited native fluorescence and second harmonic generation*. Proc Natl Acad Sci U S A, 100(12):7075–7080, 10-6-2003.
- [21] STOLLER, P., K. M. REISER, P. M. CELLIERS and A. M. RUBENCHIK: *Polarization-modulated second harmonic generation in collagen*. Biophys.J., 82(6):3330–3342, 2002.

- [22] CAMPAGNOLA, P. J., A. C. MILLARD, M. TERASAKI, P. E. HOPPE, C. J. MALONE and W. A. MOHLER: *Three-dimensional high-resolution second-harmonic generation imaging of endogenous structural proteins in biological tissues*. *Bio-phys.J.*, 82(1 Pt 1):493–508, 2002.
- [23] GU, M.: *Principles of Three-Dimensional Imaging in Confocal Microscopes*. World Scientific Publishing Co Pte Ltd, Singapore, 1st Edition, 1996.
- [24] RICHARDS, B. and E. WOLF: *Electromagnetic Diffraction in Optical Systems .2. Structure of the Image Field in An Aplanatic System*. *Proceedings of the Royal Society of London Series A-Mathematical and Physical Sciences*, 253(1274):358–379, 1959.
- [25] SHEPPARD, J. R.: *An electromagnetic theory of imaging in fluorescence microscopy, and imaging in polarization fluorescence microscopy*. *Bioimaging*, 5(4):205–218, 1997.
- [26] HIGDON, P. D., P. TOROK and T. WILSON: *Imaging properties of high aperture multiphoton fluorescence scanning optical microscopes*. *Journal of Microscopy-Oxford*, 193:127–141, 1999.
- [27] SHEPPARD, C. J. R. and H. J. MATTHEWS: *Imaging in High-Aperture Optical-Systems*. *Journal of the Optical Society of America A-Optics Image Science and Vision*, 4(8):1354–1360, 1987.
- [28] ZIPFEL, WARREN R., REBECCA M. WILLIAMS and W. W. WEBB: *Nonlinear magic: multiphoton microscopy in the biosciences*. *Nature Biotech.*, 21:1369–1377, 2003.
- [29] GU, X. S. G. MIN: *Effect of the detector size and the fluorescence wavelength on the resolution of three- and two-photon confocal microscopy*. *Bioimaging*, 4(3):129–137, 1996.
- [30] GU, M. and C. J. R. SHEPPARD: *Comparison of 3-Dimensional Imaging Properties Between 2-Photon and Single-Photon Fluorescence Microscopy*. *Journal of Microscopy-Oxford*, 177:128–137, 1995.
- [31] GU, M. and C. J. R. SHEPPARD: *Effects of A Finite-Sized Pinhole on 3D Image-Formation in Confocal 2-Photon Fluorescence Microscopy*. *Journal of Modern Optics*, 40(10):2009–2024, 1993.

-
- [32] GAUDERON, R., P. B. LUKINS and C. J. SHEPPARD: *Effect of a confocal pinhole in two-photon microscopy*. *Microsc.Res.Tech.*, 47(3):210–214, 1-11-1999.
- [33] GAUDERON, R. and C. J. R. SHEPPARD: *Effect of a finite-size pinhole on noise performance in single-, two-, and three-photon confocal fluorescence microscopy*. *APPLIED OPTICS*, 38(16):3562–3565, 1-6-1999.
- [34] STELZER, E. H. K.: *Contrast, resolution, pixelation, dynamic range and signal-to-noise ration: fundamental limits to resolution in fluorescence light microscopy*. *Journal of Microscopy*, 189(1):15–24, 1998.
- [35] HECHT, E.: *Optik*. Oldenbourg Wissenschaftsverlag GmbH, München, 3rd Edition, 2001.
- [36] DENK, W., J. H. STRICKLER and W. W. WEBB: *Two-photon laser scanning fluorescence microscopy*. *Science*, 248:73–76, 1990.
- [37] DIASPRO, A., M. COROSU, P. RAMOINO and M. ROBELLO: *Adapting a compact confocal microscope system to a two-photon excitation fluorescence imaging architecture*. *Microsc.Res.Tech.*, 47(3):196–205, 1-11-1999.
- [38] MINSKY, M.: *Microscopy apparatus*, USA Patent No. 3,013,467; 1961.
- [39] PAWLEY, J. B. (Editor): *Handbook of Biological Confocal Microscopy*. Springer, New York, 3rd Edition, 2006.
- [40] CARLSSON, K., P. E. DANIELSSON, R. LENZ, A. LILJEBORG, L. MAJLOF and N. ASLUND: *3-Dimensional Microscopy Using A Confocal Laser Scanning Microscope*. *Optics Letters*, 10(2):53–55, 1985.
- [41] BRAKENHOFF, G. J., H. T. M. VANDERVOORT, E. A. VANSRONSEN, W. A. M. LINNEMANS and N. NANNINGA: *3-Dimensional Chromatin Distribution in Neuro-Blastoma Nuclei Shown by Confocal Scanning Laser Microscopy*. *Nature*, 317(6039):748–749, 1985.
- [42] LECHLEITER, J. D., D. T. LIN and I. SIENEART: *Multi-photon laser scanning microscopy using an acoustic optical deflector*. *Biophys.J.*, 83(4):2292–2299, 2002.
- [43] IYER, V., B. E. LOSAVIO and P. SAGGAU: *Compensation of spatial and temporal dispersion for acousto-optic multiphoton laser-scanning microscopy*. *J.Biomed.Opt.*, 8(3):460–471, 2003.

- [44] COX, G. and C. J. SHEPPARD: *Practical limits of resolution in confocal and non-linear microscopy*. Microsc.Res.Tech., 63(1):18–22, 1-1-2004.
- [45] CALMETTES, P. P. and M. W. BERNS: *Laser-induced multiphoton processes in living cells*. Proc.Natl.Acad.Sci.U.S.A, 80(23):7197–7199, 1983.
- [46] STELZER, E. H. K., S. HELL, S. LINDEK, R. STRICKER, R. PICK, C. STORZ, G. RITTER and N. SALMON: *Nonlinear Absorption Extends Confocal Fluorescence Microscopy Into the Ultra-Violet Regime and Confines the Illumination Volume*. Optics Communications, 104(4-6):223–228, 1-1-1994.
- [47] XU, C., W. ZIPFEL, J. B. SHEAR, R. M. WILLIAMS and W. W. WEBB: *Multiphoton fluorescence excitation: new spectral windows for biological nonlinear microscopy*. Proc.Natl.Acad.Sci.U.S.A, 93(20):10763–10768, 1-10-1996.
- [48] DACOSTA, R. S., H. ANDERSSON and B. C. WILSON: *Molecular fluorescence excitation-emission matrices relevant to tissue spectroscopy*. Photochem.Photobiol., 78(4):384–392, 2003.
- [49] CAHALAN, M. D., I PARKER, S. H. WEI and M. J. MILLER: *TWO-PHOTON TISSUE IMAGING: SEEING THE IMMUNE SYSTEM IN A FRESH LIGHT*. Nature, 2:872–880, 1-11-2002.
- [50] ROTHSTEIN, E. C., M. NAUMAN, S. CHESNICK and R. S. BALABAN: *Multiphoton excitation microscopy in intact animals*. J.Microsc., 222(Pt 1):58–64, 2006.
- [51] RUBART, M.: *Two-photon microscopy of cells and tissue*. Circ.Res., 95(12):1154–1166, 10-12-2004.
- [52] TAUER, U.: *Advantages and risks of multiphoton microscopy in physiology*. Exp.Physiol, 87(6):709–714, 2002.
- [53] SVOBODA, K. and R. YASUDA: *Principles of two-photon excitation microscopy and its applications to neuroscience*. Neuron, 50(6):823–839, 15-6-2006.
- [54] CHEONG, W. F., S. A. PRAHL and A. J. WELCH: *A review of the optical properties of biological tissues*. IEEE J.Quantum Electron., 26(12):2166–2185, 1990.
- [55] KÖNIG, K.: *Multiphoton microscopy in life sciences*. Journal of Microscopy, 200(2):83–104, 2000.

-
- [56] HELMCHEN, F. and W. DENK: *Deep tissue two-photon microscopy*. Nat.Methods, 2(12):932–940, 2005.
- [57] HOPT, A. and E. NEHER: *Highly nonlinear photodamage in two-photon fluorescence microscopy*. Biophys.J., 80(4):2029–2036, 2001.
- [58] DENK, W., STRICKLER J. H. and W. W. WEBB: *Two-photon laser scanning fluorescence microscopy*, USA Patent No. 5034613; 1991.
- [59] STOLLER, P., P. M. CELLIERS, K. M. REISER and A. M. RUBENCHIK: *Quantitative second-harmonic generation microscopy in collagen*. Appl.Opt., 42(25):5209–5219, 1-9-2003.
- [60] CENTONZE, V. E. and J. G. WHITE: *Multiphoton excitation provides optical sections from deeper within scattering specimens than confocal imaging*. Biophys.J., 75(4):2015–2024, 1998.
- [61] SO, P. T. C., H. KIM and I. E. KOICHEVAR: *Two-photon deep tissue ex vivo imaging of mouse dermal and subcutaneous structures*. Optics Express, 3(9):339–350, 26-10-1998.
- [62] BEAUREPAIRE, E., M. OHEIM and J. MERTZ: *Ultra-deep two-photon fluorescence excitation in turbid media*. Optics Communications, 188(1-4):25–29, 1-2-2001.
- [63] CHU, S. W., T. M. LIU and C. K. SUN: *Real-time second-harmonic-generation microscopy based on a 2-GHz repetition rate Ti : sapphire laser*. Optics Express, 11(8):933–938, 21-4-2003.
- [64] KURTZ, R., M. FRICKE, J. KALB, P. TINNEFELD and M. SAUER: *Application of multiline two-photon microscopy to functional in vivo imaging*. Journal of Neuroscience Methods, 151(2):276–286, 15-3-2006.
- [65] KONIG, K. and I. RIEMANN: *High-resolution multiphoton tomography of human skin with subcellular spatial resolution and picosecond time resolution*. J.Biomed.Opt., 8(3):432–439, 2003.
- [66] MASTERS, B. R., P. T. SO and E. GRATTON: *Multiphoton excitation fluorescence microscopy and spectroscopy of in vivo human skin*. Biophys.J., 72(6):2405–2412, 1997.

- [67] MASTERS, B. R. and P. T. C. SO: *Confocal microscopy and multi-photon excitation microscopy of human skin in vivo*. Optics Express, 8(1):2–10, 1-1-2001.
- [68] THEER, P., M. T. HASAN and W. DENK: *Two-photon imaging to a depth of 1000 μ m in living brains by use of a Ti : Al₂O₃ regenerative amplifier*. Optics Letters, 28(12):1022–1024, 15-6-2003.
- [69] DONG, C. Y., K. KOENIG and P. SO: *Characterizing point spread functions of two-photon fluorescence microscopy in turbid medium*. J Biomed.Opt., 8(3):450–459, 2003.
- [70] SZMACINSKI, H., I. GRYCZYNSKI and J. R. LAKOWICZ: *Spatially localized ballistic two-photon excitation in scattering media*. Biospectroscopy., 4(5):303–310, 1998.
- [71] GAN, X. S. and M. GU: *Fluorescence microscopic imaging through tissue-like turbid media*. Journal of Applied Physics, 87(7):3214–3221, 1-4-2000.
- [72] BEAUREPAIRE, E. and J. MERTZ: *Epifluorescence collection in two-photon microscopy*. Appl.Opt., 41(25):5376–5382, 1-9-2002.
- [73] KIM, K. H., C. BUEHLER and P. T. C. SO: *High-speed, two-photon scanning microscope*. APPLIED OPTICS, 38(28):6004–6009, 1-10-1999.
- [74] ROORDA, R. D., T. M. HOHL, R. TOLEDO-CROW and G. MIESENBOCK: *Video-rate nonlinear microscopy of neuronal membrane dynamics with genetically encoded probes*. J.Neurophysiol., 92(1):609–621, 2004.
- [75] FAN, G. Y., H. FUJISAKI, A. MIYAWAKI, R. K. TSAY, R. Y. TSIEN and M. H. ELLISMAN: *Video-rate scanning two-photon excitation fluorescence microscopy and ratio imaging with cameleons*. Biophys.J., 76(5):2412–2420, 1999.
- [76] ALBOTA, A. A., C. XU and W. W. WEBB: *Two-photon fluorescence excitation cross sections of biomolecular probes from 690 to 960nm*. APPLIED OPTICS, 37(31):7352–7356, 1-11-1998.
- [77] XU, R. M. W. CHRIS: *Multiphoton excitation cross-sections of molecular fluorophores*. Bioimaging, 4(3):198–207, 1996.
- [78] CHENG, P., B. LIN, F. KAO, M. GU, M. XU, X. GAN, M. HUANG and Y. WANG: *Multi-photon fluorescence microscopy—the response of plant cells to high intensity illumination*. Micron., 32(7):661–669, 2001.

-
- [79] BUIST, A. H., M MÜLLER, J. SQUIER and G. J. BRAKENHOFF: *Real time two-photon absorption microscopy using multi point excitation*. Journal of Microscopy, 192(Pt 2):217–226, 11-1-1998.
- [80] BEWERSDORF, J., R. PICK and S. HELL: *Multifocal Multiphoton Microscopy*. Optics Letters, 23(9):655–657, 1998.
- [81] HELL, S. W. and V. ANDRESEN: *Space-multiplexed multifocal nonlinear microscopy*. J.Microsc., 202(Pt 3):457–463, 2001.
- [82] EGNER, A., S. JAKOBS and S. W. HELL: *Fast 100-nm resolution three-dimensional microscope reveals structural plasticity of mitochondria in live yeast*. Proc.Natl.Acad.Sci.U.S.A., 99(6):3370–3375, 2002.
- [83] FUJITA, K., O. NAKAMURA, T. KANEKO, M. OYAMADA, T. TAKAMATSU and S. KAWATA: *Confocal multipoint multiphoton excitation microscope with microlens and pinhole arrays*. Optics Communications, 174(1-4):7–12, 2000.
- [84] STRAUB, M., P. LODEMANN, P. HOLROYD, R. JAHN and S. W. HELL: *Live cell imaging by multifocal multiphoton microscopy*. Eur.J.Cell Biol., 79(10):726–734, 2000.
- [85] EGNER, A., V. ANDRESEN and S. W. HELL: *Comparison of the axial resolution of practical Nipkow-disk confocal fluorescence microscopy with that of multifocal multiphoton microscopy: theory and experiment*. J Microsc., 206(Pt 1):24–32, 2002.
- [86] NIELSEN, T., M. FRICKE, D. HELLWEG and P. ANDRESEN: *High efficiency beam splitter for multifocal multiphoton microscopy*. Journal of Microscopy, 201(3):368–376, 2001.
- [87] FRICKE, M.: *Parallel-Processing in der Zwei-Photonen-Laser Raster-Mikroskopie: Anwendung in der Praxis und 3D-Visualisierung biologischer Zellen*, Thesis, 2000, Bielefeld University.
- [88] NIELSEN, T.: *Zeitaufgelöste Laserspektroskopie*, Thesis, 1999, Bielefeld University.
- [89] FITTINGHOFF, D. N., P. W. WISEMAN and J. A. SQUIER: *Widefield multiphoton and temporally decorrelated multifocal multiphoton microscopy*. Optics Express, 7(8):273–279, 9-10-2000.

- [90] FRICKE, M. and T. NIELSEN: *Two-dimensional imaging without scanning by multifocal multiphoton microscopy*. Appl.Opt., 44(15):2984–2988, 20-5-2005.
- [91] KALB, J., T. NIELSEN, M. FRICKE, M. EGELHAAF and R. KURTZ: *In vivo two-photon laser-scanning microscopy of Ca²⁺ dynamics in visual motion-sensitive neurons*. Biochem.Biophys.Res.Comm., 316(2):341–347, 2-4-2004.
- [92] KIRCHHOF, K.: *Zellbiologische Charakterisierung und mikroskopische Analyse von Knorpelbiopsien und in vitro-Knorpelkonstrukten als Grundlage für online-Untersuchungen mittels Laser-Raster-Mikroskopie (CLSM, TPLSM)*, Thesis, 2005, Martin-Luther-Universität Halle-Wittenberg.
- [93] MARTINEK, V.: *Anatomy and pathophysiology of articular cartilage*. Deutsche Zeitschrift für Sportmedizin, 54(6):166–170, 2003.
- [94] JAMES, C.-B. and T. L. UHL: *A Review of Articular Cartilage Pathology and the Use of Glucosamine Sulfate*. Journal of Athletic Training, 36(4):413–419, 2005.
- [95] GROHMANN, S.: *Biochemische und Molekularbiologische Analyse der Matrix-synthese von Chondrozyten auf verschiedenen Trägermaterialien*, Thesis, 2005, Friedrich-Schiller-Universität Jena.
- [96] LAASANEN, M. S., J TÖYRÄS, R. K. KORHONEN, J. RIEPPO, S. SAARAKKALA, M. T. NIEMINEN, J. HIRVONEN and J. S. JURVELIN: *Biomechanical properties of knee articular cartilage*. Biorheology, 40:133–140, 2003.
- [97] HUNZIKER, E. B., T. M. QUINN and H.-J. HÄUSELMANN: *Quantitative structural organization of normal adult human articular cartilage*. Osteoarthritis and Cartilage, 10:564–572, 2002.
- [98] POPP, J., STREHLE M. (Editor): *Biophotonics - Visions for Better Health Care*. WILEY-VCH Verlag GmbH & Co. KGaA, Weinheim, 1st Edition, 2006.
- [99] REDMAN, S. N., OLDFIELD S.F. and C. W. ARCHER: *CURRENT STRATEGIES FOR ARTICULAR CARTILAGE REPAIR*. European Cells and Materials, 9:23–32, 2005.
- [100] HUNZIKER, E. B.: *Articular cartilage repair: basic science and clinical progress. A review of the current status and prospects*. Osteoarthritis and Cartilage, 10(6):432–463, 2001.

-
- [101] CLAR, C., E. CUMMINS, L. MCINTYRE, S. THOMAS, J. LAMB, L. BAIN, P. JOBANPUTRA and N. WAUGH: *Clinical and cost-effectiveness of autologous chondrocyte implantation for cartilage defects in knee joints: systematic review and economic evaluation*. Health Technol.Assess., 9(47):iii–x, 1, 2005.
- [102] WILLERS, C., J. CHEN, D. WOOD, J. XU and M. H. ZHENG: *Autologous chondrocyte implantation with collagen bioscaffold for the treatment of osteochondral defects in rabbits*. Tissue Eng., 11(7-8):1065–1076, 2005.
- [103] BEHRENS, P., T. BITTER, B. KURZ and M. RUSSLIES: *Matrix-associated autologous chondrocyte transplantation/implantation (MACT/MACI)–5-year follow-up*. Knee., 13(3):194–202, 2006.
- [104] MARTIN, I., D. WENDT and M. HEBERER: *The role of bioreactors in tissue engineering*. TRENDS in Biotechnology, 22(2):80–86, 2004.
- [105] MEYVIS, T. K., S. C. DE SMEDT, P. VAN OOSTVELDT and J. DEMEESTER: *Fluorescence recovery after photobleaching: a versatile tool for mobility and interaction measurements in pharmaceutical research*. Pharm.Res., 16(8):1153–1162, 1999.
- [106] MARCHANT, J. S., G. E. STUTZMANN, M. A. LEISSRING, F. M. LAFERLA and I. PARKER: *Multiphoton-evoked color change of DsRed as an optical highlighter for cellular and subcellular labeling*. Nat.Biotechnol., 19(7):645–649, 2001.
- [107] CHUDAKOV, D. M., V. V. VERKHUSHA, D. B. STAROVEROV, E. A. SOUSLOVA, S. LUKYANOV and K. A. LUKYANOV: *Photoswitchable cyan fluorescent protein for protein tracking*. Nat.Biotechnol., 22(11):1435–1439, 2004.
- [108] POST, J. N., K. A. LIDKE, B. RIEGER and D. J. ARNDT-JOVIN: *One- and two-photon photoactivation of a paGFP-fusion protein in live Drosophila embryos*. FEBS Letters, 579:325–330, 2005.
- [109] PATTERSON, G. H. and J. LIPPINCOTT-SCHWARTZ: *Selective photolabeling of proteins using photoactivatable GFP*. Methods, 32:445–450, 2004.
- [110] PATTERSON, G. H. and J. LIPPINCOTT-SCHWARTZ: *A Photoactivatable GFP for Selective Photolabeling of Proteins and Cells*. Science, 291:1873–1877, 2002.

- [111] SCHNEIDER, M., S. BAROZZI, I. TESTA, M. FARETTA and ALBERTO DIASPRO: *Two-Photon Activation and Excitation Properties of PA-GFP in the 720-920-nm Region*. Biophys.J, 89:1346–1352, 2005.
- [112] CHEN, Y., P. J. MACDONALD, J. P. SKINNER, G. H. PATTERSON and J. D. MULLER: *Probing nucleocytoplasmic transport by two-photon activation of PA-GFP*. Microsc.Res.Tech., 69(3):220–226, 2006.
- [113] MARTINI, J., K SCHMIED, R. PALMISANO, K. TÖNSING, D. ANSELMETTI and T. MERKLE: *Intracellular dynamics of a transcription factor containing a nuclear export signal by two-photon laser scanning microscopy and photo-activatable GFP*. submitted, 2006.
- [114] ALBERTS, B., JOHNSON-A. LEWIS J. RAFF M. ROBERTS K. and P. WALTER (Editor): *Molecular Biology of the Cell*. Garland Science, Taylor & Francis Group, New York, 4th Edition, 2002.
- [115] MERKLE, T.: *Nucleo-cytoplasmic partitioning of proteins in plants: implications for the regulation of environmental and developmental signalling*. Curr.Genet., 44(5):231–260, 2003.
- [116] SCHMIED, K: *Funktionale Charakterisierung einer kleinen Familie von Arabidopsis MYB1R-Transkriptionsfaktoren : LHY/CCA1-like (LCL) Proteine als potentielle Koregulatoren des zentralen Oszillators*, Thesis, 2005, Bielefeld University.
- [117] SCHMIED, K and T. MERKLE: *The Arabidopsis LHY/CCA1-like (LCL) protein family: MYB transcription factors containing a nuclear export signal are co-regulators of the circadian clock*. submitted, 2006.
- [118] GRATTON, E., S. BREUSEGEM, J. SUTIN, Q. RUAN and N. BARRY: *Fluorescence lifetime imaging for the two-photon microscope: time-domain and frequency-domain methods*. J.Biomed.Opt., 8(3):381–390, 2003.
- [119] RASBAND, W. S.: *ImageJ*, Computer Program, 1997-2005, U. S. National Institutes of Health, Bethesda, Maryland, USA, <http://rsb.info.nih.gov/ij/>.
- [120] YEH, A. T., M. J. HAMMER-WILSON, D. C. VAN SICKLE, H. P. BENTON, A. ZOUMI, B. J. TROMBERG and G. M. PEAVY: *Nonlinear optical microscopy of articular cartilage*. Osteoarthritis Cartilage, 13(4):345–352, 2005.

- [121] MARTINI, J., TÖNSING K. DICKOB M. and D. ANSELMETTI: *2-Photon Laser Scanning Microscopy on Native Human Cartilage*. Proceedings of SPIE, 5860:16–21, 2005.
- [122] MARTINI, J., TÖNSING K. DICKOB M. SCHADE R. LIEFEITH K. and D. ANSELMETTI: *2-Photon Laser Scanning Microscopy on Native Human Cartilage and Collagen-Membranes for Tissue Engineering*. Proceedings of SPIE, 6089:274–282, 2006.
- [123] HUANG, S., A. A. HEIKAL and W. W. WEBB: *Two-photon fluorescence spectroscopy and microscopy of NAD(P)H and flavoprotein*. Biophys.J., 82(5):2811–2825, 2002.
- [124] ZOUMI, A., A. YEH and B. J. TROMBERG: *Imaging cells and extracellular matrix in vivo by using second-harmonic generation and two-photon excited fluorescence*. Proc.Natl.Acad.Sci.U.S.A, 99(17):11014–11019, 20-8-2002.
- [125] MARCU, L., COHEN D. MAAREK J.-M. I. and W. GRUNDFEST: *Characterization of Type I, II, III, IV and V collagens by time-resolved laser-induced fluorescence spectroscopy*. Proceedings of SPIE, 3917:93–101, 2000.

List of Publications

1. J. MARTINI, K. TÖNSING, M. DICKOB. and D. ANSELMETTI: *2-Photon Laser Scanning Microscopy on Native Human Cartilage*. Proceedings of SPIE, 5860: 16–21, 2005.
2. J. MARTINI, K. TÖNSING, M. DICKOB., R. SCHADE, K. LIEFEITH and D. ANSELMETTI: *2-Photon Laser Scanning Microscopy on Native Human Cartilage and Collagen-Membranes for Tissue Engineering*. Proceedings of SPIE, 6089: 274–282, 2006.
3. R. ECKEL, V. WALHORN, C. PELARGUS, J. MARTINI, T. NANN, D. ANSELMETTI and R. ROS: *Combined TIRF-AFM Setup: Controlled Quenching of Individual Quantum Dots*. Proceedings of SPIE, 6092: 49–56, 2006.
4. V. ANDRESEN, H. SPIECKER, J. MARTINI, K. TÖNSING, D. ANSELMETTI, R. SCHADE, S. GROHMANN, G. HILDEBRAND AND K. LIEFEITH: *Regenerative Surgery (Metabolism and Morphology of Biological Tissue -MeMo)*. in: J. POPP, M. STREHLE (Editor): *Biophotonics - Visions for Better Health Care*. WILEY-VCH Verlag GmbH & Co. KGaA, Weinheim, 1st Edition, 2006.
5. J. MARTINI, K. SCHMIED, R. PALMISANO, K. TÖNSING, D. ANSELMETTI and T. MERKLE: *Intracellular dynamics of a transcription factor containing a nuclear export signal by two-photon laser scanning microscopy and photo-activatable GFP*. submitted, 2006.
6. R. ECKEL, V. WALHORN, C. PELARGUS, J. MARTINI, J. ENDERLEIN, T. NANN, D. ANSELMETTI and R. ROS: *Fluorescence Emission Control of Single CdSe Nanocrystals Using Gold-Modified AFM Tips*. Analytical and Bioanalytical Chemistry, in press, 2006.
7. D. ANSELMETTI, N. HANSMEIER, J. KALINOWSKI, J. MARTINI, T. MERKLE, R. PALMISANO., R. ROS, K. SCHMIED, A. SISCHKA and K. Tönsing: *Analysis of Subcellular Surface Structure, Function and Dynamics*. Analytical and Bioanalytical Chemistry, in press, 2006.
8. J. MARTINI, K. TÖNSING and D. ANSELMETTI: *Visualisierung zellulärer Makrostrukturen mittels multifokaler 2-Photonen-Laser-Scanning-Mikroskopie für das Tissue Engineering*. BIOSpektrum 5, 489-492, 2006.

9. J. MARTINI, W. HELLMICH, D. GREIF, A. BECKER, T. MERKLE, R. ROS, A. ROS, K. TÖNSING AND D. ANSELMETTI: *Systems Nanobiology: From Quantitative Single Molecule Biophysics to Microfluidic-Based Single Cell Analysis*. in: M. FAUPEL, E. BERTRAND (Editor): *Subcellular Fractionation and Proteomics*. Springer, Heidelberg, submitted, 2006.
10. J. MARTINI and D. ANSELMETTI: *Scattering Suppression and Confocal Detection in Multifocal Multiphoton Microscopy*. submitted, 2006.
11. R. SCHADE, J. MARTINI, K. TÖNSING, D. ANSELMETTI and K. LIEFEITH: *Laseroptische Methoden basierend auf der Zweiphotonen-Mikroskopie zur Detektion von Chondrozyten auf artifiziellen Kollagen-I/III-Trägern*. Dresdner Beiträge zur Medizintechnik, TUDpress Verlag der Wissenschaften GmbH Dresden, in press, 2006.

Contributions to conferences

1. J. MARTINI, V. WALHORN, T. KRAMER, G. KIM, J. STEEN, J. BRUGGER, R. ROS and D. ANSELMETTI: *Small Cantilever AFM for single molecule Force Spectroscopy*. (poster), DPG Frühjahrstagung 2004.
2. J. STEEN, T. KRAMER, J. BRUGGER, V. WALHORN, J. MARTINI, R. ROS and D. ANSELMETTI: *Small SiN AFM Cantilevers for High Frequency Application*. (poster), Trends in Nanotechnology 2004.
3. J. MARTINI, K. TÖNSING and D. ANSELMETTI: *Multi Focal 2-Photon Laser Scanning Microscopy of Cells and Biological Tissue*. (talk), DPG Frühjahrstagung 2005.
4. J. MARTINI, K. TÖNSING, D. ANSELMETTI, K. KIRCHHOF, R. SCHADE, K. LIEFEITH, V. KUNERT, K. HINTERKEUSER, V. ANDRESEN and H. SPIECKER: *2-Photon Laser Scanning Microscopy on Native Human Chondrocytes for Tissue Engineering*. (talk), Focus on Microscopy 2005.
5. J. MARTINI, K. TÖNSING, M. DICKOB., R. SCHADE, K. LIEFEITH and D. ANSELMETTI: *2-Photon Laser Scanning Microscopy on Native Human Cartilage and Collagen-Membranes for Tissue Engineering*. (poster), The 41st Winterseminar, Klosters, 2006.

6. S.GROHMANN, R. SCHADE, J. MARTINI, D. ANSELMETTI and K. LIEFEITH:
Visualization of chondrocytes on collagen scaffolds by two photon laser scanning microscopy (TPLSM). (talk), ECM VII: Cartilage & Joint Repair, Davos, 2006.

Acknowledgment

Nature is really really complex. Therefore, scientific work requires the contributions of many people. This is especially true for an interdisciplinary work like this, which was supported by the expertise, preparation and help of various people.

First of all, I would like to thank Prof. Dr. Dario Anselmetti who entrusted the MeMo-project at Bielefeld University to me. He supported me by his enthusiasm and scientific guidance but also gave me the freedom to follow my own scientific curiosity.

I am thankful to Prof. Dr. Markus Sauer, who agreed to evaluate this work within such a short timeframe.

Thanks to Katja Tönsing, who also took on the burden of the organizational work in the MeMo-project, I learned a lot about staining and handling biological material.

I thank Robert Ros, who has often been a great support, more than he might know, by giving me general scientific advice.

The competence of the people working in the shops at the faculty of physics, particularly Kay Schnurrbusch's realization of the PMT electronics, enabled many of the experiment's advances. Thank You!

I thank Ronald Schade and his colleagues from IBA, who did not only provide the populated collagen membranes, but also taught me most of what I know about tissue engineering. Thanks to Michael Dickob, I learned a lot about the cartilage that he provided and more about knee surgeries than I ever wanted to know.

I owe great thanks to Volker Andresen from LaVision BioTec. He not only taught me how to use the TriM-scope, but he was always there to discuss details and ideas about MMM and gave me countless tips and advice. The software department at LaVision BioTec helped me on many times with data processing and enabled the new parallel detection modes, thanks to Martin Ahlering and Kai Schröder.

The Pa-GFP measurements were initiated and prepared by Thomas Merkle, Ralf Palmisano and Katja Schmied. I am thankful, for their biological expertise and sample preparation.

This work has only been possible because I had access to excellent equipment, thanks to financial support by the "Biophotonik" research initiative of the Bundesministerium für Bildung und Forschung (Grant MeMo, FKZ: 13N8432).

My colleagues at the Department of Experimental Biophysics and Applied Nanosciences at Bielefeld University provided a great working environment over the last years. For example, I would like to thank Christoph Pelargus for repairing the computer numerous times and helping me on with the optics; Rainer Eckel for Matlab programming,

theoretical and chemical support; Volker Walhorn for proof reading, electronic scrap excursions and usually knowing where the oscilloscope was; Herman Kleine for introducing me to Steinhagener Feng Shui; Dominik Greif, who did not always know the answers to my biological questions, but knew who to ask or where to look it up; Tobias Kahre for countless business meetings, electronics support and not talking too loudly to his computer; and everyone else for offering cake, favors, a great work atmosphere and much more. Thank you!

Spending so much time at work, one needs great family support to manage "real" life. Ich danke daher meinen Eltern, die mich über die Jahre, nicht nur während des Studiums, so vielfältig unterstützt haben.

Finally, I thank my beloved Liz de Renzy for her absolute support.